Stars and planets at high spatial and spectral resolution

Albrecht, S.

Stars and planets

at high

spatial and spectral resolution

Stars and planets

at high

spatial and spectral resolution

Proefschrift

ter verkrijging van
de graad van Doctor aan de Universiteit Leiden,
op gezag van de Rector Magnificus prof. mr. P.F. van der Heijden,
volgens besluit van het College voor Promoties
te verdedigen op woensdag 17 december 2008
klokke 15.00 uur

door

Simon Albrecht

geboren te Osnabrück

Promotiecommissie

Promotor:	Prof. dr. A. Quirrenbach	
Co-promotor:	Dr. I. A. G. Snellen	
Referent:	Dr. M. Fridlund	(European Space Agency, ESTEC, Noordwijk)
Overige leden:	Dr. M. Hogerheijde	
	Prof. dr. K. H. Kuijken	
	Dr. J. Lub	
	Prof.dr. E. F. van Dishoeck	

Für meine Mutter

Sunset as seen by NASA's Mars Rover Spirit on May 19th, 2005. The floor of the Gusev crater is visible in the distance, and the Sun is setting behind its wall some 80 km away. One can see the scatter of sunlight by dust particles in the Martian atmosphere (NASA JPL). Thanks to the rover team for building these wonderful spacecrafts and making the photos publically available. Cover made by Sebastian Heimann.

Contents

Chapter 1

Introduction

Light has told us nearly everything about the cosmos we know today. With our ability to measure its characteristics more and more accurately, our understanding of the universe has increased dramatically.

Since the invention of the telescope 400 years ago, enormous progress has been made in the angular and spectral resolution of telescopes, and in increasing the range of wavelengths over which electromagnetic waves can be measured. This development has made a profound impact on our understanding of the formation and evolution of stars and planetary systems. Space-based observatories, such as IRAS, ISO, and Spitzer, have opened up the infrared spectral window, which have allowed the investigation of interstellar clouds as birth-places of stars, and the study of circumstellar disks from which it is thought planets may be formed. The advent of optical/infrared interferometry allows us now to probe the inner parts of these proto-planetary disks, giving insights into their structure, dynamics, and evolution. In parallel to these developments, the recent improvements in the accuracy and stability of optical spectrographs have lead to the dawn of population studies of extrasolar planet systems. It is thought that this progress in instrumental techniques continues to flourish, leading possibly to the direct imaging of Earth-like planets, and planets not at all like our own, in the not too distant future.

The work presented in this thesis involves the development of new instrumental techniques and analysing tools, combining high spectral resolution with high spatial information, with the aim to increase our understanding of the formation and evolution of stars and planets. First, in Chapter 2 a novel instrumental concept is presented that aims to achieve high spatial and spectral resolution by combining existing Echelle spectrographs with existing optical interferometers. Subsequently, several studies combining high spatial and spectral resolution are presented. In the third chapter of this thesis we investigate the immediate environment of the massive young stellar object MWC 349A, using the MIDI instrument on the VLT interferometer. In Chapter 4, new methods are presented to analyse the Rossiter-McLaughlin effect during stellar eclipses. By using this effect it is possible to obtain high resolution spectra from different parts of stellar surfaces, and de facto to obtain spatial information on stellar surface scales, something difficult to achieve by other means. Using these new tools we show that the spin axes in both stars of the V1143 Cyg system are aligned with the orbital spin axis. For the stars in the DI Herculis system, for which we present our results in Chapter 5, the situation turned out to be very different. In this system the axes of both stars are strongly tilted with respect to the orbital angular momentum. This solves a 20 year old riddle about the DI Herculis system, involving its apparently slow apsidal motion, but it presents new challenges for binary formation theories. In the final chapter of this thesis I present sodium measurements for the atmosphere of the extrasolar planet HD 209458b using ground-based transmission spectroscopy.

1.1 The formation of stars and planets in a nutshell

In recent years the research field of single, low-mass star formation has seen an enormous development, both due to new ground-based and space-based instruments and observational techniques, and due to the development of astrophysical theories that support these observations. Star formation occurs in cold dense clouds of gas and dust. While the cloud is supported by magnetic fields and turbulence, the densest regions can collapse under the influence of gravity. At the centre of these dense cores, a star begins to form. During this process it is thought that a circumstellar disk is formed by in-falling material due to its non-zero angular momentum. Accretion from the disk onto the star, is believed to drive bi-polar outflows that help to transport the excess angular momentum away. When the reservoir of cloud material that feeds the disk is exhausted, the accretion rate from the disk onto the star drops. While the star contracts, its temperature increases and the developing stellar winds clear away the remaining material from the cloud. In the disk, planetesimals and finally planets are thought to be able to form. The star, which thus far has generated most of its energy from contraction, is now mainly powered by hydrogen fusion and does not contract anymore. It has reached the main sequence. The surrounding disk is dissipated and the leftover material comprises a debris-disk, possibly with planets.

In the field of star formation the theory of single low-mass star formation, as described above, is most advanced. However, in the fields of the formation of high-mass stars, and the formation of multiple systems, many open questions remain.

1.1.1 Formation of high-mass stars

The processes which lead to the formation of massive stars are not well understood yet (see Zinnecker & Yorke 2007, for a review). The reasons for this are the shorter time scale over which the formation of massive stars occurs, the smaller numbers of massive stars, and the greater distances between us and the nearest regions where massive stars are forming. As an additional consequence of the short times scales over which the formation of massive stars occurs a much greater portion of their formation history is hidden from our view compared to the case for low-mass star formation. Finally, massive stars often form in the densest clusters, making the interpretation of the observations much more difficult.

Nevertheless, the following sequence of events towards the formation of massive stars can be drawn (Zinnecker & Yorke 2007). In a giant molecular cloud, cold dense cores or filaments, possibly formed by supersonic turbulence, generate gravitationally bound pockets of compressed gas. These 10-15K cold cores subsequently collapse under the influence of gravity into optically thick, pressure-supported stellar embryos. This phase is thought to be followed by accretion onto the proto-stellar objects while they evolve towards the main sequence. While for low-mass stars it is believed that the accretion stops before the onset of hydrogen burning, for massive stars it is believed that hydrogen burning already starts while accretion is still ongoing. The young high-mass stars emit a high degree of UV radiation and generate HII regions around them. Furthermore, these high-mass stars generate strong winds during accretion, which will eventually clear their surroundings and disrupt the birth cloud of the star.

Despite having this general picture of massive star formation, many questions are still unanswered. For example, do massive stars always form in dense clusters or can they also form in isolation? What role does binarity play in the formation of massive stars? Can massive stars form through mergers? To what extent have circumstellar disks time to form in the surrounding of these high-mass stars? How long will they survive in the intense radiation field of the massive star, and can planets form in these disks? How does the formation of a massive star shape its environment and influence neighbouring proto-stars? In particular, in what way do they influence the formation of low-mass stars and their planets?

In Chapter 3 we contribute to the efforts of answering these questions by studying the structure of the disk around one isolated young stellar object, which has already dispersed its parent cloud, using the VLT interferometer.

1.1.2 Stellar binaries

Many problems in the field of the star formation, for either low- or high-mass stars, are connected to angular momentum. How do stars slow down their rotation after forming with a rapid spin rate? Do stars in binary systems acquire a common angular momentum and orientation from their parent molecular cloud? How do tidal interactions between stars, and between planets and stars, result in a redistribution of angular momentum among the rotating bodies and their orbits? Most stars (and by extension their planets) are born in double or multiple star systems (e.g. Ghez et al. 1993). Therefore, the problem of binary stars is central to a complete understanding of star formation. It is suspected that even the Sun was once a member of a multiple system, based partly on evidence directly related to observations discussed in this thesis: the observed 7° tilt between the planetary orbits and the solar spin axis (Heller 1993). According to theories of binary star formation, the overall angular momentum distribution is a key determinant (Goodwin et al. 2007), but there are other important aspects of the parent interstellar cloud, such as its geometry, its gravitational and thermal energy, and its magnetic fields. It is important to know the relative influence of these factors on the formation processes (e.g. Bonnell et al. 1992; Larson 2003; Machida et al. 2003). One way to determine the relative importance of angular momentum is by measuring the relative orientation of the stellar spin-axes: for what maximum orbital period are the stars observed to be well-aligned? Until quite recently there had been little hope of answering this question, although there is circumstantial evidence for misalignment in a few very long-period systems (hundreds of years) (e.g Jensen et al. 2004; Skemer et al. 2008). On the other hand, for extremely close binaries, in which the stars are nearly in contact, one can safely assume that tidal forces have co-aligned the stars even if they did not form in that way. Observations between these two extremes have heretofore been unavailable, but they are critical, as they will define the scale length over which the primordial angular momentum was influential.

How can the orientation of stellar rotation axes be measured when even the world's biggest telescopes cannot resolve stellar surfaces to the necessary degree? Optical interferometers have a high enough spatial resolution to (partly) resolve the stellar surfaces. If they would have a high enough spectral resolution to resolve stellar absorption lines, measurements of the colour-differential phase would probe the relative difference in position on-sky between the centroid of the blue-shifted light and the centroid of the rotationally red-shifted light. Measurements at different projected baselines would in this way reveal the orientation of the stellar spin axes

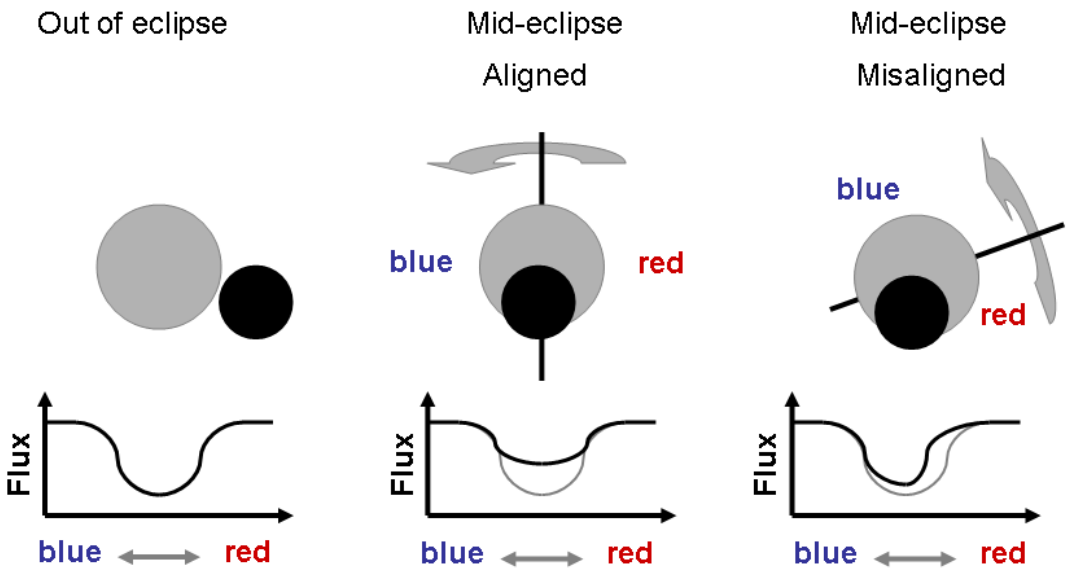

Figure 1.1 — Schematic picture of the Rossiter-McLaughlin effect. Due to stellar rotation, an observed absorption line is broadened (left). A partial eclipse by a foreground object deforms the absorption line differently if the stellar spin axis is aligned (middle panel) or misaligned (right panel).

(Petrov 1989; Chelli & Petrov 1995). More detailed modeling of the interferometric signal can also provide the inclination of the stellar rotation axis (Domiciano de Souza et al. 2004). This was partly our motivation to develop, in the framework of this thesis, the concept of an interferometric instrument which will be able to measure, next to other quantities of stars and circumstellar disks, the orientation of stellar rotation axes (Chapter 2).

For eclipsing binaries, however, one can obtain spatial information 'for free' since during the eclipse of one star by another different portions of the stellar disk are obscured at different times, providing an opportunity to resolve details on the surface of the eclipsed star. Particularly interesting in this respect is the Rossiter-McLaughlin (RM) effect (Rossiter 1924; McLaughlin 1924), a spectral distortion that is caused by the blockage of parts of the rotating stellar disk (see Figure 1.1). Due to the Doppler effect, light emitted from the side of the stellar disk that moves towards us is blueshifted and light emitted from the receding side is redshifted. When the redshifted (receding) part of the disk is blocked, the net starlight looks slightly blueshifted, and vice versa. If the spin axis of the eclipsed star is aligned with the orbital axis, first blueshifted light and later, to the same amount, redshifted light is blocked. For a misaligned axis this is not true, and redshifted and blueshifted light is blocked at different times and to different amounts. The RM effect has been known since 1924, but has not been exploited until recently because it is difficult to measure precisely and analyse quantitatively. For binary star systems this is partly because the absorption lines of the eclipsing foreground star blend the lines of the eclipsed background star. We will approach this challenge in Chapters 4 and 5 of this thesis.

1.1.3 Planets

The improvement of techniques originally developed for double star systems, in particular advances in the stability of Echelle spectrographs and analysis techniques, which made it possible to combine the signal of thousands of stellar absorption lines, have lead to the detection of the first extra solar planets around solar type stars (Mayor & Queloz 1995). Since the mid-1990s more than 300 planets have been detected. Via the measurement of Doppler shifts induced by the planetary companion, the orbital period of the planet, the eccentricity of its orbit and its minimum mass (the inclination of the orbit is not known) can be determined. More recently, also other techniques contributed to detections of planets such as micro-lensing, measurements of planetary transits, and recently also direct imaging of some massive planets around young stars.

The first planet for which a transit was measured was HD 209458b (Charbonneau et al. 2000). As for stellar eclipse measurements, transit measurements allow for the determination of the radius and mass, and therefore the density of the components. Now more than 40 transiting planets have been discovered and these measurements have shown, together with the Doppler measurements, that extrasolar planets are a very heterogeneous group with many surprising properties. For example it is believed that giant planets, such as Jupiter and Saturn, can only form at great distances from the parent stars, where ices are available in solid form to provide extra bulk to growing proto-planets. It was therefore a huge surprise to discover that $\sim$1% of Sun-like stars harbor a giant planet that orbits much closer than Mercury orbits the Sun. This finding has prompted major revisions in the theory of planet formation, mainly by allowing for 'migration' of planets to different orbits after they have formed (Lin et al. 1996). One class of migration theories invokes a tidal interaction between the planet and the disk of dust and gas from which it formed (e.g. Ida & Lin 2004). A second class of theories explains the migration by planet-planet gravitational scattering (e.g. Rasio & Ford 1996; Nagasawa et al. 2008) and a type of three-body interaction called the Kozai effect (Wu & Murray 2003).

The first theory, disk-planet migration, would leave the orbital spin axis aligned with the stellar spin axis, while the latter migration processes would produce misalignment. Hence, by measuring the degree of alignment between stellar and orbital axes one can distinguish between these theories. Researchers have begun to measure the relative orientation of the spin axes using the RM-effect (e.g. Winn et al. 2005). Recently, the first planetary system with a likely misalignment, XO-3, has been found (Hébrard et al. 2008). With the now rapidly growing sample of transiting planets, soon also planets with somewhat longer orbital periods, due to the space missions CoRoT and Kepler, the relative orientation of the stellar spin axis with respect to the orbital plane will be measured for a much larger sample, meaning that soon we might have a clearer picture about the formation history of these hot gas giants.

In addition, it has been found that some planets are inflated, i.e. their density is much lower than theory would predict (see Charbonneau et al. 2007, for a review). Is this a result of the intense stellar radiation these planets experience in their close orbits? Or might this be due to the tidal forces these planets experience in their possibly slightly eccentric orbits? While so far no clear route to solving the problem has appeared, measurements of the energy budget, by observing the eclipse of the planet by the star in the infrared (de Mooij & Snellen 2008), and observations of the brightness of the planet as a function of the planetary longitude (Knutson et al. 2007), might help to constrain possible theories. The measured orbital eccentricities for

these planets themselves constitute another challenge for formation and evolution theories. For short-period planets, it is expected that eccentricities are quickly damped by tidal forces. Non-zero eccentricities may be caused by the presence of yet undiscovered planets in wider orbits.

The same group that observed the first planetary transit were first to detect signatures from this planet's atmosphere with transmission spectroscopy using STIS on HST (Charbonneau et al. 2002). Taking advantage of the stability and accuracy of this observatory, they could observe the transit depth with great precision in many different spectral bands. As planetary atmospheres absorb wavelength dependent, they could, for the first time, identify the signature of sodium. In the last chapter of this thesis I further develop techniques to observe extrasolar planets during transits, to make it possible to observe their atmospheres also using ground-based telescopes.

1.2 This thesis

In **Chapter 2** a novel instrumental concept is presented. It is shown that by coupling existing high-resolution spectrographs to existing interferometers, one can observe in the domain of high spectral and spatial resolution, and avoid the construction of a new complex and expensive instrument. We first show that this combination of high spatial and spectral resolution in optical astronomy would allow new observational approaches to many open problems in stellar and circumstellar astrophysics. The different challenges, which arise from combining an interferometer with a high-resolution spectrograph, are investigated. The requirements for the different sub-systems are determined, with special attention given to the problems of fringe tracking and dispersion in the interferometer. A concept study for the combination of the Very Large Telescope Interferometer (VLTI) with UV-Visual Echelle Spectrograph (UVES) is carried out, and several other specific instrument pairings are discussed. We show that the proposed combination of an interferometer with a high-resolution spectrograph is indeed feasible with current technology, for a small fraction of the cost of building a whole new spectrograph.

In **Chapter 3** observations and analysis of the massive young stellar object MWC 349A are presented, using the unique capabilities of the VLTI in combination with the Mid-Infrared Interferometric Instrument (MIDI) in N-band. The data can be modeled assuming a circumstellar disk consisting partly of amorphous silicates, and with a strong temperature gradient, as function of disk height above the mid-plane, out to a few hundred AU. The measurement of hydrogen recombination line masers in the visibility amplitudes and differential phases delivered by MIDI enabled us to create a simple model consisting of two emission regions located a few tens of AU away from the centre of the object. This agrees with what is found by earlier studies, that the hydrogen recombination lines originate in the atmosphere of the inner parts of the circumstellar disk. The simultaneous observation of the continuum emission from the circumstellar disk and the observation of the hydrogen lines enables us to establish that there exists a small but significant offset in the location of the centroid of the continuum and the centre of the emission line region, something difficult to establish if the continuum and the masers are observed with different instruments at different times.

In **Chapter 4 and Chapter 5** we use high spectral resolution observations of stellar eclipses to obtain spatial resolution information on stellar surface scales. We developed new and robust modeling tools to analyse the spectral distortion of stellar absorption lines during the eclipses, caused by the Rossiter–McLaughlin (RM) effect, which disentangle the light from the eclipsing foreground star and the light of the eclipsed background star.

For the eclipsing binary system V1143Cyg, which was observed at the Lick Observatory using the Hamilton high-resolution Echelle spectrograph, it is shown in **Chapter 4** that the rotation axes of the two stars are aligned with respect to each other and with the orbital axis, to within a few degrees, with the angle of the primary rotation axis $\beta_p = 0.3 \pm 1.5^\circ$, and the angle of the secondary rotation axis $\beta_s = -1.2 \pm 1.6^\circ$.

In **Chapter 5** we present our results for the binary system DI Herculis, which we observed with the Sophie high-resolution Echelle spectrograph on the Observatoire de Haute Provence. Our results show that the spin axes of both stars are tilted with respect to the orbital axis. The angle between the projected stellar spin axes and the projected orbital spin axis is $\beta_p = 71 \pm 4^\circ$ for the primary and $\beta_s = 93 \pm 8^\circ$ for the secondary. This is, to our knowledge, the first clear demonstration of such a strong misalignment in a close binary system. It solves a 20-year-old mystery about this system: the observed orbital precession is too slow to be in agreement with the predictions of general relativity (Moffat 1984, Claret 1998). This prediction was based on the premise of co-aligned stars. When this assumption is relaxed the paradox disappears. These results are not only important for the DI Herculis system but also for the formation and evolution theories of binary stars in general, since it is unclear how this system has formed and evolved this way.

In the final chapter of this thesis (**Chapter 6**) we present our results on ground-based transmission spectroscopy of the planetary atmosphere of HD 209458b. It is shown that transmission spectroscopy can be done routinely from the ground, possibly also for planets around less bright stars than HD 209458. The obtained spectra are corrected for instrumental effects, which influence the transmission spectroscopy, such as a change of the blaze function of the spectrograph, and a non-linearity effect in the CCD. Furthermore, methods have been developed to remove the influence of telluric sodium absorption, and absorption due to water in earth's atmosphere for spectra obtained under less than ideal weather conditions. We detect sodium in the atmosphere of HD 209458b and our measurements are fully consistent with earlier results. We further extend these observations by measuring the ratio between the Na D_2 and Na D_1 lines to be ~ 1.8. Around the centre of the transit the planetary sodium absorption seems to be less deep than during the rest of the transit, of which a hint is also seen in the Snellen et al. (2008) data. If real, this could be caused by the change in the relative radial velocity of the planet with respect to that of the star, with the planet's absorption centred at the centre of the stellar absorption line during mid-transit. Furthermore, a change in the shape of the stellar absorption line from centre to limb might contribute to this effect. For the absorption by potassium in the atmosphere of HD 209458b, we find an upper 3-σ limit of 0.042% in a passband of 1.5 Å.

1.3 Summary and outlook

In this thesis we use different techniques to investigate stars and planets at high spatial and spectral resolution. In Chapter 2 of this thesis we describe a fast and cost-effective way to combine high-resolution spectroscopy with optical interferometry, by connecting an existing interferometer to an existing spectrograph. We also show in which research fields such an instrument will be particularly useful. The first results delivered by the Astronomical Multiple BEam Recombiner (AMBER) instrument at the VLTI, with a spectral resolution of R $\sim$ 12 000 in the near-infrared shows the great potential such an instrument could have. Currently the Vega (Visible spEctroGraph and polArimeter) project is under construction with a spectral resolution of R $\sim$ 30 000 at the Chara array, which is expected to deliver fascinating new results. However, both instruments have a bandpass of a few tens of nanometers. To use cross correlation techniques, which have proven very useful for optical spectroscopy, a wider bandpass is needed. In this way one would have the same observing possibilities for different areas on stellar surfaces as one has now for the integrated light form the stellar surface as a whole, albeit at the moment only for bright stars.

In Chapters 4 and 5 two studies are presented in which high spectral resolution instruments are used, and by which the high spatial resolution is achieved by taking advantage of the occurrence of eclipses (Rossiter-McLaughlin effect).

In Chapter 4 the relative orientation of the stellar rotation axes of the binary system V1143 Cyg are studied. Analysis tools are developed to disentangle the light coming from the foreground eclipsing star and from the eclipsed background star. In this way it is possible to achieve spatial resolution on sub-stellar surface scales across stellar absorption lines. The two analysis tools developed in this work, in particular the method which incorporates the shape change of the stellar absorption line, and not only the change of centre of gravity, will enable the direct measurement of a number of stellar parameters difficult to access otherwise. It will be possible to accurately disentangle between rotational broadening and broadening due to velocity fields on the stellar surface and possible differential rotation. High signal-to-noise spectra obtained during eclipses will enable us to calculate limb darkening coefficients, not only for wavelength bands, but also over stellar absorption lines. i.e. It may be possible to establish the difference in stellar lines forming at the limb of the stellar disk and the centre. The subsequent blocking of the central and limb parts of the eclipsed star makes it relatively straight forward to remove the broadening of the stellar lines due to rotation, and to effectively obtain spectra of the limb and centre of the eclipsed star at different times.

In Chapter 5 we use the newly developed tools to derive the relative orientation of the spin axes in the DI Herculis system. We find that there exists a strong misalignment between the stellar spin axes and the orbital spin. This brings the expected apsidal motion in agreement with the measured apsidal motion, but it raises new questions: How did DI Herculis obtain its misaligned axes? Was it 'formed' with misaligned axes, and if so, how did it maintain this misalignment during the pre-main sequence phase, during which tidal forces are stronger due to greater radii of the components? Or did this young system acquire its current state during an subsequent evolution by multi-body interaction? Was it ejected from a cluster, or did Kozai migration, via an undiscovered third body in the system, lead to its current state?

A second connected class of interesting questions raised by the presented results in Chapter 5 are connected to the question whether systems like DI Herculis, with misaligned angular momentum vectors, are rare or common. If more systems with misaligned axes exist, then it would be instructive to know whether this misalignment is a function of orbital period, orbital eccentricity, and/or the total mass and mass ratio in the system. These measurements would help to refine theories of star formation as they basically provide constraints on an observable so far unobtained for non-contact binaries. There have been measurements of the inclination of stellar spin axes in RS CVn type binaries which suggest some degree of misalignment in these systems (Glebocki & Stawikowski 1997), but there were also suggestions that binaries with semi-major axes $\lesssim 40$ AU all have their spin vectors aligned (e.g. Hale 1994). So far we are missing information to answer the questions pointed out above.

To measure the orientation of a stellar spin axis, the stellar disk needs to be spatially resolved. An instrument presented in chapter 2, which would be able to measure the orientation of stellar spin axes for a variety of stars along the main sequence, is not available yet. One can, however, exploit for short-period systems the RM-effect during eclipses, and for long-period systems one can use the AMBER instrument at the VLTI. With a spectral resolution of R $\sim 12\,000$ in the near-infrared one would be able to use the Brγ line to determine the orientation axes in O and B stars. It would be particularly interesting to do so for stars of the Sco OB2 association, also to measure a possible alignment of single stars in the association.

Our measurements of the atmosphere of the exoplanet HD 209458b, presented in Chapter 6, using a ground-based telescope are interesting for two important reasons. We extend earlier measurements of the atmosphere by targeting the two Na D lines separately and by setting an upper limit to potassium absorption in the atmosphere of HD 209458b. Secondly, our measurements are completely consistent not only with the earlier HST results, but also with data taken with a different telescope and a different spectrograph under different weather conditions (Snellen et al. 2008). This shows that reliable measurements of extrasolar planet atmospheres are possible with ground-based telescopes. Now is the time to extend these measurements to different wavelengths, e.g. in the near infrared and to planets around less bright host stars.

Bibliography

Bonnell, I., Arcoragi, J.-P., Martel, H., & Bastien, P. 1992, ApJ, 400, 579 3
Charbonneau, D., Brown, T. M., Burrows, A., & Laughlin, G. 2007, in Protostars and Planets V, ed. B. Reipurth, D. Jewitt, & K. Keil, 701 5
Charbonneau, D., Brown, T. M., Latham, D. W., & Mayor, M. 2000, ApJ, 529, L45 5
Charbonneau, D., Brown, T. M., Noyes, R. W., & Gilliland, R. L. 2002, ApJ, 568, 377 6
Chelli, A. & Petrov, R. G. 1995, A&AS, 109, 401 4
Churchwell, E. 2002, ARA&A, 40, 27
de Mooij, E. J. W. & Snellen, I. A. G. 2008, submitted A&AL 5
Domiciano de Souza, A., Zorec, J., Jankov, S., et al. 2004, A&A, 418, 781 4
Ghez, A. M., Neugebauer, G., & Matthews, K. 1993, AJ, 106, 2005 3
Glebocki, R. & Stawikowski, A. 1997, A&A, 328, 579 9

Goodwin, S. P., Kroupa, P., Goodman, A., & Burkert, A. 2007, in Protostars and Planets V, ed. B. Reipurth, D. Jewitt, & K. Keil, 133 3
Hale, A. 1994, AJ, 107, 306 9
Hébrard, G., Bouchy, F., Pont, F., et al. 2008, A&A, 488, 763 5
Heller, C. H. 1993, ApJ, 408, 337 3
Ida, S. & Lin, D. N. C. 2004, ApJ, 616, 567 5
Jensen, E. L. N., Mathieu, R. D., Donar, A. X., & Dullighan, A. 2004, ApJ, 600, 789 3
Knutson, H. A., Charbonneau, D., Allen, L. E., et al. 2007, Nature, 447, 183 5
Larson, R. B. 2003, Reports on Progress in Physics, 66, 1651 3
Lin, D. N. C., Bodenheimer, P., & Richardson, D. C. 1996, Nature, 380, 606 5
Machida, M. N., Tomisaka, K., & Matsumoto, T. 2003, in IAU Symposium, Vol. 221, IAU Symposium, 167 3
Mayor, M. & Queloz, D. 1995, Nature, 378, 355 5
McLaughlin, D. B. 1924, ApJ, 60, 22 4
Nagasawa, M., Ida, S., & Bessho, T. 2008, in IAU Symposium, Vol. 249, IAU Symposium, 279 5
Petrov, R. G. 1989, in NATO ASIC Proc. 274: Diffraction-Limited Imaging with Very Large Telescopes, ed. D. M. Alloin & J.-M. Mariotti, 249 4
Rasio, F. A. & Ford, E. B. 1996, Science, 274, 954 5
Rossiter, R. A. 1924, ApJ, 60, 15 4
Skemer, A. J., Close, L. M., Hinz, P. M., et al. 2008, ApJ, 676, 1082 3
Snellen, I. A. G., Albrecht, S., de Mooij, E. J. W., & Le Poole, R. S. 2008, A&A, 487, 357 7, 9
Winn, J. N., Noyes, R. W., Holman, M. J., et al. 2005, ApJ, 631, 1215 5
Wu, Y. & Murray, N. 2003, ApJ, 589, 605 5
Zinnecker, H. & Yorke, H. W. 2007, ARA&A, 45, 481 2

Chapter 2

A new concept for the combination of optical interferometers and high-resolution spectrographs

The combination of high spatial and spectral resolution in optical astronomy enables new observational approaches to many open problems in stellar and circumstellar astrophysics. However, constructing a high-resolution spectrograph for an interferometer is a costly and time-intensive undertaking. Our aim is to show that, by coupling existing high-resolution spectrographs to existing interferometers, one could observe in the domain of high spectral and spatial resolution, and avoid the construction of a new complex and expensive instrument. We investigate in this chapter the different challenges which arise from combining an interferometer with a high-resolution spectrograph. The requirements for the different sub-systems are determined, with special attention given to the problems of fringe tracking and dispersion. A concept study for the combination of the VLTI (Very Large Telescope Interferometer) with UVES (UV-Visual Echelle Spectrograph) is carried out, and several other specific instrument pairings are discussed. We show that the proposed combination of an interferometer with a high-resolution spectrograph is indeed feasible with current technology, for a fraction of the cost of building a whole new spectrograph. The impact on the existing instruments and their ongoing programs would be minimal.

S. Albrecht, A. Quirrenbach, R. N. Tubbs & R. Vink
AN to be submitted

2.1 Introduction

In recent years optical interferometers have proven that they can produce excellent science in the field of stellar and circumstellar astrophysics. Over the same period high-resolution spectrographs have enabled the discovery of the first extra-solar planets, and contributed substantially to great progress in the field of asteroseismology.

A number of current interferometric instruments have some spectroscopic capabilities. For example the mid- and near-infrared instruments MIDI (The Mid-Infrared instrument, at the VLTI) and AMBER (Astronomical Multiple BEam Recombiner, at the VLTI) provide spectral resolutions of up to $R \sim 250$ and $R \sim 12000$, over bandpasses of $\sim 5\ \mu m$ and ~ 50 nm, respectively. At the CHARA array, the Vega (Visible spEctroGraph and polArimeter) project is under construction with a spectral resolution of $R \sim 30000$ and a bandpass of ~ 50 nm. For science results obtained with spectrally resolved interferometry see for example Vakili et al. (1998) and Weigelt et al. (2007). Unfortunately the combination of very high spectral resolution over a bandpass greater than a few tens of nanometer, to enable a real analog to classical Echelle spectroscopy with interferometric spatial resolution is not yet available.

In building a dedicated high-resolution Echelle spectrograph for an existing interferometer such as the VLTI, one would face several challenges. First of all, building a high-resolution spectrograph is a very costly and time-intensive undertaking. In addition it would be hard to justify building such an instrument only for use with an interferometer, as current optical interferometers are still restricted to very bright objects in comparison with single telescopes. Furthermore, high-resolution spectrographs are usually large instruments, while the space available in the beam combining laboratories of interferometers is often limited. Therefore, it is unlikely that such a dedicated instrument will be built in the near future.

In this chapter we advocate a different approach. By using an existing spectrograph and only building an interface between it and an interferometer at the same site, the combination of high spectral and spatial resolution could be achieved on a much shorter timescale, and for a fraction of the cost of a complete new instrument.

The pre-existing infrastructure would need to consist of two telescopes, delay lines for path compensation, a fringe sensing unit to acquire and stabilize the fringes, and a high-resolution spectrograph on the same site. These conditions are already fulfilled, or will be fulfilled in the very near future, at several observatories. The two most promising sites are:

- In the Southern hemisphere at Paranal Observatory with the VLTI in combination with the UVES spectrograph at Unit Telescope 2 (UT2), or the High-Resolution IR Echelle Spectrometer (CRIRES) spectrograph at UT1.
- In the Northern hemisphere at Mauna Kea with the Keck Interferometer (KI) and HIgh Resolution Echelle Spectrometer (HIRES) at Keck I telescope or the NIRSPEC spectrograph at Keck II. Also at Mauna Kea, the OHANA (Optical Hawaiian Array for Nanoradian Astronomy) interferometer is currently under development, and will allow the combination of several other pairs of telescopes at the Manual Kea site.

In each case, three additional hardware components would be required:

1. A beam combiner that accepts two input beams from the telescopes and feeds the outputs carrying the fringe signals (coded as intensity variations) into fiber feeds;

2. Fibers that connect the interferometer to the spectrograph;

3. A fiber head that feeds the light from the fibers into the spectrograph.

If separate telescopes are available for interferometry (as in the case of the Auxiliary Telescopes of the VLTI), the impact on the single-telescope-use of the spectrograph would be minimal, as it could be used in the interferometric mode during times when other instruments are scheduled for use with the main telescope.

The outline of this chapter is as follows. In Section 2.2 the scientific motivation for the proposed setup will be discussed. Section 2.3 will give an overview of the challenges in designing and building the proposed instrument, and their possible solutions. In Section 2.4 we will give more information about the proposed combination of the VLTI with the UVES spectrograph, and its expected performance. Section 2.5 highlights the main points for other possible interferometer-spectrograph pairings, and Section 2.6 gives our conclusions.

2.2 Scientific case

By taking advantage of the existing infrastructure and instrumentation at the observatories, the proposed interface between a high-resolution spectrograph and an optical / near-infrared interferometer can provide some unparalleled capabilities in a time- and cost-efficient manner. Most importantly, interferometry can be performed with sufficiently high spectral resolution to resolve absorption lines allowing visibility changes across spectral lines to be measured even in late-type stars. The interferometric spectra would also cover a wide wavelength band. Using the broad spectral coverage, one would be able to use cross-correlation techniques to obtain very accurate radial-velocities and line shapes, which have proven extremely helpful in planet search programs and asteroseismology.

Although restricted to observations of relatively bright stars, interferometry at high spectral resolution will provide hitherto inaccessible information on stellar rotation properties, atmospheric structure and surface features, and can have a profound impact on a large number of open questions in stellar astrophysics.

2.2.1 Stellar diameters and limb-darkening

Measuring the variation of the stellar diameter with wavelength, or even better determining wavelength-dependent limb darkening profiles, can provide a sensitive probe for the structure of strongly-extended atmospheres of cool giant stars. Such data can be directly compared with predictions of theoretical models, and provide qualitative new tests of state-of-the-art three-dimensional stellar model atmospheres (Quirrenbach & Aufdenberg 2003). These models make predictions for the emergent spectrum at every point of the stellar disk. To compare model predictions with data from traditional spectroscopy, they have to be integrated over the full disk first. In contrast, interferometric spectroscopy gives access to the center-to-limb variation of the emergent spectrum, and is thus naturally suited to comparisons with model atmospheres.

A first step in this direction has been made with the Mark III and COAST interferometers and with aperture masking, by measuring the diameters of a sample of cool giant stars in filters centered on deep TiO absorption bands and filters in the nearby continuum (Quirrenbach et al.

1993; Tuthill et al. 1999; Quirrenbach 2001; Young et al. 2003). Many stars are found to be substantially larger in the TiO bands, and to have wavelength-dependent asymmetry. It is easy to understand the principle behind these effects: we effectively measure the diameter of the τ = 1 surface of the star, and the height of that surface varies with opacity and therefore with wavelength. In cool stars this variation may be so large (up to $\sim$ 10% of the stellar diameter for "normal" giants, even more for pulsating variables) that it can be observed as a variation of the effective stellar diameter with wavelength. The higher parts of the atmospheres are cooler, making the brightness distribution across the stellar surface in absorption bands more sensitive to asymmetries in the temperature distribution. The large spectral widths of the filters used for these interferometric observations average over many TiO absorption lines with different strengths. Interferometric high-resolution spectroscopy will provide much more detailed information on the diameter and limb darkening profiles as a function of TiO absorption depth, and thus substantially better constraints on the theoretical models.

Out of the giant stars which have been observed, the variations of the apparent diameter and limb darkening profile with wavelength are most pronounced in Mira stars. The instrument proposed here will enable detailed investigations of the pulsation and wind acceleration mechanisms. Again, high spectral resolution is required to sample a large range of depths in the stellar atmosphere. The advantage of combining high spatial- and spectral-resolution together in one observation of an object rather than using separate observations in this context has also been pointed out by e.g. Wittkowski et al. (2006); Tsuji (2006).

2.2.2 Interferometric Doppler Imaging

Classical Doppler Imaging (DI) has been developed into a very powerful tool (e.g., Rice 2002; Kochukhov et al. 2004). This technique allows mapping of the chemical and magnetic properties of stellar photospheres with surprisingly small details. Up to now, line profiles have been used for DI which are based on average atmospheric structures; this can obviously only be an approximation, in particular in regions of extreme abundance peculiarity. Tools are now available to compute such stellar atmospheres more accurately (e.g., Shulyak et al. 2004), and a reduced abundance contrast between spots and their surrounding is expected. Interferometric high-resolution spectroscopy data will allow a direct check of the models, because abundance analyses can be performed for individual surface regions of prominent chemically-peculiar stars. The same approach is also applicable for other stars with inhomogeneous surface properties, like active cool giant stars, as interferometry allows the study of individual surface regions. The fact that interferometry can isolate the active regions will partly compensate for the lower total signal-to-noise compared to single-telescope spectra, which always average over the whole stellar surface.

2.2.3 Pulsations and asteroseismology

Radial and non-radial stellar oscillations also lead to characteristic surface patterns of line shapes and central velocities. The reconstruction of these patterns from line profile variations alone is plagued with ambiguities, however. These can to a large extent be resolved by the additional phase information contained in interferometric data (Jankov et al. 2002). This means that pulsation modes can be identified uniquely without any need for comparisons with theoret-

ical models. Empirical mode identification with interferometric spectroscopy could become an important tool in the field of asteroseismology (Cunha et al. 2007).

2.2.4 Interpretation of radial-velocity variations

Radial-velocity observations of main-sequence stars have yielded more than 250 planet detections so far. The wealth of information from these surveys has revolutionized the field of planetary system physics, but little is known about the incidence of planets around stars with masses higher than about 1.5 $M_{\odot}$, because more massive main-sequence stars are difficult targets for radial-velocity observations. Surveys of K giants can provide this information, and planets around such stars have indeed been detected (Frink et al. 2002). Planets in highly eccentric orbits can be easily identified as such in high-precision radial-velocity data due to the distinct shape of the Keplerian velocity variations, but sinusoidal variations observed in a number of objects in ongoing radial-velocity surveys of K giants could be due either to planetary companions or to low-order non-radial g-mode pulsations. It is possible in principle to distinguish between these possibilities by analyzing the line shapes (which should vary along with the radial velocity in the case of pulsations, but remain stable in the case of companions), but this requires very high spectral resolution and signal-to-noise. Observations with interferometric spectroscopy could resolve the stellar disk and hence distinguish more easily between these possibilities, which would help to establish the mass function of planets around stars with masses between 3 and 5 $M_{\odot}$. Similar arguments apply to other cases in which radial-velocity variations could plausibly be attributed to different mechanisms, either related to stellar variability or to companions.

2.2.5 Cepheids and distance ladder

Limb darkening curves measured for a spectral line can provide direct measurements of the projection factors of Cepheid pulsations, which relate the true velocity of the pulsation to the observed radial-velocity curve. Uncertainties in this "p factor", which presently must be computed from theoretical models, are a serious limiting factor in current estimates of Cepheid distances with the Baade-Wesselink method (Sabbey et al. 1995; Marengo et al. 2002; Nardetto et al. 2006). Interferometric spectroscopy can thus eliminate one of the important contributions to the error budget for distances to Cepheids and other variable stars.

2.2.6 Orientation of stellar rotation axes

Stellar rotation induces a difference in the fringe phase between the red wings and the blue wings of stellar absorption lines in resolved interferometric observations. Measuring the position angle of the phase gradient allows determination of the orientation of the stellar axis on the sky (Petrov 1989; Chelli & Petrov 1995). More detailed modeling of the interferometric signal can also provide the inclination of the stellar rotation axis (Domiciano de Souza et al. 2004). High resolution spectroscopy will thus open a way to determine the orientation of stellar rotational axes in space.

To know the orientation of the stellar axes in space is of particular interest in double- or multiple-star systems. One can determine whether the rotation axes of binaries are aligned with

each other, and with the orbital rotation axes of the systems. The orientation of the rotational axes contains information about the origin and evolution of the system (see also Chapters 4 and 5).

One can also search for (partial) alignment of rotation axes in star forming regions and stellar clusters. Interactions between stars in multiple systems and other stars in a stellar cluster change the momentum of the systems.

The orientation of the stellar rotation axes will be of special interest for stars which harbor planets, since the mutual inclination between the orbital plane of the companion and the rotation axis of the star can provide insights into the formation and evolution processes of the planet. If the orbital evolution of planetary systems is dominated by few-body scattering processes, or Kozai migration, one might expect to find orbits that are not aligned with the stellar angular momentum (e.g., Lin & Ida 1997; Papaloizou & Terquem 2001; Wu & Murray 2003; Nagasawa et al. 2008). In the near future, astrometric orbits will become available from ground-based and space-based astrometry with the Phase-Referenced Imaging and Micro-arcsecond Astrometry (PRIMA) facility at the VLTI, the Space Interferometry Mission (SIM), and with GAIA. Combining this information with interferometric high resolution observations will provide the relative inclination between the orbital and equatorial plane for a large number of planets in a variety of orbits.

2.2.7 Differential stellar rotation

Along with the oscillation spectrum, differential rotation is a powerful diagnostic for the interior structure of a star. Unfortunately, observations of differential rotation are difficult with classical spectroscopy, and degeneracies exist between inclination, limb darkening, and differential rotation (e.g., Gray 1977). These degeneracies can be resolved by the additional information from interferometric spectroscopy (Domiciano de Souza et al. 2004). High spectral resolution is of the essence for this application, giving the proposed type of instrument a big advantage over more conventional interferometric spectrographs such as AMBER.

2.2.8 Circumstellar matter

Velocity-resolved interferometric observations of emission lines can be used to determine the structure and velocity field of disks around pre-main-sequence objects and Be stars (e.g. Quirrenbach et al. 1997; Young et al. 2003; Tycner et al. 2006; Meilland et al. 2007). It is possible to determine the disk opening angle and the rotation law in the disk, to measure the location of the inner edge of the disk, and to obtain detailed information on possible asymmetries caused by spiral waves. Interferometric observations of winds and outflows from pre-main-sequence stars and from evolved objects can be used to determine their extent and overall geometry, and to probe sub-structure such as clumps and shells. These observations will not need the full spectral resolution offered by high-resolution optical spectrographs, but access to the Hα line is of critical importance.

2.3 Instrument and infrastructure

In this section we describe our proposal for combining an optical/IR interferometer with a high-resolution spectrograph. Figure 2.1 shows a schematic drawing of the combined instrument, while a possible design for the beam combiner is shown in Figure 2.2. Special attention is given to longitudinal dispersion compensation (Section 2.3.2). This has to be addressed if one wants to perform long integrations (several minutes) over a wide bandpass, one of the key abilities of the proposed instrument.

2.3.1 Telescopes

The Earth's atmosphere distorts planar incoming wavefronts from an unresolved astronomical source, introducing phase fluctuations as a function of position and time (Roddier 1981). These fluctuations are commonly described by a Kolmogorov spectrum (Tatarski 1961; Kolmogorov 1941) with constant Fried parameter r_0 (Fried 1966). In order to obtain stable complex visibilities, the incoming stellar wavefronts at the beam combiner have to be flat (with constant wavefront phase as a function of position in the pupil plane for an unresolved star). This can be achieved using either:

1. telescope aperture diameters small enough that the atmospherically-induced phase variations are negligible with $D/r_0 \leq 1$ (this may require a variable pupil stop);

2. tip-tilt correction making wavefront errors negligible on aperture diameters up to $D/r_0 \simeq 3$; or

3. higher-order adaptive optics.

Larger apertures can be used at longer wavelengths or under better seeing conditions, as the Fried parameter varies as $r_0 \propto \lambda^{6/5}$ and $r_0 \propto 1/\mathrm{FWHM}_{seeing}$ for observations at a wavelength λ and with a seeing disk of FWHM_{seeing}.

2.3.2 Longitudinal dispersion compensation

To compensate for the difference in path length from the two telescopes to the source, optical path must be added to one arm of the interferometer. This is typically achieved through the use of *optical trombone* delay lines or through the stretching of optical fibers (Monnier 2003). If the optical delay compensation is performed in a dispersive medium, the Optical Path Difference (OPD) where the fringes are found will vary with wavelength. Longitudinal dispersion can affect the OPD in the proposed instrument concept in two ways:

1. Dispersion will give a variation of optical delay across the wavelength range of the spectrograph;

2. If the spectrograph operates in a different waveband from the fringe tracker, dispersion will introduce a different OPD in the spectrograph waveband to that in the fringe-tracking waveband.

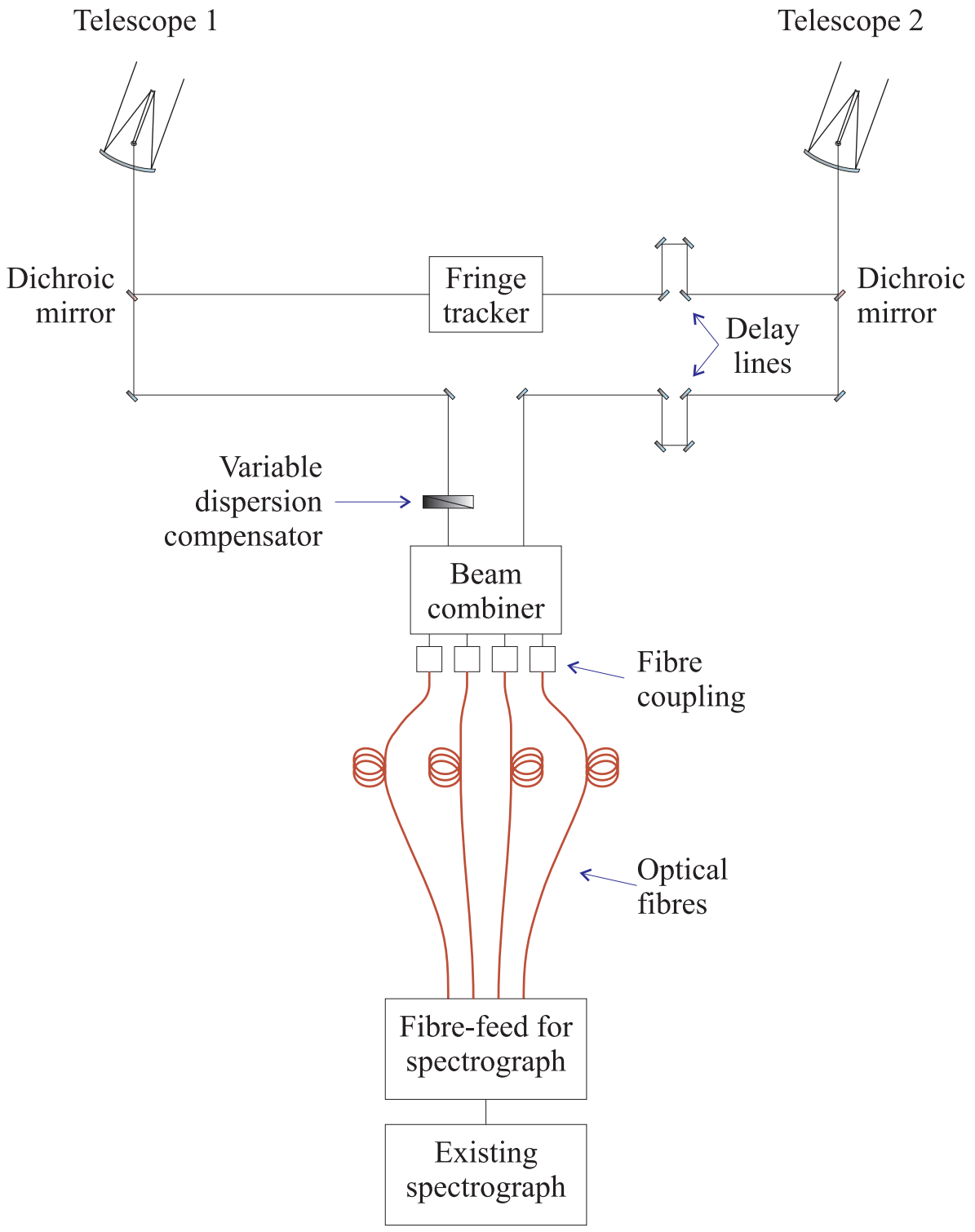

Figure 2.1 — Schematic of the combined instrument, interferometer and spectrograph. The proposed instrument relies on pre-existing infrastructure (telescopes, fringe-tracker, delay lines and a spectrograph located within a few hundred meters). The additional components which must be built include the variable dispersion compensator, beam combiner, fiber coupling, optical fibers and fiber-feed for the spectrograph.

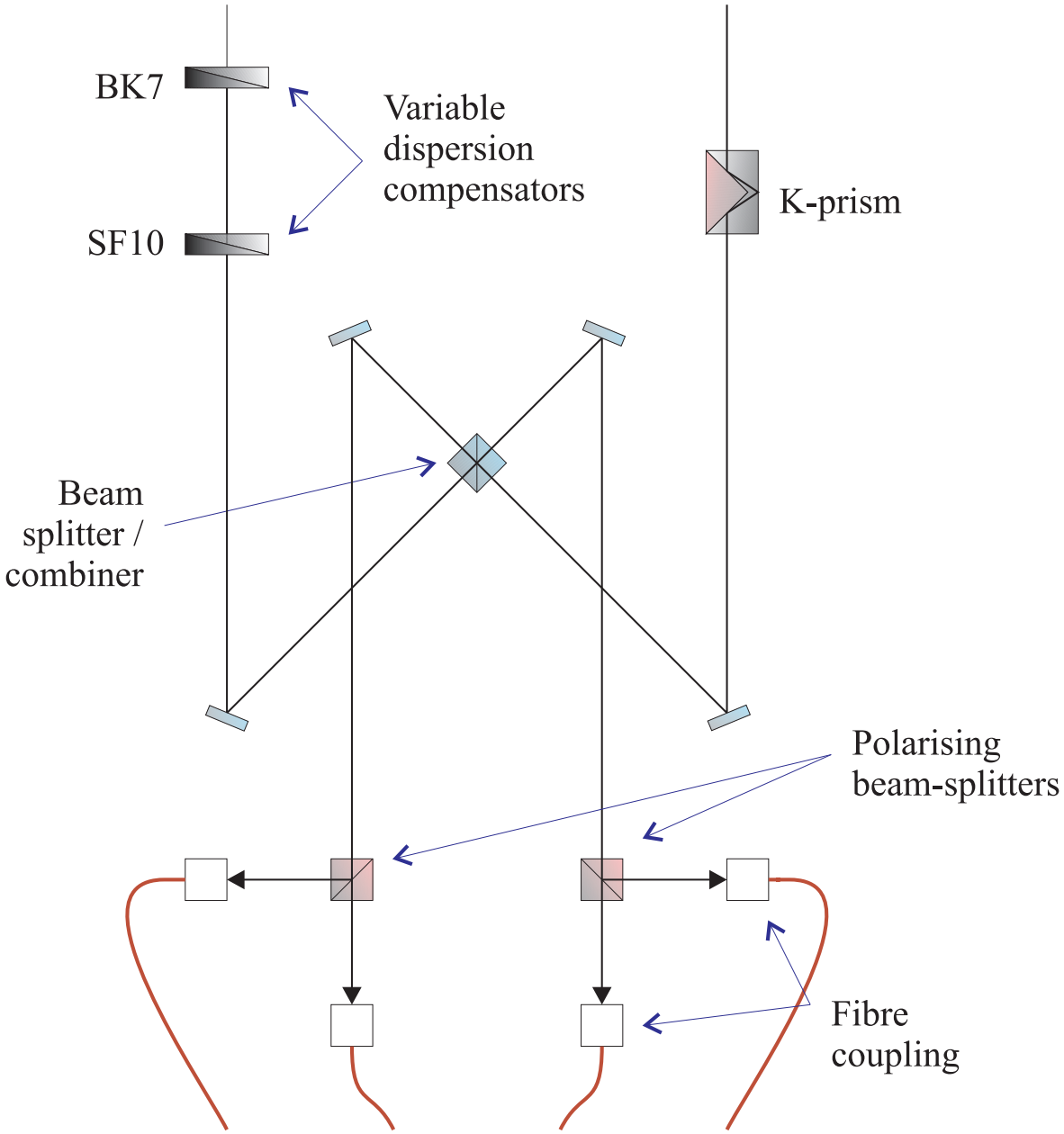

Figure 2.2 — Schematic of the suggested beam combiner for the coupling of a spectrograph to an interferometer. The beam from one telescope passes through a K-prism which introduces an achromatic phase shift of $\pi/2$ between the s and p polarizations. The beam from the other telescope passes through longitudinal dispersion compensators. The combination of the two beams in the beam-splitter introduces a phase shift of π between the two output beams. The two polarizations of the two output beams are separated by the polarizing beam-splitters, resulting in four beams with phase relations of 0, $\frac{\pi}{2}$, π, $\frac{3\pi}{2}$ entering the fibers.

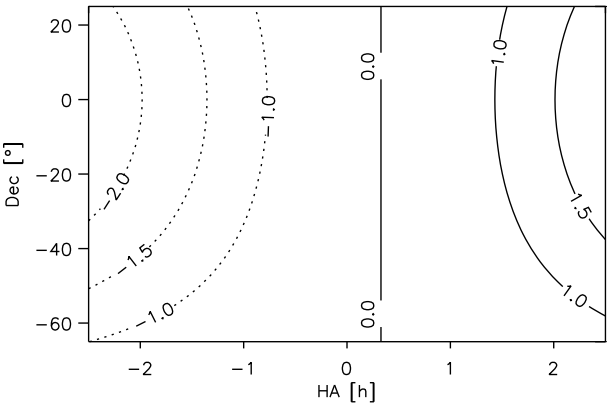

Figure 2.3 — Change (in m) of OPD during a 10 minute integration as a function of HA and Declination for the G1-J6 AT stations at the VLTI which form a baseline of a length of 192 m and an orientation angle of $-2°$. An angle of $0°$ would indicate a baseline directed towards the North.

For a typical high-resolution spectrograph the coherence length of the fringes in each spectral channel is much larger than the optical delay offsets introduced by dispersion. However, time-variation of the dispersion effects during a spectrograph detector integration will blur the interference fringes, reducing the measured visibility amplitude. The two principal sources of variation in optical delay due to dispersion are:

I During an observation the position of the object on the sky changes. To keep the interference fringes at a stable position, the additional optical path introduced in one arm of the interferometer must be varied as the Earth rotates. The change in optical path through the dispersive medium in one arm of the interferometer causes the visibility phase to vary differently at each wavelength. During the course of an observation of several minutes this inevitably leads to a loss of fringe contrast for observations in a waveband of non-zero bandwidth. For example, during a 10-minute visible-light integration, the geometric delay path can change by several meters (see Figure 2.3 and Figure 2.4), which would lead to a relative OPD shift of several μm between R band and I band.

II A change in the temperature or humidity of the air in one of the optical paths to the star will introduce a change in the column density of air and/or water vapor. To first order, these changes will be corrected by the fringe tracking. The residuals are not expected to be large enough to give different delays for different spectral channels in the spectrograph bandpass. However, if the spectrograph is operating in a different waveband from the fringe tracker, the optical delay in the spectrograph waveband may differ from that in the fringe tracking waveband.

Both dispersion problems could be circumvented by restricting the exposure time, but this would reduce the observational efficiency, and in the read-noise limited regime it would reduce the limiting magnitude. Reducing the spectral bandwidth would solve point I above, but would limit the spectral coverage of the observations. As one can see in Figure 2.3 and Figure 2.4, the change in OPD depends on the declination of the star and on the alignment of the baseline with the rotation axis of the earth. Therefore, restricting the baseline geometry and restricting the selection of sources would also circumvent point I above. This would seriously reduce the usefulness of the proposed instrument.

A better way to address point I above would be to equip the beam combiner with a variable atmospheric dispersion compensator (see e.g. Section 2.4.3). This dispersion compensator

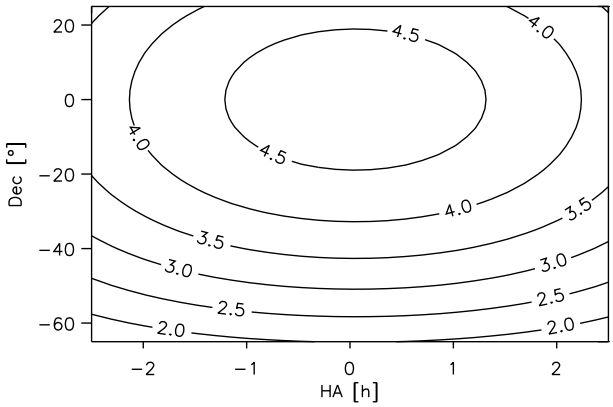

Figure 2.4 — Same as Figure 2.3, but this time with a baseline of 109 m length and an angle of 88° (C1-J2).

would correct for the differential dispersion introduced by the few meters of additional path between the two telescopes added during the course of the observations; it does not need to correct for the full differential air path.

Point II can be addressed by estimating the dispersion at the wavelength of the spectrograph using measurements of the ambient environmental conditions (Albrecht et al. 2004) and the variation of optical delay with wavelength across the fringe-tracking bandpass. If the fringe tracker cannot operate sufficiently far from the zero optical group-delay point, then an additional delay line will be required in order to provide a different geometrical delay for the spectrograph than is used for light that is sent to the fringe tracker, as shown in Figure 2.1.

2.3.3 Fringe tracker

The proposed instrument scheme relies on the interferometer having a fringe-tracking capability. The fringe tracking must keep the fringes of the spectroscopic observation stable even if they are observed at a different wavelength to the one used for fringe tracking. The fringes in the spectroscopic instrument must be kept stable to a fraction of a wavelength (typically ~ 1 rad of visibility phase). A number of existing interferometers already have fringe-tracking instruments (Delplancke 2003; Colavita et al. 2004; McAlister et al. 2004). The RMS noise (the jitter) in the optical delay from the fringe tracking will cause a reduction in the visibility amplitude by a factor γ:

$$\gamma = \exp\left(-2\left(\frac{\pi\sigma_d}{\lambda}\right)^2\right) \tag{2.1}$$

where σ_d is the RMS variation in the optical delay compensation in a spectral channel with wavelength λ during a detector integration.

2.3.4 Beam Combiner

The primary observable in an interferometer is the complex visibility (having amplitude and phase), proportional to the complex coherence function of the radiation received by the two telescopes (Quirrenbach 2001). The complex visibility can be derived in a number of ways,

for example using a fixed delay offset and measuring the fringe signal as a function of wavelength in the spectrum (Labeyrie 1975). Alternatively, to obtain the full information on the complex visibility in each spectral channel, one can measure the four fringe quadratures at each wavelength, i.e. measure the light intensity with fringe phase offsets of 0, $\pi/2$, π and $3\pi/2$ radians. The normalized light intensities as a function of wavelength λ in these four outputs are commonly called $A(\lambda)$, $B(\lambda)$, $C(\lambda)$, and $D(\lambda)$ respectively. The $A(\lambda)$, $B(\lambda)$, $C(\lambda)$, and $D(\lambda)$ outputs can be produced using 50% beam-splitter(s) (providing a π phase shift between the output beams) and achromatic $\pi/2$ phase shifts in two of the four output beams (see e.g. Figure 2.2). The complex visibility $V(\lambda)$ in the spectral channel at wavelength λ is then fully described by the four intensities $A(\lambda)$, $B(\lambda)$, $C(\lambda)$, and $D(\lambda)$:

$$V(\lambda) = 2 \cdot \frac{A(\lambda) - C(\lambda)}{A(\lambda) + B(\lambda) + C(\lambda) + D(\lambda)} + 2i \cdot \frac{B(\lambda) - D(\lambda)}{A(\lambda) + B(\lambda) + C(\lambda) + D(\lambda)}, \tag{2.2}$$

where $i = \sqrt{-1}$.

The squared amplitude of this visibility estimate $|V(\lambda)|^2$ and the argument (fringe phase) $\phi(\lambda)$ are given by:

$$|V(\lambda)|^2 = 4 \cdot \frac{(A(\lambda) - C(\lambda))^2 + (B(\lambda) - D(\lambda))^2}{(A(\lambda) + B(\lambda) + C(\lambda) + D(\lambda))^2},$$
$$\phi(\lambda) = \arctan \frac{A(\lambda) - C(\lambda)}{B(\lambda) - D(\lambda)}. \tag{2.3}$$

Applying the fringe estimators on a wavelength-by-wavelength basis, one can thus derive the complex visibility as a function of λ.[1]

The absolute phase will usually be corrupted by turbulence in the Earth's atmosphere, but differential phases can be measured between adjacent spectral channels or between the fringe tracking wavelength and one of the observed spectral channels. These differential phases can provide very valuable observables, such as phase differences between the red and blue wings of spectral lines. In sources which are resolved in some spectral lines but which are un-resolved at continuum wavelengths (e.g. Be stars, as discussed in Section 2.2.8), the complex visibilities can be used to make interferometric images of the structure in the spectral lines, using the position of the unresolved continuum source as the phase reference. In this context it is worth noting that phenomena on scales much smaller than the 'resolution limit' λ/B of the interferometer with baseline B are accessible with this technique, because differential phases with a precision of a few degrees provide astrometric accuracy significantly higher than the conventional (imaging) resolution limit.

[1] Note that the estimator for $|V(\lambda)|^2$ in Eqn. 2.3 is biased — $|V(\lambda)|^2$ will be over-estimated in the presence of noise. Slightly modified estimators can be used to give unbiased estimates of $|V(\lambda)|^2$ (e.g., Shao et al. 1988).

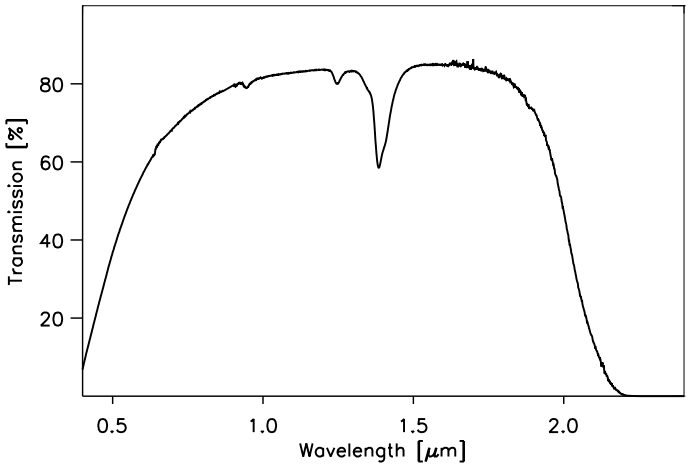

Figure 2.5 — Transmission in the wavelength range from 0.4 to 2.5 μm for 150 m of Optran Plus WF fiber (Ceramoptec catalog, see http://www.ceramoptec.com/catalog.htm).

2.3.5 Connection to the spectrograph

The outputs from the beam combiner can be easily transported to the spectrograph using multi-mode fiber optics. Only the light intensity as a function of wavelength is of interest at this point (after beam combination), so the additional optical path length and longitudinal dispersion from the fiber are unimportant.

For a link at visible or near-infrared wavelengths one could for example use the Optran Plus WF fiber with a core diameter of 100 μm (see Figure 2.5). Fluoride glass fibers could provide better throughput at longer near-infrared wavelengths.

The insertion of pick-off mirrors might provide a good solution for directing the light from the fibers into the spectrograph. However, in some infrared slit spectrographs, the slit is located in a cryogenic part of the instrument. If it is undesirable to make modifications inside the cryogenic Dewar, it may be sufficient to place the fibers in an image plane outside the spectrograph Dewar.

If the spectrograph is already a fiber-fed instrument, the number of new components will be small and the installation fast.

2.4 An illustrative example: UVES-I

In this section we investigate in more depth the possible combination of the VLTI interferometer with the UVES spectrograph. We name this combination *UVES-I* in the reminder of this chapter. In particular we address here the matter of external fringe tracking and dispersion compensation in Sections 2.4.2 and 2.4.3, respectively. As mentioned above it is essential to solve these points if one wants to combine a high-resolution Echelle spectrograph like UVES with an optical interferometer like VLTI and carry out long exposures, which has not been done so far.

2.4.1 VLTI Auxiliary Telescopes

UVES-I would operate in the wavelength range between 0.6 μm and 1.0 μm. Therefore it would use the VLTI ATs (1.8-m Auxiliary Telescopes) and not the UTs (8-m Unit Telescopes) as the Multi Application Curvature Adaptive Optics (MACAO) adaptive optics systems of the UTs do not deliver well-corrected wavefronts in the visible.

The existing tip-tilt correction on the ATs would allow the use of $3r_0$ sub-apertures with UVES-I (corresponding to ~ 75 cm at 800 nm under typical seeing conditions). With the planned installation of adaptive optics systems at the ATs, their full 1.8 m apertures would become useable for UVES-I, corresponding to a sensitivity gain of ~ 2 mag.

The ATs currently have a dichroic beam-splitter sending the visible light to the tip-tilt system, and passing the infrared light to the delay lines and instruments. This beam-splitter reduces the VLTI transmission in the visible considerably (Puech & Gitton 2006). For UVES-I this dichroic should be replaced by 10-90 beam-splitter, with only 10% of the visible light used for tip-tilt correction. The astronomical targets of interest are all bright enough that they will still give good tip-tilt performance. The sensitivity estimates given in Section 2.4.6 are based on this change, and assume a total VLTI transmission of 6% (Puech & Gitton 2006).

2.4.2 Fringe tracking with PRIMA

Starlight at wavelengths longward of 1.5 μm will be separated using a dichroic mirror and sent to the PRIMA fringe tracker (see Figure 2.2) for stabilization of the fringes. If the R-band fringes at the beam combiner can be stabilized to less than one radian of fringe phase long integrations ($\gg$ than the atmospheric coherence time) can be performed. In order to stabilize the fringe phase at R-band, the OPD at R-band must be calculated from the measured environmental conditions in the VLTI and the measured phases in the PRIMA spectral channels (1.95–2.45 μm).

For the case of von Karman turbulence (Goodman 1985) with finite outer scale L_0, the spatial structure function for the optical phase D_Φ asymptotically approaches a maximum value of $D_\Phi(\infty)$ (Lucke & Young 2007):

$$D_\Phi(r) \equiv \left\langle \left| \Phi(r') - \Phi(r'+r) \right|^2 \right\rangle \rightarrow D_\Phi(\infty), \text{ as } r \rightarrow \infty \tag{2.4}$$

For von Karman turbulence, Lucke & Young (2007) give a possible range of:

$$0.0971 \left(\frac{L_0}{r_0}\right)^{5/3} < D_\Phi(\infty) < 0.173 \left(\frac{L_0}{r_0}\right)^{5/3} \tag{2.5}$$

The total contribution of seeing to OPD fluctuations is typically estimated by assuming that the seeing is caused by a wind-blown Taylor screen of frozen turbulence passing the interferometer array telescopes at a velocity v (Taylor 1938; Buscher et al. 1995). Under this assumption, the asymptotic value of the temporal structure function will be equal to the asymptotic value of the spatial structure function:

$$D_\Phi(t) \equiv \left\langle \left| \Phi(t') - \Phi(t'+t) \right|^2 \right\rangle \rightarrow D_\Phi(\infty), \text{ as } t \rightarrow \infty \tag{2.6}$$

For a typical value of $r_0 = 0.25$ m at 800 nm wavelength and $L_0 = 22$ m (Martin et al. 2000) this would lead to a mean-square optical phase variation $D_\Phi(\infty)$ of:

$$170 \text{ radians}^2 < D_\Phi(\infty) < 300 \text{ radians}^2 \tag{2.7}$$

For a two-telescope interferometer with a long baseline, the mean-square variation in fringe phase will be up to twice as large. As this corresponds to fringe motions of several wavelengths, active fringe tracking will be required in order to perform long integrations.

The OPD fluctuations caused by astronomical seeing can be split up into two constituent parts:

1 variations in the mean particle density due to temperature fluctuations (temperature seeing, with no change in the air composition); and

2 replacement of dry air with an equal particle density of water vapor (water vapor seeing, with no change in particle density).

Measurements using the MIDI 10 μm instrument at the VLTI indicate that the differential column density of water vapor typically varies by an RMS of $\lesssim 1$ mole m^{-2} (Meisner 2007) due to water vapor seeing (the displacement of dry air by an equal particle density of water vapor). This introduces a mean-square fringe phase fluctuation of up to 50 rad^2 at 800 nm wavelength. The remaining 290–600 rad^2 of mean square phase variation result from temperature seeing[2].

If fringe tracking is performed at K-band, the fringes will be partially stabilized in R-band and I-band. Figure 2.6 shows plots of the refractivities of dry air and water vapor, normalized to unity at a fringe-tracking wavelength of 2.2 μm. The black *dry air* curve shows the relative amount of OPD at each wavelength if temperature seeing in a dry-air atmosphere introduced 1 unit of OPD at 2.2 μm. For air of finite humidity, the plot of the relative amount of fringe motion would be shifted linearly a small amount ($< 1\%$ of the way) towards the blue *water vapor* curve.

If the geometrical path length is varied in order to stabilize the fringes at K-band against temperature seeing, and no additional compensation is applied to account for the different refractivity in the visible, the correction applied will be 0.5–1.5% too small to stabilize the fringes between 600 and 900 nm. For the 288–602 radians^2 of mean square phase variation expected from temperature seeing, this will lead to an RMS fringe-tracking error of 0.1–0.4 radians at 800 nm wavelength.

The red curve in Figure 2.6 shows the relative effect of water vapor seeing at different wavelengths. It corresponds to the difference in refractivity between air and water vapor of the same (low) density, with the curve normalized to be unity at 2.2 μm (the fringe-tracking wavelength). A mean-square fringe phase fluctuation of $\simeq 50$ radians^2 due to water vapor seeing at 800 nm wavelength will correspond to $\simeq 0.90$ μm RMS motion at 800 nm wavelength, but from Figure 2.6 it can be seen that the fringe motion due to the water vapor seeing will always be 15% larger at 2.2 μm. If K-band fringe tracking is performed with no compensation for the different air refractivity in the visible, this will introduce an RMS residual of $\simeq 1$ radian to the

[2] A small fraction of the water vapor column density fluctuations is expected to occur within the VLTI, but this can be ignored when estimating the atmospheric contribution to the temperature seeing.

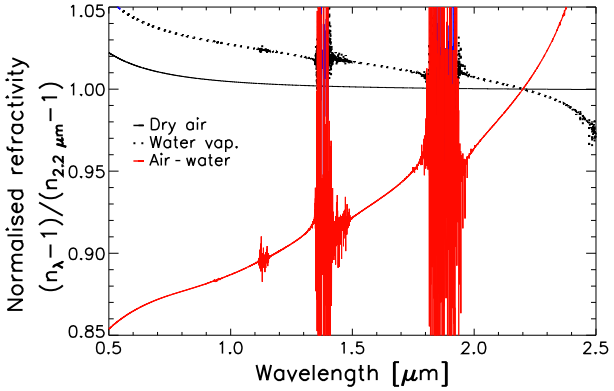

Figure 2.6 — Normalized refractivities of air and water vapor, plotted in black and blue respectively. The refractivity (equal to $n-1$ where n is the refractive index) is plotted against wavelength for dry air and water vapor. The refractivity curves have been normalized in this plot such that the refractivity value at 2.2 μm is unity. Also plotted in red is a curve of the refractivity of dry air minus the refractivity of water vapor, which has been normalized in the same way. The normalization process stretches this curve vertically. The data were taken from Ciddor (1996) and Mathar (2004)

fringe phase at 800 nm wavelength. This would cause a reduction of the fringe visibility due to blurring of the fringes in long exposures.

The approach described by Meisner (2007) for N-band fringe stabilization using PRI-MA can be adapted to improve R- and I-band fringe stabilization during fringe phase tracking. In this method, the geometric path from the star and the differential column density of dry air are estimated from the position of the optical delay lines and measurements from environmental sensors in the VLTI (Albrecht et al. 2004). The K-band group phase measurements provided by the PRIMA instrument are only very weakly dependent on the differential column density of dry air, but are strongly dependent on the differential column density of water vapor. If the effect of the estimated dry-air column density is subtracted from the measured group phase, the resulting group phase can provide a good estimate of the water vapor column density. The fluctuations in the measured water vapor column density can then be used to calculate and independently correct the residuals produced by water vapor and dry air seeing, assuming that the drift in the geometric delay error is small during one integration.

Analyses of temperature, pressure and absolute humidity data taken on 4 nights immediately following the installation of the four humidity and temperature sensors at Paranal (Albrecht et al. 2004) show that the square root of the temporal structure function of the density of air molecules typically varies by less than 0.003 moles m^{-3} (see Figure 2.7) at all measured locations within the VLTI, during a 2-minute integration. There is no measurable correlation between the fluctuations in the different ducts to the telescopes and the fluctuations in the main delay tunnel on timescales of a few minutes. The observed water vapor fluctuations within the VLTI are less than 3×10^{-4} moles m^{-3} over a 2-minute integration, and are already included in the $\lesssim 1$ mole m^{-2} figure from Meisner (2007).

In the extremely pessimistic case that all the air in an entire 100-m duct simultaneously undergoes the same 0.003 moles m^{-3} density change, 2 μm of OPD would be introduced at a wavelength of 2.2 μm. The light paths at the VLTI pass through two such ducts and through an air-filled main delay line, but the total OPD fluctuation due to density changes within the

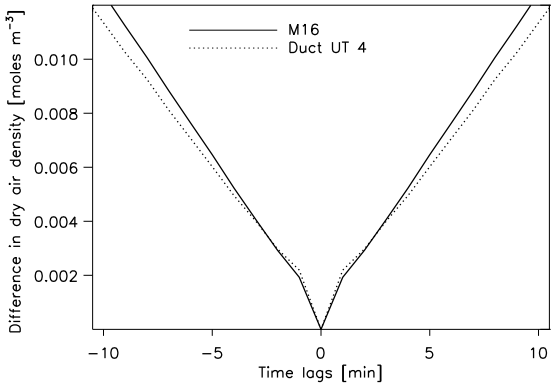

Figure 2.7 — Square root of the temporal structure function of the dry air density at two locations in the VLTI for the Night 22/23 September 2004. The solid line shows the temporal structure function for measurements at the M16 mirror in front of the interferometric laboratory, and the dashed line displays the same measurements inside the light duct towards the UT 4 telescope.

VLTI is still expected to be much smaller than the figure of 24–33 μm RMS OPD estimated above for temperature seeing in the atmosphere. The measurements of K-band fringe phase and group phase include the complete path through the atmosphere and instrument as far as the PRIMA optical bench, so OPD fluctuations caused by changes in the ambient conditions within the VLTI will be accurately tracked.

The expected fringe tracking noise introduced by the PRIMA instrument itself will be 100 nm for a star with $m_K = 8$, and 50 nm at $m_K = 6$ (see Figures 5-12 of Delplancke (2003), and Tubbs et al. (2007)). Equation 2.1 gives visibility losses of 27% and 7.5% respectively at 800 nm, which is easily tolerable.

2.4.3 Dispersion compensation for UVES-I

Each meter of unbalanced air path introduces (under median Paranal atmospheric conditions) offsets from the K-band group delay zero-point of 108 nm and 412 nm, respectively, for the fringes at 900 nm and 600 nm wavelength. This fringe motion can be accurately predicted from environmental sensor measurements and the known geometrical delay. It can be stabilized at one wavelength using a delay line, but to give good stabilization over the full 900 nm to 600 nm wavelength range, a variable dispersion corrector is required.

Starlight at wavelengths shorter than 1.5 μm is separated from the K-band fringe tracking light by a dichroic mirror into the dispersion compensator. The dispersion compensator and the beam combiner are located on the same optical table as PRIMA to ensure alignment and OPD stability (see Figure 2.2).

Viable solutions for a single-material dispersion compensator exist. Using data from the Schott catalog (http://us.schott.com/sgt/english/products/listing.html), the Sellmeir dispersion formula (e.g. Berger et al. 2003), and Cramer's rule we find that, for the 0.6-μm to 1-μm wavelength range SF10 glass can be used (see Figure 2.8, upper panel). For extreme parameters — a build up of 10 m delay during integration, compare also to Figures 2.3 and 2.4 — the residual uncompensated optical path length would reach 150 nm, however; therefore an arrangement where two different materials are used for the dispersion compensation is preferred. A combination of fused silica and BK7 glass gives the best theoretical performance, but the required glass thickness is relatively high (see Figure 2.8, lower panel). We therefore favor a SF10/BK7 combination, which provides compensation to 70 nm even for extreme delay rates, using much thinner glass elements (see Figure 2.8, middle panel). The variable dispersion compensator will also compensate for the fixed additional dispersion produced in the K-prism.

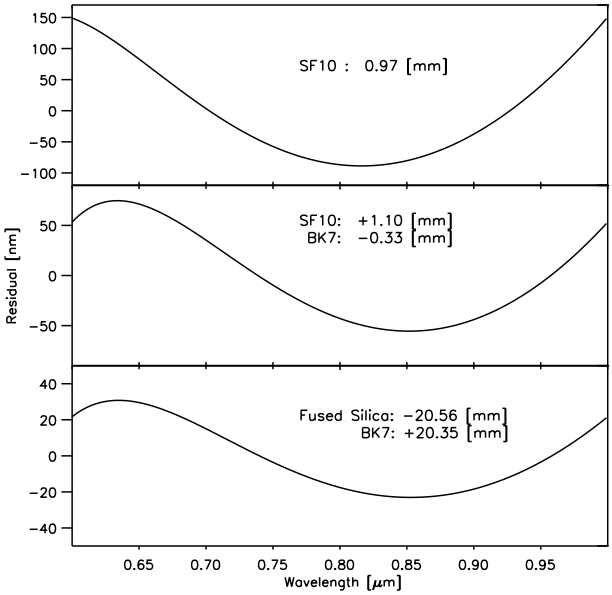

Figure 2.8 — Residual dispersion after accumulation of a 10 *m* change of the total delay, using atmospheric dispersion compensators made of: a] SF10; b] SF10/BK7; and c] BK7/Fused Silica. The combination of SF10 and BK7 (b]) could be used for an instrument like UVES-I. The thickness of the material needed for the compensation is also indicated. For example an additional air path of 10 m in one beam would require the insertion of a 0.97 mm SF10 glass in the other beam.

In addition to the compensation of the delay differences in the visible band, we must also compensate the delay difference between the visible band and the K-band, where PRIMA tracks the fringes. This can be done by commanding the PRIMA fringe tracker to fringe track far enough from the K-band group delay zero point to allow compensation of the fringes at visible wavelengths, or alternatively by inserting another additional delay as shown in Figure 2.1.

2.4.4 Beam combiner for UVES-I

One beam is sent through an achromatic phase shifter (e.g. K-prism), which introduces a $\pi/2$ phase shift of one polarization state with respect to the other. Variable dispersion compensation is applied in the other beam. The dispersion introduced by the K-prism is also compensated in the dispersion compensator. Two flat mirrors then direct the beams into the main beam combiner (Figure 2.2). The combined beams, which have a phase shift of π relative to each other, are sent to polarizing beam-splitters by a second pair of flat folding mirrors (see Figure 2.2). The polarizing beam-splitters separate the two linear polarizations (with their $\pi/2$ phase differences) giving the four fringe quadratures $A(\lambda)$, $B(\lambda)$, $C(\lambda)$, and $D(\lambda)$.

Full information on the complex visibility can be obtained from the four fringe quadratures $A(\lambda)$, $B(\lambda)$, $C(\lambda)$ and $D(\lambda)$ as discussed in Sect. 2.3.4. For an ideal beam combiner, the complex visibility can then be calculated for each spectral channel using Eqn. 2.2.

The requirements on the precision of the phase shift are rather loose; one can easily tolerate up to 10° errors as long as they are stable. Errors in the phase shifts can be compensated for in software, using a similar approach to that used for phase measurements with the PRIMA instrument (Tubbs et al. 2007). Similarly, there are no stringent requirements on the splitting ratios and polarization purity of the beam-splitter cubes. It is therefore possible to mostly use standard commercial components. A preliminary design of the beam combiner fits on a 45 cm $\times$85 cm breadboard (see Figure 2.9). This compact design ensures stability and minimizes the space taken up in the beam-combination laboratory of the interferometer. Due to its high spectral resolution, the coherence length of UVES-I is very large ($\geq$ 3 cm). However, the drift of the optical

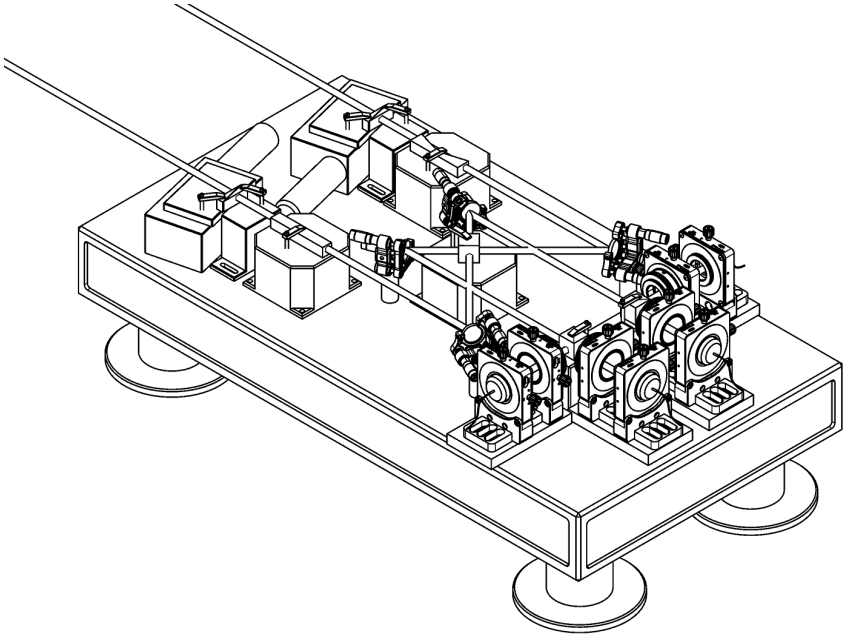

Figure 2.9 — UVES-I beam combination table. The light beams from the two telescopes enter from the top left, and pass through the atmospheric dispersion compensator and achromatic phase shifter before being combined at the central beam combiner. The two polarization states are separated, and the resulting four beams coupled into optical fibers; the four fiber holders are visible at the bottom right.

path difference *during* one exposure must not be larger than ~ 50 nm, as this would reduce the fringe visibility due to the fringe blurring; therefore the UVES-I breadboard should be mounted as rigidly as possible to the fringe sensing unit. This eliminates the necessity of an additional metrology system.

2.4.5 UVES instrument on UT-2

The impact of the proposed combination on the UVES instrument would be small. The UVES-I fiber interface to the spectrograph will be similar to the existing link from FLAMES (Fiber Large Array Multi Element Spectrograph) to UVES (Pasquini et al. 2000), which has a fiber head for 8 fibers. The UVES-I fiber head will be placed after the pre-slit optics and can, when UVES-I is used, be injected via a folding mirror.

To retrieve the full interferometric information only four fibers are needed. It would thus be possible to use two VLTI baselines simultaneously if an eight-fiber feed is used. This would require both of the PRIMA fringe-tracking units to stabilize the fringes on the two baselines. Interesting, but currently not possible at Paranal for an instrument like UVES-I, is the simultaneous use of three baselines, which would make it possible to measure a triangle of baselines, and aquire closure phase. For this a three-way beam combiner, with 12 output fiber is needed and the light from these fibers has to be directed on the spectrograph CCD with sufficiently-low cross-talk between the different orders.

As the light is injected via fibers into the spectrograph the spectral resolution achieved by the instrument no longer depends on the slit size, but on the core diameter of the fiber and

the re-imaging optics. For example using a fiber with a core diameter of 100 μm, the fiber whose transmission is shown in Figure 2.5, and with re-imaging optics changing the F/3 fiber output beam into the F/10 beam similar to that produced by the standard pre-slit optics of UVES (Dekker et al. 2000), a spectral resolution of $\sim$ 55000 for UVES-I would be achieved, while still making alignment of the fiber-couplers easy.

2.4.6 Performance

The detector integration times used should be sufficiently long to ensure that the detector read-noise is not dominant (see below), and sufficiently short to allow compensation of the atmospheric dispersion accumulating during the exposure with a relatively simple device (see Section 2.3.2). This will typically give exposure times between 1 min and 15 min.

The beam combiner has 12 optical surfaces (before fiber coupling). The transmissive optics will be covered with anti-reflection coatings optimized for the wavelength range used, while mirrors will be coated in protected silver. Using a conservative assumption of 95% efficiency per mirror surface and 99% efficiency per anti-reflection coated glass element, the resulting overall throughput of the beam combination table is 72%.

The transmission of the fiber link depends on the fiber coupling efficiency as well as the bulk transmission losses in the fiber. The fiber link will be similar to the fiber link of FLAMES but the fiber length will be larger, about 150 m compared to 40 m for the FLAMES-UVES link. In Figure 2.5 the transmission for 150 m of Optran Plus WF fiber is given. Note that the transmission changes from 55% to 80% between 0.6 μm and 1.0 μm

Assuming two optical surfaces at each end of the fiber couplers plus one folding mirror which can inject the light into UVES while the spectrograph is in interferometric mode, and the transmission efficiencies described above, the total transmission of the UVES-I link will vary from 45 % to 65 % over the 0.6 μm–1.0 μm wavelength band used.

The system visibility of an interferometer, i.e., the fringe contrast measured on an unresolved source, depends on the wavefront quality of the two beams and on the accuracy of overlap at the beam combiner[3]. Factors influencing the system visibility include alignment, aberrations in the instrument optics, tracking (tip-tilt) errors, and higher-order wavefront errors due to atmospheric seeing. Using tip-tilt corrected $3r_0$ apertures we expect a mean Strehl ratio of $\geq 43\%$ from each telescope (Noll 1976; Fusco & Conan 2004), providing a system visibility of order 0.40.

The total difference in sensitivity between FLAMES and the UVES-I combination depends on the instrument efficiency and the source visibility. The efficiency due to both the throughput and the system visibility would be equivalent to a loss of 10.8 magnitudes (Tab. 2.1) in both the stellar and sky background photon counts. After an integration of 2 min using the maximum spectral resolution and fast read-out rate of UVES-I, one would be in the photon-noise-limited regime for a G0 star of magnitude $R = 6$. In this regime long integrations can be constructed from multiple short exposures with no additional noise penalty in order to reach the required SNR. The signal-to-noise also varies in proportion to the source visibility. It should be pointed out that even though the sensitivity of UVES-I is significantly lower than that of UVES, the

[3]We do not consider the possibility of increasing the system visibility with a spatial filter here, because the introduction of such a filter would impose much more stringent requirements on the alignment and might reduce the fringe temporal stability (Tubbs 2005).

Table 2.1 — Comparison of UVES-I throughput with the throughput of UVES-FLAMES, for operation without adaptive optics (0.75 m aperture) and with adaptive optics (full 1.8 m aperture of the ATs).

Term	Flux reduction ($\frac{\text{UVES}-\text{I}}{\text{FLAMES}}$)
Telescope aperture area (no AO / with AO)	0.009 / 0.05
Number of telescopes	2
Transmission VLTI / UT	0.075
Beam combiner transmission	0.72
Fiber link UVES-I / FLAMES	0.75
Flux for real and imaginary components of visibility	0.5
Squared system visibility	0.16
Squared fringe tracking losses	0.85
Total (no AO / with AO)	4.9×10^{-5} / 2.8×10^{-4} 10.8mag / 8.9mag

final sensitivity compares quite favorably with other optical interferometers especially bearing in mind that the achieved spectral resolution is very high. The signal-to-noise ratio will be further reduced in proportion to the source visibility, but for many measurements described in Section 2.2 the sources need only be marginally resolved, so that the variation of visibility phase with wavelength directly probes offsets in the position of the emitting region.

For example, for a measurement of the phase change across a spectral line the adjacent continuum provides an excellent calibration, allowing measurement of phase changes with wavelength as small as one milliradian. This means that UVES-I will be sensitive to astrometric offsets that are over one hundred times smaller than the resolution limit of the interferometer. It will not be possible to image such small structures, but models of such astrometric offsets can be constructed and tested with UVES-I.

It should be pointed out that not all observing programs will require the full spectral resolution provided by the new instrument. In those cases it will be possible to obtain a higher SNR per desired spectral element by binning the data. In the readout-noise-limited regime, this can best be done on the CCD. This would have the advantage that one would be able to go to fainter targets than stated above with shorter integration times and shorter detector readout times.

Often the astrophysical interesting signal is encoded in multiple lines in a spectral region (Section 2.2). In this case the SNR can be improved by cross-correlating these absorption lines with a line-template mask. This is routinely done in high-resolution spectroscopy, (e.g. Griffin 1967; Queloz 1995; Donati et al. 1997; Rucinski 1999) but has not yet been done with optical interferometers, while it would be possible with an instrument like UVES-I.

2.5 Other interferometer-spectrograph pairings

In this section we give some remarks about other possible pairings of interferometers and spectrographs at different sites and in different wavelength regimes.

The high-resolution spectrograph CRIRES at Paranal Observatory covers the wavelength range from 1 μm to 5 μm and has a spectral resolution up to $R_{CRIRES} \sim 10^5$ (Kaeufl et al. 2004). The wavelength range would overlap with the wavelength range of AMBER (Petrov et al. 2003) but with a much higher resolution ($R_{AMBER} \sim 12000$). The throughput of the VLTI+CRIRES combination would be higher than UVES-I as the transmission of the VLTI increases towards longer wavelengths. The distortions of the incoming wavefronts are also less severe for the longer wavelengths (see Section 2.3.1), so one would be able to use the full aperture of the ATs or make observations with the UTs using the MACAO AO system (Arsenault et al. 2004). For a combination of CRIRES with the VLTI one could use the Optran Plus WF fiber (Figure 2.5) as the transmission for a 150 m of Optran Plus WF fiber between 1 μm and 2 μm would be $\sim$ 80 %. Note the dip at $\sim$ 2 μm and the steep decline in transmission beyond 2 μm.

In the Northern hemisphere the Mauna Kea Observatory site would be well-suited for the high spectral resolution optical/IR interferometer design advocated in this chapter. The Keck interferometer (KI) is already in place at the observatory and its infrastructure is similar to the one found at the VLTI (delay lines, 2-μm fringe tracker). The HIRES spectrograph with the spectral range from 0.3 μm to 1.1 μm and a resolving power of $R \sim 67000$ (Vogt et al. 1994) at the Keck I Telescope covers a similar wavelength-range to the UVES spectrograph. Therefore a similar approach as described in Section 2.4 is possible for mating HIRES and KI. The combination of a high-resolution spectrograph with an interferometer at this site seems particular attractive from the scientific point of view, as so far the interferometer has no spectrographic mode.

A second interferometer, the OHANA experiment, is also currently being set up at Mauna Kea (Perrin et al. 2004). This instrument uses optical fibers for beam transport instead of the bulk optics used in conventional interferometers. This allows combination of telescopes which were not originally designed for interferometry, forming an array several hundred meters across. Using the OHANA array, one would potentially have access to all spectrographs at the telescopes which are connected to OHANA. However one has to use the bandwidth offered by the OHANA fibers (J,H,K). One would prefer to keep the length of the transport of the beams after the combination in the interferometric lab short to avoid unnecessary losses, therefore one could use the spectrographs at the telescope where the beam combiner is placed. A new beam combiner at CFHT will be used by the OHANA project in addition to the existing K-band fringe tracker on the Keck Interferometer. The Near Infrared Echelle Spectrograph (NIRSPEC) at the Keck II could be used as the spectrograph.

2.6 Conclusion

This article shows that the combination of high-resolution spectroscopy with long-baseline interferometry gives access to hitherto unobservable properties of stellar surfaces and circumstellar matter.

Furthermore the article shows how this combination can be achieved without building a major new instrument; only a beam combiner and a fiber link are needed. No instrument components are required which would be expensive or time-consuming to make. The use of external fringe tracking is essential for an instrument like this as it enables long integration times. Time-varying longitudinal dispersion could severely limit the possibilities of such an

instrument. Dispersion compensation techniques are investigated in this article and a solution is presented which allows integration times up to a few minutes.

The implementation of this approach is shown for the example combination UVES-VLTI. The resulting instrument would differ from other instruments or efforts taken to achieve high spatial and spectral resolution. It would offer spectral resolution nearly a factor 2 higher than for any other interferometric instrument, and over a wide spectral range of a few hundred rather than a few tens of nanometers. It offers the same possibilities to an astronomer as a high-resolution Echelle spectrograph behind a single telescope does, plus the high spatial resolution due to the interferometer, albeit only for bright targets. However it is important to realize that this concept, the combination of two existing instruments to create a new one, is not limited to a specific location or instrument, but rather is an approach which can be followed at different observatories in both hemispheres.

It is worth pointing out that the measurements taken with the proposed instruments are differential in nature (e.g. change of visibility amplitude and visibility phase over spectral lines), allowing many interferometric calibration problems to be circumvented. As noted in Section 2.2, these differential measurements contain a wealth of astronomical information in the optical/IR regime.

Acknowledgments

We are thankful to Jeff Meisner, Luca Pasquini, and Gerardo Avila for many useful discussions and suggestions. We are grateful to Richard J. Mathar for providing material on the refractivity of water vapor.

Bibliography

Albrecht, S., Bakker, E. J., de Jong, J. A., et al. 2004, in Proc. SPIE, ed. W. A. Traub, Vol. 5491, 1266 21, 26

Arsenault, R., Donaldson, R., Dupuy, C., et al. 2004, in Proc. SPIE, ed. D. Bonaccini Calia, B. L. Ellerbroek, & R. Ragazzoni, Vol. 5490, 47 32

Berger, D. H., ten Brummelaar, T. A., Bagnuolo, Jr., W. G., & McAlister, H. A. 2003, in Proc. SPIE, ed. W. A. Traub, Vol. 4838, 974 27

Buscher, D. F., Armstrong, J. T., Hummel, C. A., et al. 1995, Appl. Opt., 34, 1081 24

Chelli, A. & Petrov, R. G. 1995, A&AS, 109, 401 15

Ciddor, P. E. 1996, Appl. Opt., 35, 1566 26

Colavita, M. M., Wizinowich, P. L., & Akeson, R. L. 2004, in Proc. SPIE, ed. W. A. Traub, Vol. 5491, 454 21

Cunha, M. S., Aerts, C., Christensen-Dalsgaard, J., et al. 2007, A&A Rev., 14, 217 15

Dekker, H., D'Odorico, S., Kaufer, A., Delabre, B., & Kotzlowski, H. 2000, in Proc. SPIE, ed. M. Iye & A. F. Moorwood, Vol. 4008, 534 30

Delplancke, F. 2003, PRIMA, the Phase Referenced Imaging and Microarcsecond Astrometry facility: High Level Requirements & System Description, ESO Doc. ref.: VLT-SPE-ESO-15700-3051 21, 27

Domiciano de Souza, A., Zorec, J., Jankov, S., et al. 2004, A&A, 418, 781 15, 16

Donati, J.-F., Semel, M., Carter, B. D., Rees, D. E., & Collier Cameron, A. 1997, MNRAS, 291, 658 31
Fried, D. L. 1966, Optical Society of America Journal, 56, 1372 17
Frink, S., Mitchell, D. S., Quirrenbach, A., et al. 2002, ApJ, 576, 478 15
Fusco, T. & Conan, J.-M. 2004, Journal of the Optical Society of America A, 21, 1277 30
Goodman, J. W. 1985, Statistical Optics, Chapter 8 (Wiley) 24
Gray, D. F. 1977, ApJ, 211, 198 16
Griffin, R. F. 1967, ApJ, 148, 465 31
Jankov, S., Vakili, F., Domiciano de Souza, Jr., A., & Janot-Pacheco, E. 2002, in ASP Conference Series, Vol. 259, IAU Colloq. 185: Radial and Nonradial Pulsationsn as Probes of Stellar Physics, ed. C. Aerts, T. R. Bedding, & J. Christensen-Dalsgaard, 172 14
Kaeufl, H.-U., Ballester, P., Biereichel, P., et al. 2004, in Proc. SPIE, ed. A. F. M. Moorwood & M. Iye, Vol. 5492, 1218 32
Kochukhov, O., Drake, N. A., Piskunov, N., & de la Reza, R. 2004, A&A, 424, 935 14
Kolmogorov, A. 1941, Akademiia Nauk SSSR Doklady, 30, 301 17
Labeyrie, A. 1975, ApJ, 196, L71 22
Lin, D. N. C. & Ida, S. 1997, ApJ, 477, 781 16
Lucke, R. L. & Young, C. Y. 2007, Appl. Opt., 46, 559 24
Marengo, M., Sasselov, D. D., Karovska, M., Papaliolios, C., & Armstrong, J. T. 2002, ApJ, 567, 1131 15
Martin, F., Conan, R., Tokovinin, A., et al. 2000, A&AS, 144, 39 25
Mathar, R. J. 2004, Appl. Opt., 43, 928 26
McAlister, H. A., Ten Brummelaar, T. A., Aufdenberg, J. P., et al. 2004, in Proc. SPIE, ed. W. A. Traub, Vol. 5491, 472 21
Meilland, A., Stee, P., Vannier, M., et al. 2007, A&A, 464, 59 16
Meisner, J. A. 2007, Using the FSU to generate a phase reference for coherent integration by MIDI at N band, Unpublished 25, 26
Monnier, J. D. 2003, Reports of Progress in Physics, 66, 789 17
Nagasawa, M., Ida, S., & Bessho, T. 2008, ApJ, 678, 498 16
Nardetto, N., Mourard, D., Mathias, P., & Fokin, A. 2006, Memorie della Societa Astronomica Italiana, 77, 235 15
Noll, R. J. 1976, Optical Society of America Journal, 66, 207 30
Papaloizou, J. C. B. & Terquem, C. 2001, MNRAS, 325, 221 16
Pasquini, L., Avila, G., Allaert, E., et al. 2000, in Proc. SPIE, ed. M. Iye & A. F. Moorwood, Vol. 4008, 129 29
Perrin, G. S., Lai, O., Woillez, J. M., et al. 2004, in Proc. SPIE, ed. W. A. Traub, Vol. 5491, 391 32
Petrov, R. G. 1989, in NATO ASIC Proc. 274: Diffraction-Limited Imaging with Very Large Telescopes, ed. D. M. Alloin & J.-M. Mariotti, 249 15
Petrov, R. G., Malbet, F., Weigelt, G., et al. 2003, in Proc. SPIE, ed. W. A. Traub, Vol. 4838, 924 32
Puech, F. & Gitton, P. 2006, Interface Control Document between VLTI and its Instruments, ESO Doc. ref.: VLT-ICD-ESO-15000-1826 24
Queloz, D. 1995, in IAU Symposium, Vol. 167, New Developments in Array Technology and Applications, ed. A. G. D. Philip, B. Hauck, & A. R. Upgren, 221 31

Quirrenbach, A. 2001, ARA&A, 39, 353 14, 21
Quirrenbach, A. & Aufdenberg, J. 2003, in IAU Symposium, Vol. 210, Modelling of Stellar Atmospheres, ed. N. Piskunov, W. W. Weiss, & D. F. Gray, 68P 13
Quirrenbach, A., Bjorkman, K. S., Bjorkman, J. E., et al. 1997, ApJ, 479, 477 16
Quirrenbach, A., Mozurkewich, D., Armstrong, J. T., Buscher, D. F., & Hummel, C. A. 1993, ApJ, 406, 215 13
Rice, J. B. 2002, Astronomische Nachrichten, 323, 220 14
Roddier, F. 1981, Prog. Optics, 19, 281 17
Rucinski, S. 1999, in ASP Conference Series, Vol. 185, IAU Colloq. 170: Precise Stellar Radial Velocities, ed. J. B. Hearnshaw & C. D. Scarfe, 82 31
Sabbey, C. N., Sasselov, D. D., Fieldus, M. S., et al. 1995, ApJ, 446, 250 15
Shao, M., Colavita, M. M., Hines, B. E., Staelin, D. H., & Hutter, D. J. 1988, A&A, 193, 357 22
Shulyak, D., Tsymbal, V., Ryabchikova, T., Stütz, C., & Weiss, W. W. 2004, A&A, 428, 993 14
Tatarski, V. I. 1961, Wave Propagation in a Turbulent Medium (McGraw-Hill) 17
Taylor, G. I. 1938, in Proceedings of the Royal Society of London A, 164, 476 24
Tsuji, T. 2006, ApJ, 645, 1448 14
Tubbs, R. 2005, Appl. Opt., 44, 6253 30
Tubbs, R. N., Launhardt, R., Meisner, R., & Mathar, R. 2007, ESPRI Exoplanets Search with PRIma: Astrometric Error Budget, ESO Doc. ref.: VLT-TRE-AOS-15753-0001, V2.1 27, 28
Tuthill, P. G., Haniff, C. A., & Baldwin, J. E. 1999, MNRAS, 306, 353 14
Tycner, C., Gilbreath, G. C., Zavala, R. T., et al. 2006, AJ, 131, 2710 16
Vakili, F., Mourard, D., Stee, P., et al. 1998, A&A, 335, 261 12
Vogt, S. S., Allen, S. L., Bigelow, B. C., et al. 1994, in Proc. SPIE, ed. D. L. Crawford & E. R. Craine, Vol. 2198, 362 32
Weigelt, G., Kraus, S., Driebe, T., et al. 2007, A&A, 464, 87 12
Wittkowski, M., Aufdenberg, J. P., Driebe, T., et al. 2006, A&A, 460, 855 14
Wu, Y. & Murray, N. 2003, ApJ, 589, 605 16
Young, J. S., Baldwin, J. E., Basden, A. G., et al. 2003, in Proc. SPIE, ed. W. A. Traub, Vol. 4838, 369 14, 16

Chapter 3

MWC 349A

In this chapter we aim to understand the massive young stellar object MWC 349A better, by studying the structure of its disk, the structure of the region from where the hydrogen emission lines originate and the forbidden lines at high spatial resolution in the N-band.

Previous observations of this peculiar emission line star suggest that it is a young massive star in the short-lived phase during which it has already dissipated its parent cloud, but it is still surrounded by the accretion disk which is seen nearly edge-on. It is believed that the unique hydrogen recombination line maser/laser activity of MWC 349A from mm to infrared wavelengths is also a consequence of this viewing angle. However, despite a wealth of data already available, it has so far not been possible to assign a clear evolutionary status to MWC 349A.

We have used the unique capabilities of the Very Large Telescope Interferometer (VLTI) in combination with the Mid-Infrared Interferometric Instrument (MIDI) to observe MWC 349A and spatially resolve the inner parts of its disk. We observed MWC 349A with MIDI at the peak of its spectral energy distribution, from 8 to 13 μm, with a spectral resolution of R $\sim$ 230. We obtained 19 *u,v* points with different baseline lengths and at different position angles.

The observed wavelength-dependence of the continuum visibility amplitudes agrees with model calculations for a hot inner disk and a wider colder disk both seen edge on. We model the visibility amplitudes and the SED in the spectral wavelength range of MIDI with optically thin emission from warm silicate, and a shield of colder material. This is critical to obtain a good agreement between model and data. In addition the signatures of at least a dozen emission lines have been identified in the interferometric data. We extract the visibilities of these lines, and model the spatial distribution of the emitting regions successfully using two emission regions separated by a few tens of mas consistent with observations of hydrogen masers at radio wavelengths.

S. Albrecht, R. N. Tubbs, A. Quirrenbach & I.A.G. Snellen
A&A in preparation

3.1 Introduction MWC 349A

Although in the optical MWC 349A is a rather inconspicuous early-type emission line star, it is very bright throughout the infrared, and it is one of the most luminous radio stars known to date (Altenhoff et al. 1994; Baldwin et al. 1973). Its bolometric luminosity is at least $2{\cdot}10^4\,L_\odot$, if corrected for foreground extinction, but probably much higher if much of the absorbing material is in a disk allowing most of the stellar radiation to escape. A luminosity as high as $5 \cdot 10^5\,L_\odot$ appears plausible if a bolometric correction corresponding to a hot main sequence star is applied. Recent spectropolarimetric observations have strengthened the classification of MWC 349A as a pre-main sequence B[e] star (Meyer et al. 2002). Furthermore, direct evidence for a circumstellar disk was obtained from high-resolution VLA images (White & Becker 1985; Martín-Pintado et al. 1993; Tafoya et al. 2004) and from near-infrared spectroscopy (Hamann & Simon 1986). The hydrogen recombination line maser detected in this source by Martin-Pintado et al. (1989) is expected to originate from this disk (Planesas et al. 1992; Thum et al. 1992). The latter authors suggest, on the basis of a series of maser transitions at 1 and 2 mm wavelength, that the disk is in Keplerian rotation around a central mass of $30\,M_\odot$, which would indicate that the central star is of spectra type O6-O8, if it is not a close binary.

The remarkable stability of the double-peaked maser features (Thum et al. 1992; Gordon 1992; Thum et al. 1994a,b) and the evidence for Keplerian rotation prompted Thum & Martin-Pintado (1994) to propose that MWC 349A is a young massive star, near the zero-age main sequence, still surrounded by its accretion disk. In this picture, we observe MWC 349A in the (probably short) period of a massive star's life, during which the parental cloud is already completely dispersed, but the star has not yet fully destroyed its accretion disk by ionization. Indeed, the spectral energy distribution (SED) shows no trace of significant cold dust emission. This is unlike the SED of compact H II regions which invariably peak near $70\,\mu$m, owing to the presence of a large mass of cold dust in the parental cloud. The extremely uniform slope of the SED out to the longest radio wavelengths is also evidence for a constant-velocity ionized wind which expands isotropically into the surrounding volume, which it appears to have cleared out to at least 0.1 pc. The extinction towards the central emission-line source is comparatively small ($A_V \sim 10$ mag), indicating that MWC 349A has left its parent molecular cloud, enabling studies of this object in the far red and infrared. Emission-line spectra in this wavelength regime have been successfully interpreted by a photo-evaporating disk model (Hamann & Simon 1986). While the outer regions of the disk consist of cold, dense neutral gas, the inner few AU are photo-ionized by the UV flux from the central star. A host of fine-structure lines from ions with ionization potentials of up to 41 eV are detected in the Infrared Space Observatory (ISO) spectrum of MWC 349A, confirming that the effective temperature of the star is at least 35,000 K (Quirrenbach et al. 2001). Hydrogen and He I recombination lines seem to be generated in a wind emanating from the disk surface rather than from the stellar photosphere, indicating substantial illumination of the disk by scattered UV radiation. The H II region generated in this way should be fairly long-lived (about $3{\cdot}10^5$ years), because it is constantly replenished from the disk, which provides an abundant reservoir of dense gas. The strong radio continuum emission originates in a massive ionized wind ($1.2{\cdot}10^{-5}\,M_\odot\,\mathrm{yr}^{-1}$). Its low expansion velocity of 50 km s^{-1} testifies to its origin on the circumstellar disk (not the stellar photosphere). MWC 349A is therefore considered as the prime example of a photo-evaporating disk around a massive star.

The most spectacular features of the MWC 349A disk are the strong hydrogen recombina-

tion line masers at mm and sub-mm wavelengths (H21α to H35α), which are thought to be located in the disk at 40 AU distance (Martin-Pintado et al. 1989; Thum et al. 1994b). In the mid-1990s MWC 349A was observed with the Short Wavelength Spectrograph (SWS) and Long Wavelength Spectrograph (LWS) grating spectrometers on the ISO satellite (Thum et al. 1998; Quirrenbach et al. 2001). Among the about 100 detected hydrogen recombination lines are all 12 transitions within the wavelength range accessible to ISO, from Brα at 4.05 μm to H15α at 169.4 μm. The lines with n < 6 are optically thick; the lines with higher n are amplified, and thus constitute infrared lasers. Combining the ISO results with millimeter and sub-millimeter data gives the first global view of the recombination line laser/maser phenomenon in this star. The maximum line-integrated amplification, of a factor of 30, occurs in the region near n = 19 at 300 μm.

Complementary information on the MWC 349A disk comes from recent high spatial resolution observations in the near-infrared using aperture masking at the Keck I Telescope (Danchi et al. 2001), and speckle interferometry at the SAO 6 m Telescope (Hofmann et al. 2002). These data sets reveal a disk seen almost edge-on at a position angle of $100^\circ \pm 3^\circ$ on the sky, consistent with the position angle of a dark lane observed previously in the VLA continuum maps. It therefore appears that the uniqueness of MWC 349A (the only known hydrogen recombination line maser source known to date) is a consequence of its being in a short-lived evolutionary stage, combined with an almost edge-on orientation.

Observing MWC 349A with MIDI and the VLTI we want to investigate the structure of the inner circumstellar disk. Taking advantage of the spectral resolution of MIDI in the N band we further want to investigate the mineralogy of the disk and the hydrogen emission lines visible in the N band.

3.2 MIDI Observations

We observed MWC 349A with the MIDI instrument of the VLTI (Leinert et al. 2003). We obtained five (u, v) data points on the 47 m long baseline between the Unit Telescopes UT2 and UT3 during the first half-night of May 26 2005, and six (u, v) data points on the 102 m UT1-UT3 baseline during the second half-night of May 27 2008. Unfortunately, four of these observations were affected by rather thick cirrus, and cannot be used. All these observations were obtained in High_Sens mode, meaning that no simultaneous photometric measurement of beams before combination is done, i.e. measurements of the correlated and uncorrelated flux are carried out sequentially. This requires that the transfer function of Earth's atmosphere does not change significantly between the two observations. Unfortunately, this condition was not met for the observations affected by cirrus clouds. Two additional (u, v) data points were obtained on the baselines UT2-UT4 (89 m length) and UT3- UT4 (62 m). These two baselines provide data at a somewhat different position angle. These observations were also obtained in MIDI's High_-Sens mode, and like the former observations they also employed the GRISM, which provides spectrally resolved data R $(\lambda/\Delta\lambda) \sim 230$ from 8 μm to 13 μm. These observations provide information on small spatial scale structures in MWC 349A (down to a few mas).

To further complement these observations and to obtain information on larger scales, we also observed with shorter baselines using the Auxiliary telescopes (ATs), as these can be positioned closer to each other than the UT's. Three (u, v) points were obtained with a 16 m baseline and

Table 3.1 — Log of MIDI observations of MWC 349A.

Date	Baseline	number (u,v) points	Dispersive element	Mode
26-05-2005	UT2 - UT3	5	GRISM	High_Sens
27-05-2005	UT1 - UT3	6	GRISM	High_Sens
20-07-2005	UT3 - UT4	1	GRISM	High_Sens
24-08-2005	UT2 - UT4	1	GRISM	High_Sens
26-05-2006	E0 - G0	2	PRISM	Sci_Phot
18-06-2006	E0 - G0	2	PRISM	Sci_Phot
16-06-2006	G0 - H0	3	PRISM	Sci_Phot

NOTES – See http://www.eso.org/sci/facilities/paranal/telescopes/vlti/configuration/index.html for the positions of the different telescopes / AT stations at Paranal observatory.

three observations with a 32 m baseline, all again with slightly varying position angles. These six observations were obtained in Sci_Phot mode of MIDI using the PRISM as the dispersive element, giving a modest spectral resolution of $R \sim 30$. In the Sci_Phot mode the correlated and uncorrelated flux are obtained simultaneously at different locations on the detector. The (u,v) plane coverage of the MIDI observations is shown in Figure 3.1. All observations are listed in Table 3.1.

For the reduction of all MIDI data the software package MIA+EWS 1.5.2[1] was used. The quantities measured by MIDI are the visibility amplitude and the visibility phase. The visibility amplitude delivered by MIDI is the uncalibrated *instrumental* visibility amplitude. As the transfer function of MIDI delivers a visibility amplitude for a point source which is $\lesssim 1$, and the transfer function might change over time, each measurement of MWC 349A is accompanied by a calibrator observation, either directly before or after the observation of the science target. To derive the calibrated visibility amplitudes, the observed amplitude is divided by the visibility amplitude of the calibrator star (assumed to be unresolved). A second assumption, which is implicitly made for these observations, is that the transfer function of the Earth's atmosphere does not change over the time span between the observations of the calibrator and science target. In addition, it is also assumed that the Earth's atmosphere has the same transfer function towards the different stars being observed in different parts of the sky. For MIDI it is often the case that the angle between calibrator and the science object is considerable (see the positions of the calibrator stars and science objects in Table A.1). It turns out that the error terms induced by these assumptions constitute the largest error sources in the visibility amplitudes (MWC 349A is very bright in the N band which reduces the importance of other error sources). We therefore collected all calibrator observations made during the nights on which MWC 349A was observed, from the ESO archive, and compared the scatter in their visibility amplitudes to assess the uncertainty in the overall visibility amplitudes derived of MWC 349A. All visibility amplitudes

[1] http://www.strw.leidenuniv.nl/∼nevec/MIDI/index.html

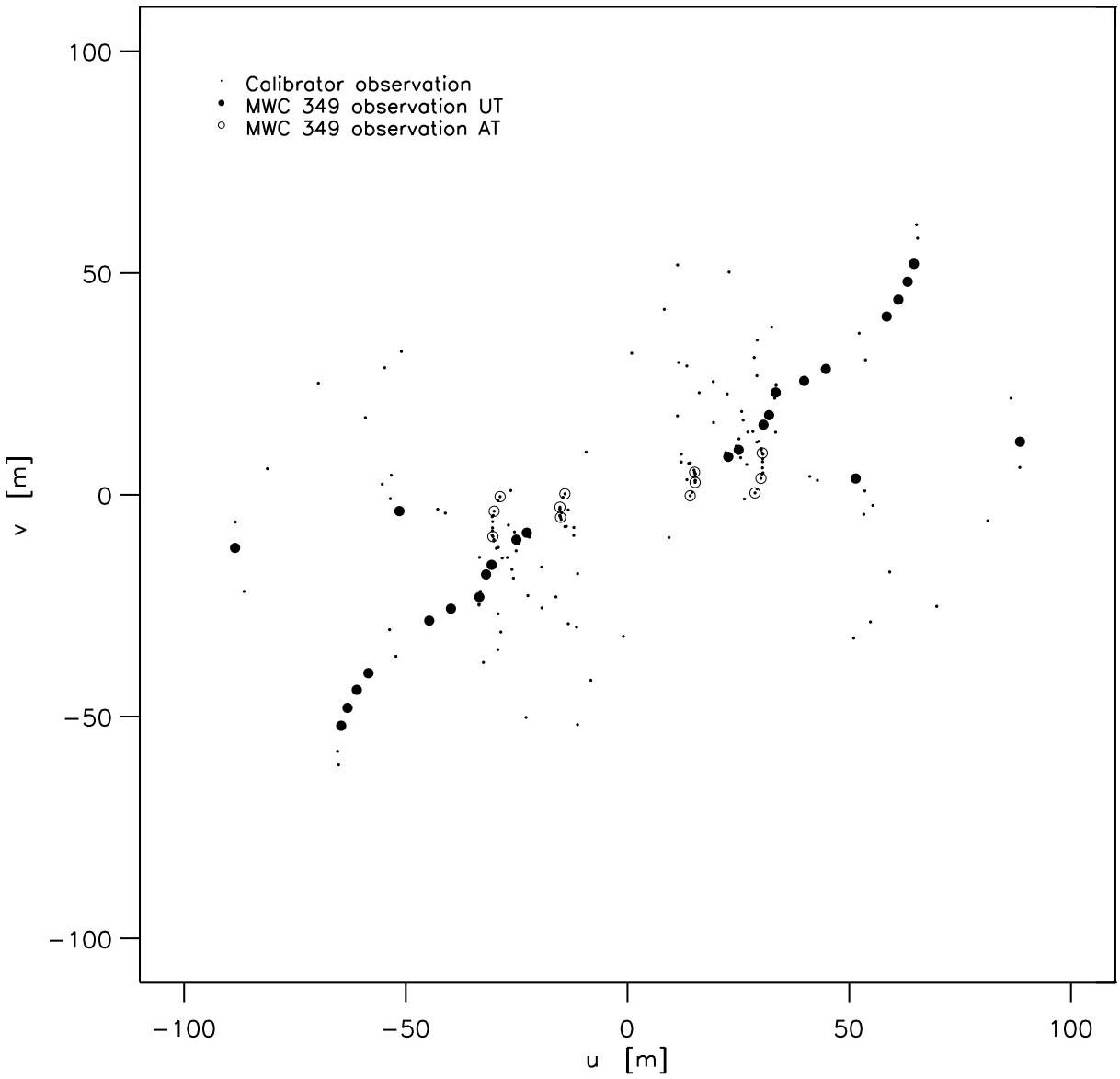

Figure 3.1 — The Fourier (*uv* plane) coverage of the MIDI observations. The filled circles indicate the *uv* position of the MWC 349A observations made with UTs. The open circles indicate the observations using the ATs. The small dots show all the calibrator observations done during the observation nights. Note that most observations are along one position angle in the *uv* plane. This is due to the high northern declination of the object and the resulting low elevation at which it is seen from Paranal. This means that MWC 349A is only observable for a short period each night and is always at about the same hour angle with a similar orientation of the UT1-UT3 and UT2-UT3 baselines.

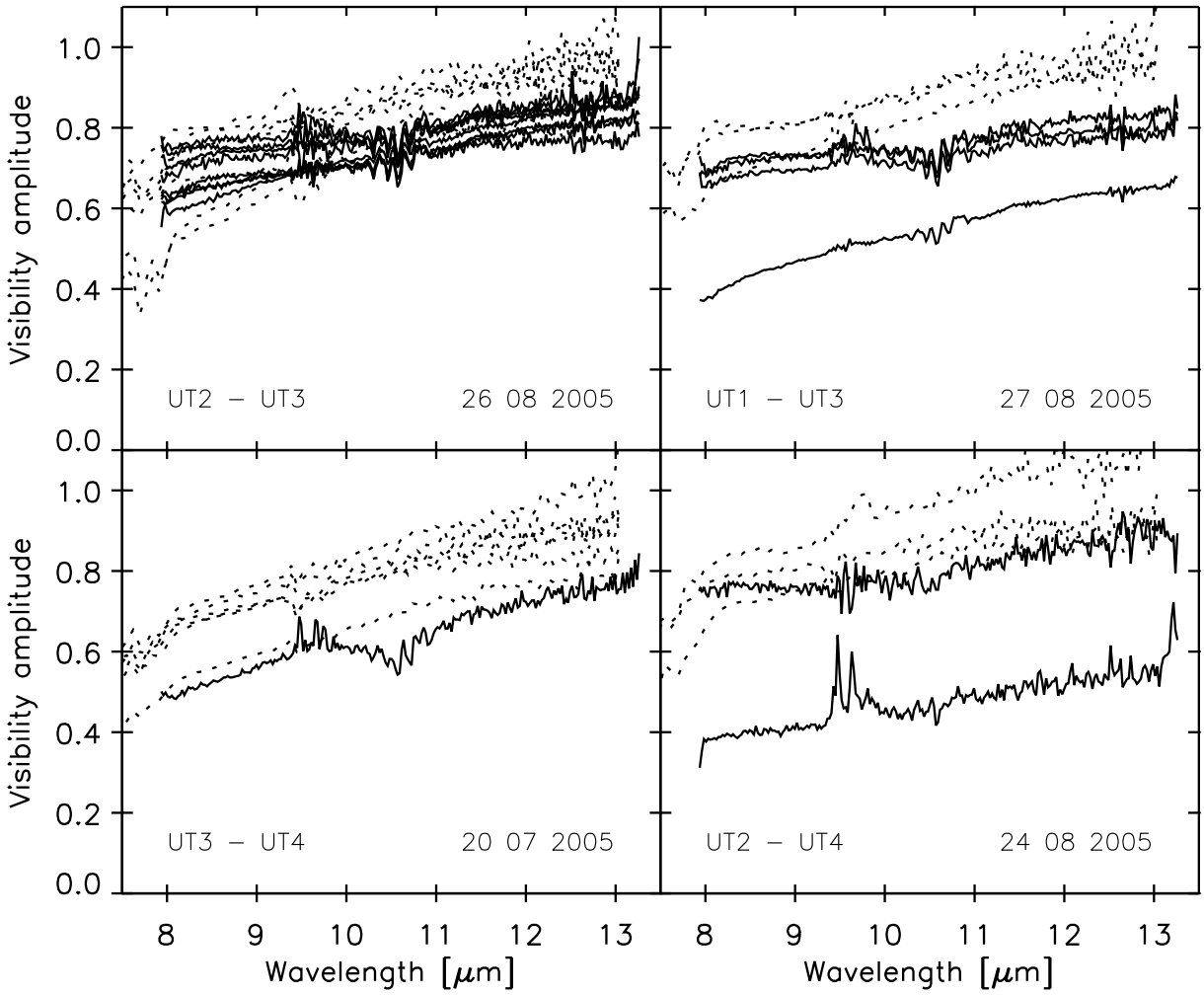

Figure 3.2 — The four panels show the visibility amplitudes of all calibrators observed using MIDI on four nights during which MWC 349A was also observed. The observing dates and baselines are indicated in the bottom right and left corners of each panel, respectively. The solid lines represent observations obtained in High_Sens mode using the GRISM as dispersive element. The dotted lines indicate High_-Sens PRISM observations.

of the calibrators can been seen in Figures 3.2 and 3.3. Note that 13 Lyr, one of the calibrators on the night 27.08.2005, is already partly resolved. The visibility amplitudes for the calibrator (γ Cyg) obtained in High_Sens mode during the night 24.08.2005 changes strongly between the two observations, which is probably due to changing atmospheric conditions. One can see in these figures that the transfer function of the instrument and the atmosphere is stable during most nights on a $\sim$ 10% level, while small systematic differences exists between the different instrumental setups. Note that the uncertainties derived in this way are for the overall visibility amplitude. The relative precision and accuracy of the visibility amplitudes at the different wavelengths is much higher. One example instrumental visibility amplitude of MWC 349A is displayed in Figure 3.4.

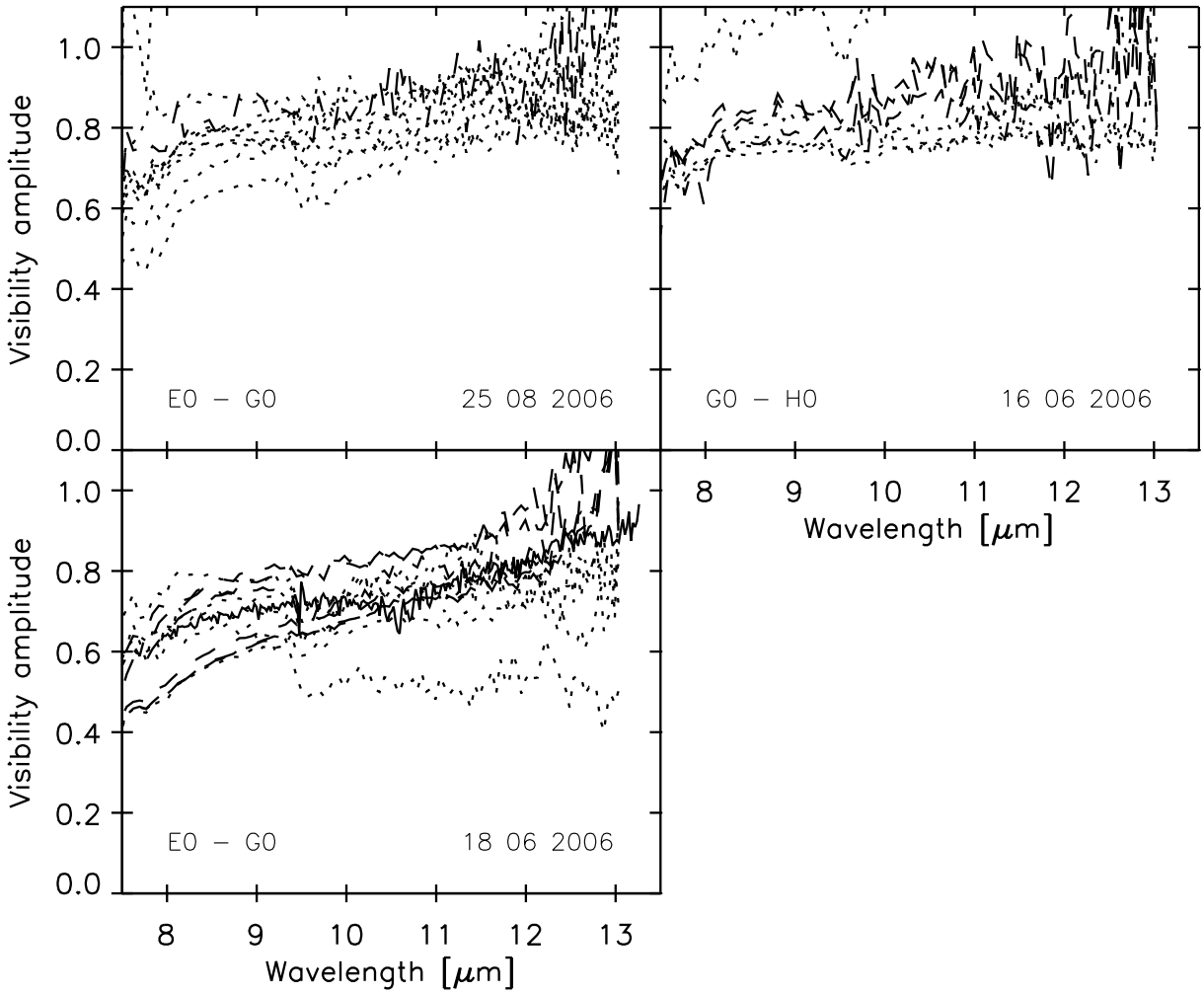

Figure 3.3 — The same as Figure 3.2 but for the three other nights. Sci_Phot PRISM observations of calibrators were also carried out on these nights, as shown by the dashed lines

The visibility phase is the second important quantity obtained from the MIDI measurements. The phase of the interferometric fringes contains information on the position of the emission well below the resolution limit (observing wavelength / projected baseline length) of the interferometer. To exploit this information an absolute phase reference is needed, which does not exist for the case of MIDI observations as the atmosphere corrupts the phase signal. The color-differential phase can however deliver information on the relative position of the centroid emission at the different wavelengths. The greater the difference between the wavelengths the larger the influence of the atmosphere, which makes the interpretation of the differential phase over the complete MIDI pass-band difficult. Fortunately, for measurements of rapid phase changes with wavelength the phase in the adjacent wavelength channels constitutes an excellent calibration source. See Figure 3.5 for an example differential phase as a function of wavelength for one (u, v) point. One can clearly see a change in phase at the wavelength of the forbidden [Ne II]

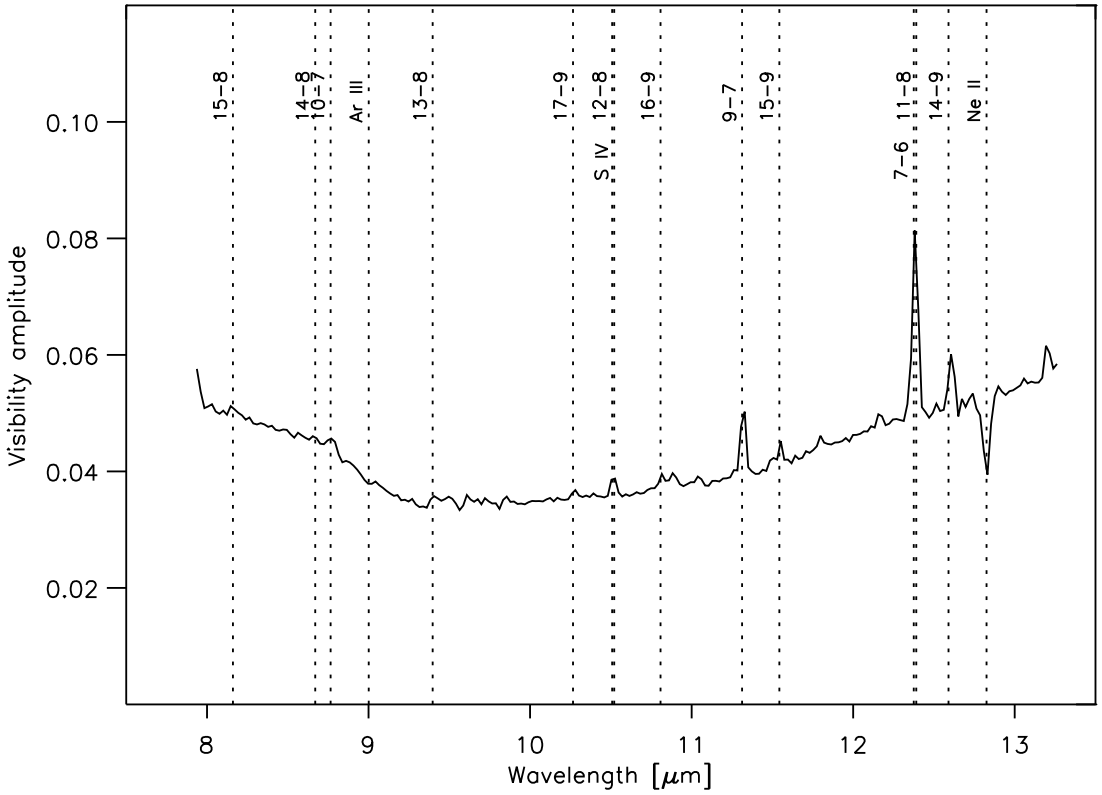

Figure 3.4 — Example of an instrumental visibility amplitude obtained with MIDI, for MWC 349A for a projected baseline of 48 m and a position angle of 33°. The observations were carried out in High_Sens GRISM mode ($R\sim$ 230 over the MIDI band-pass from 8 μm – 13 μm). The wavelengths of all hydrogen recombination lines in the MIDI passband and the forbidden lines are indicated.

line and the stronger hydrogen recombination lines. Note that one degree of phase corresponds to 1/360 th of the interferometer resolution, i.e., we are sensitive to displacements as small as 100 μas, which corresponds to 0.1 AU.

3.3 Results

3.3.1 The circumstellar disk

The visibility amplitudes for MWC 349A show a characteristic shape for all baselines (see Figures 3.6, 3.7, and 3.8). It is in general rather high at short wavelengths, drops to a minimum around 10 μm, and increases again towards the long-wavelength end of the spectrometer range.

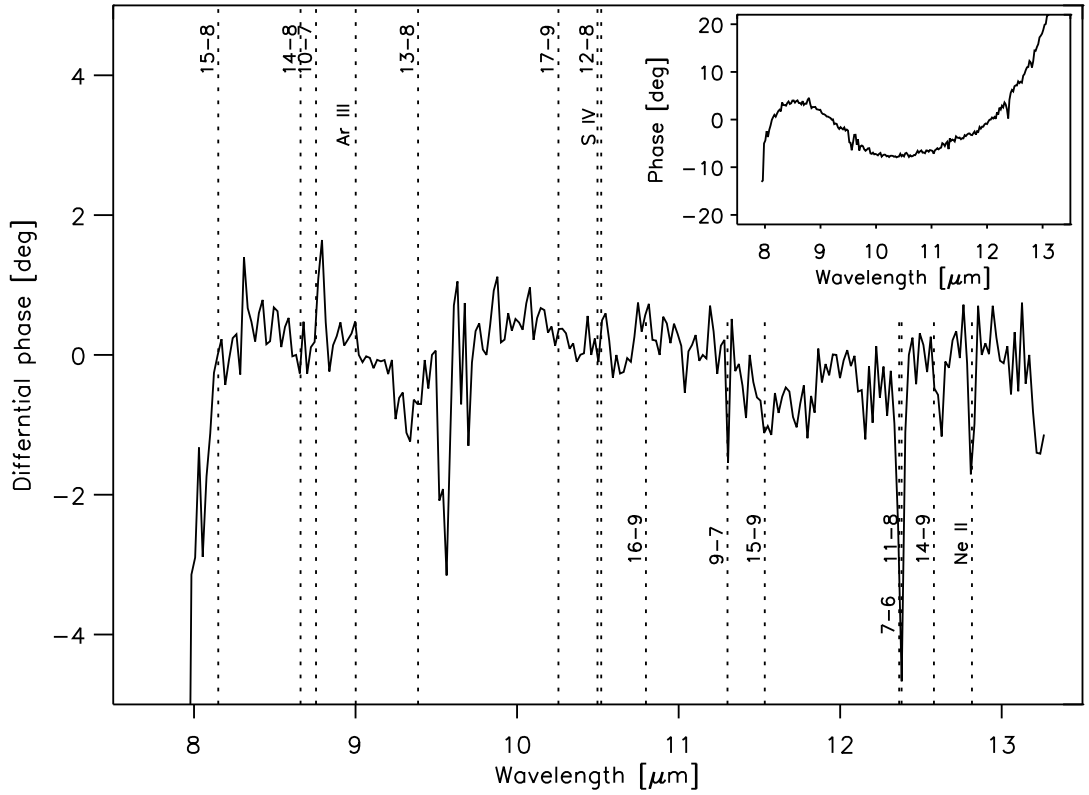

Figure 3.5 — The differential visibility phase as a function of wavelength for the same observations as shown in Figure 3.4. A high-pass filter was applied to the visibility phase to reject distortion due to dispersion in the air-filled light ducts in the interferometer, this will however also destroy all low frequency phase information on MWC 349A which might be present. The original phase can be seen in the insert. Note that as no absolute phase is defined, there is an arbitrary offset. The phases are unreliable in the 9.4 μm–9.9 μm region due to the influence of ozone in the Earth's atmosphere.

Visibilities with a somewhat similar wavelength dependence have been observed in a number of Herbig Ae/Be stars (e.g. Leinert et al. 2004). They are characteristic for disks, in which a warmer and smaller component dominates the shorter wavelengths within the N band, whose flux drops towards longer wavelengths, and a cooler, larger component whose contribution to the visibility becomes more important at longer wavelengths. The rise in visibility amplitude at long wavelengths is partly due to the reduced spatial resolution of the interferometer towards long wavelengths. The decrease in resolution of the interferometer with increasing observing wavelength might however not be the only reason for a rise in visibility amplitude at longer wavelengths. Mineralogy of the dust which constitutes the disk might play a role as well as geometric effects. The mass absorption coefficient (κ_ν) of amorphous silicate, which is thought to be abundant in proto-planetary disks, rises from the short wavelength side of the band-pass of MIDI, peaks at $\sim 9.7\,\mu$m, and subsequently decreases again (see Figure 3.9). That means one actually probes *colder* layers closer to the mid-plane of the circumstellar disk at the long

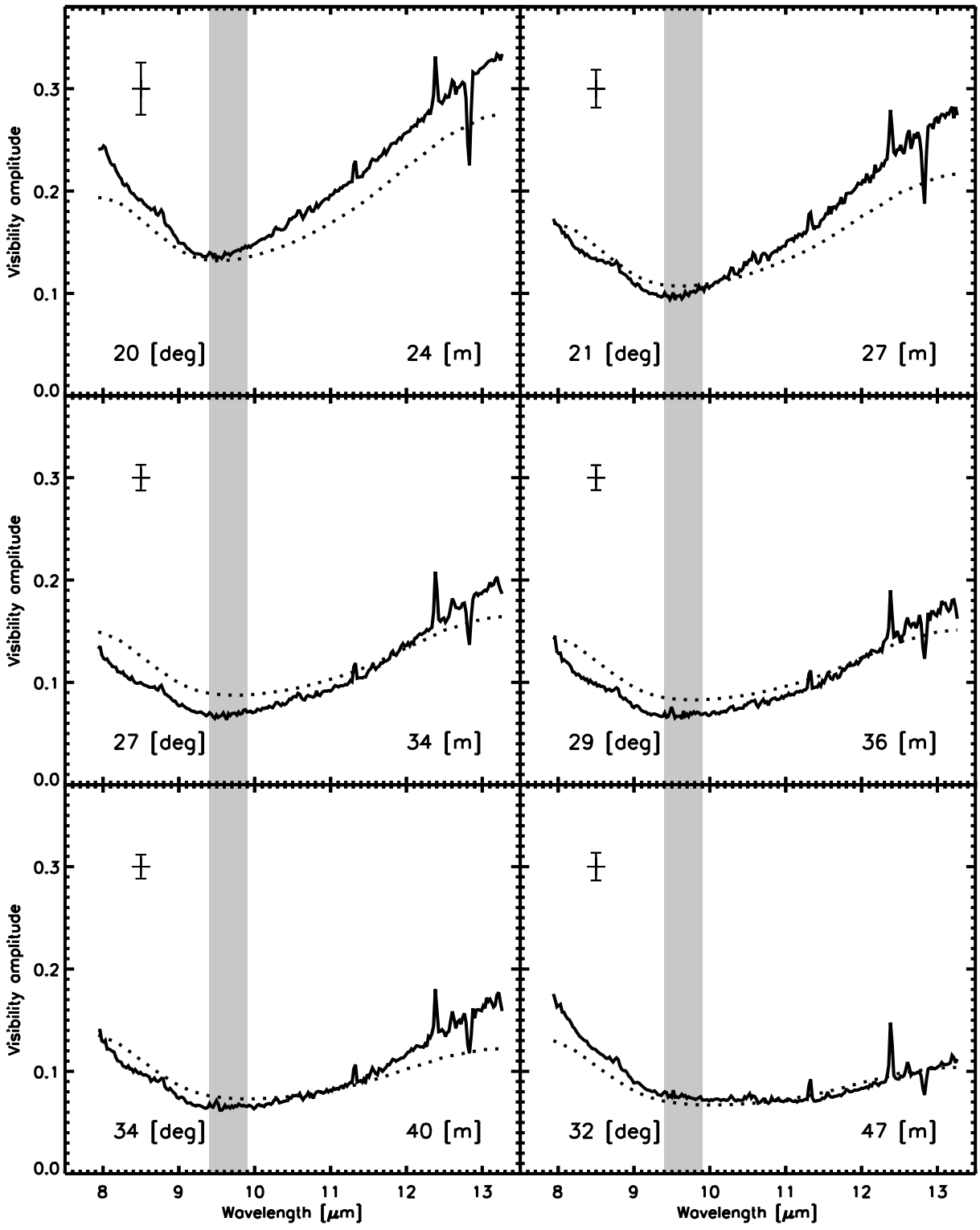

Figure 3.6 — Each panel displays the calibrated visibility amplitude of MWC 349A as function of wavelength for one observed (u,v) point. The position angles and projected length of the employed baselines are indicated in the lower left and right corners of each panel. Also indicated is the uncertainty for each measurement, derived from the scatter of the calibrators in that night. The gray areas indicate wavelength regions at which ozone in the Earth's atmosphere strongly influences the observed visibilities. The amplitudes measured in these wavelength regions are not included in our analysis. The dashed lines represent visibilities for our best model (see Section 3.3.1).

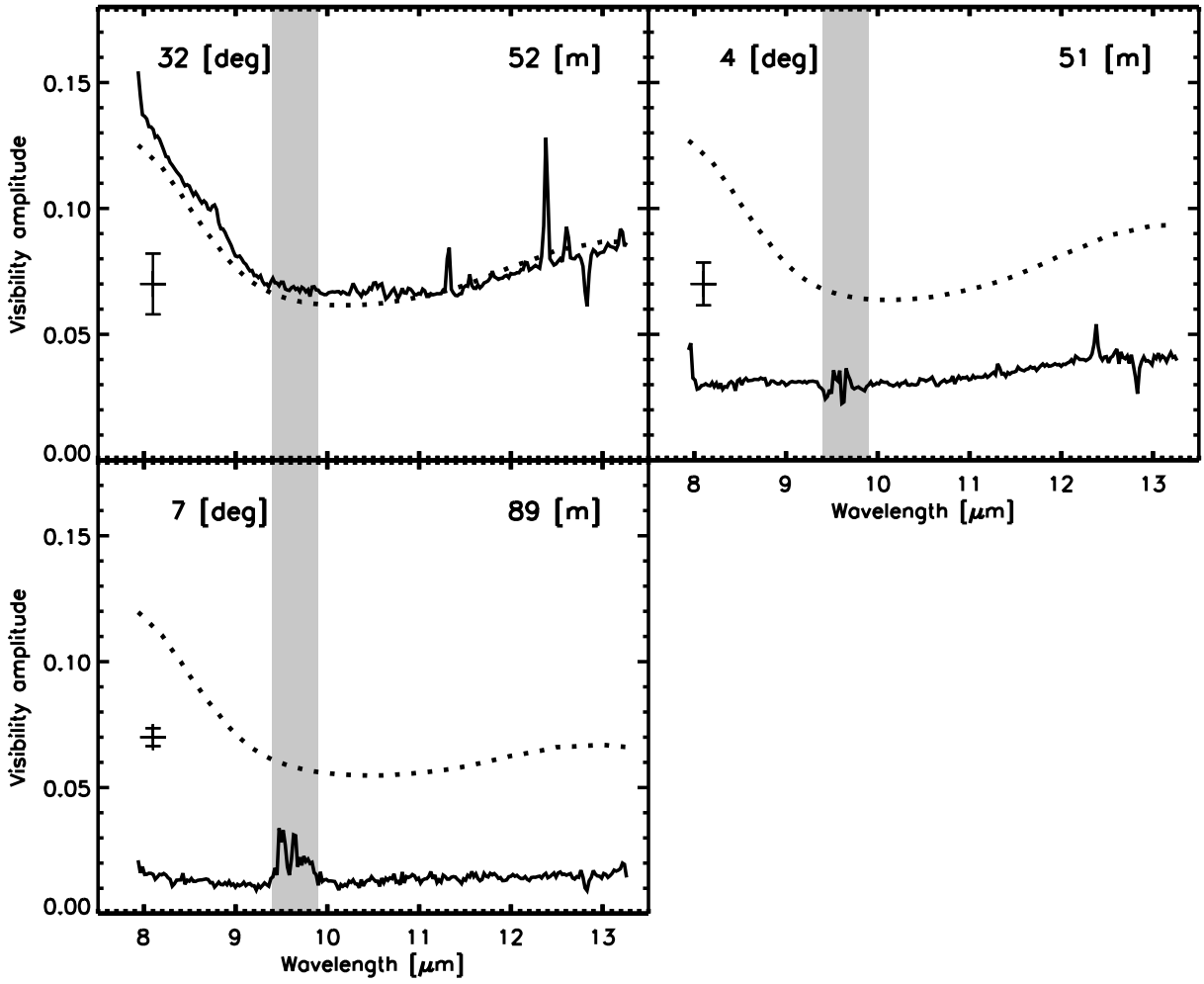

Figure 3.7 — As Figure 3.6, with each panel displaying the calibrated visibility amplitudes as function of wavelength for 3 other (u,v) points from longer baselines. Note the different scale in these panels relative to the panels in Figure 3.6. Also note the strong difference between the visibility amplitude at angles of $\sim 30^\circ$ and $\sim 0^\circ$. The dashed lines represent our best model. The model does not have a directional dependency, so it cannot reproduce the visibilities for the (u,v) obtained at small position angles, which also have not been included in the fits.

and short wavelength regimes of the spectrum, while at wavelengths around $\sim 9.7\,\mu$m one probes *hotter* layers higher above the mid-plane. For these layers the Wien cutoff of the black-body radiation happens at greater radii. This also means that the disk appears bigger around $\sim 9.7\,\mu$m, which reduces the measured visibility amplitude at these wavelengths. See also van Boekel et al. (2005) for a discussion on this subject.

For MWC 349A the rise in visibility amplitudes at longer wavelengths is more pronounced than for Herbig Ae/Be stars. For Herbig Ae/Be stars the dust disk is strongly heated at the inner rim, and depending on whether it is a flaring or non-flaring disk the rest of the disk is more or less in the shadow of the inner rim. In case of MWC 349A the central star with its high flux at short wavelengths generates an H II region around it. This H II region in turn illuminates the dust disk from above and below the disk. This heats up the outer layer of the disk out to distances which are normally in the shadow of the inner rim and cold. Therefore, for the

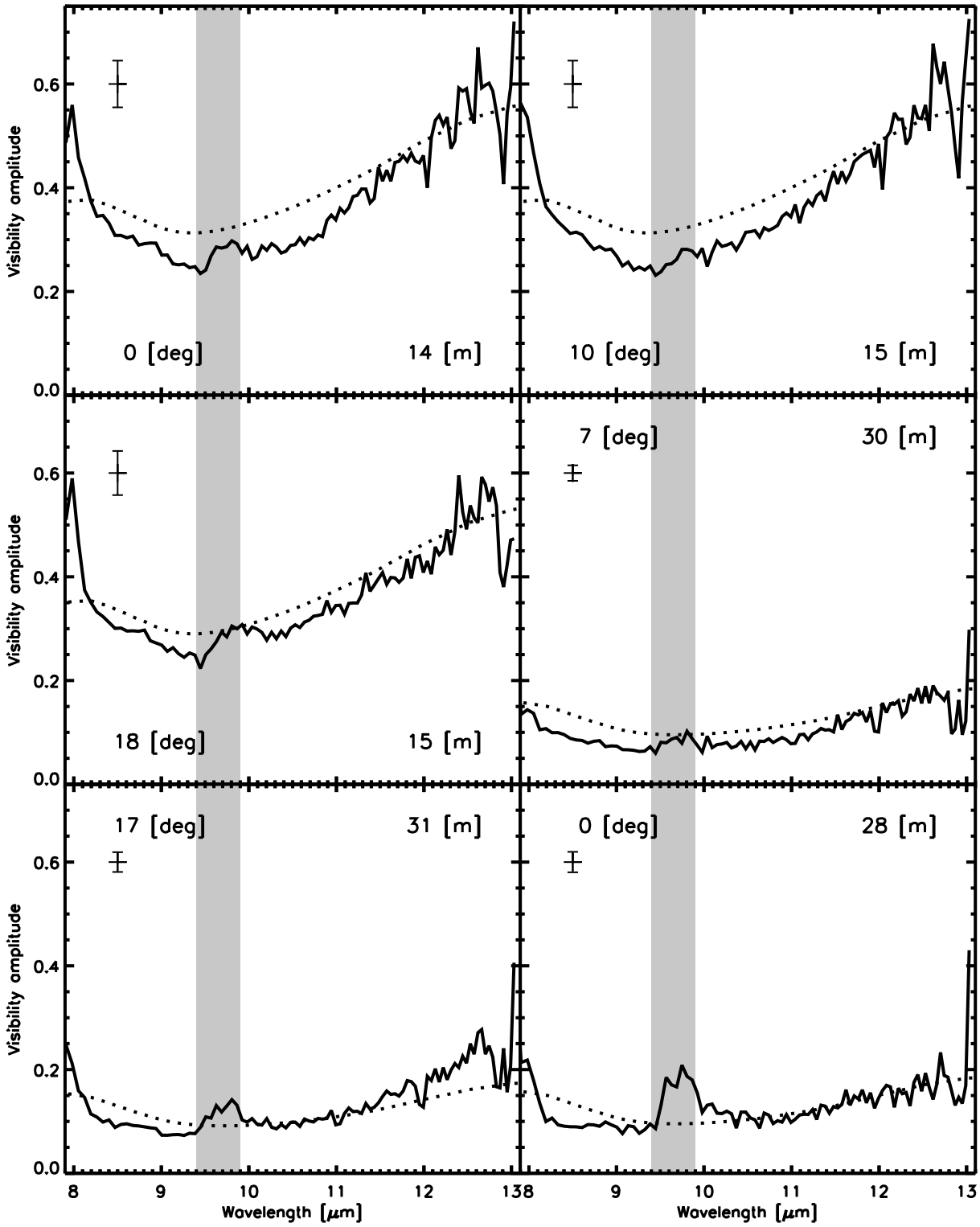

Figure 3.8 — As Figures 3.6 and 3.7. These six visibilities have been obtained using the ATs on the 16m and 32m baselines, covering position angles from $\sim 0°$ to $\sim 30°$. Each panel displays one calibrated visibility amplitude of MWC 349A obtained in Sci_Phot mode using the PRISM.

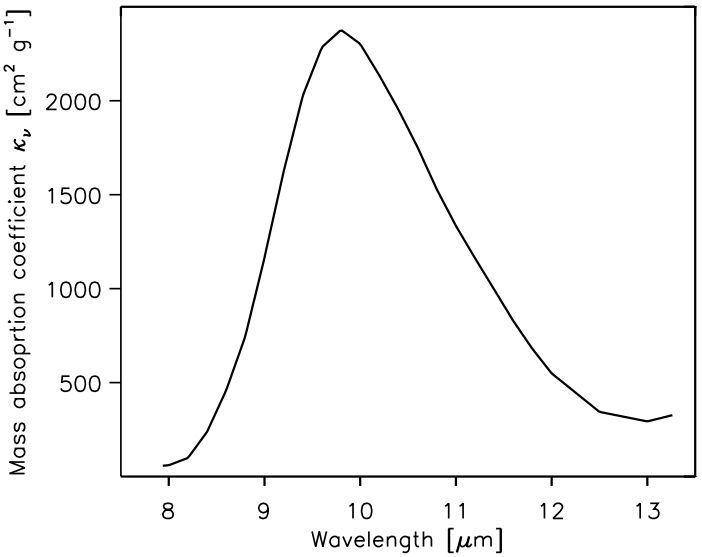

Figure 3.9 — Mass absorption coefficient κ_ν (opacity) of amorphous silicate as a function of wavelength in the pass-band of MIDI. The bulk of the flux in our model originates from the $\sim 300\,\mathrm{K}$ warm extended body whose SED is mainly shaped by the emission of amorphous silicate over almost all of the pass-band, along with amorphous silicate absorption around $9.7\,\mu$m.

case of MWC349A, MIDI probes the proto-planetary disk which has a substantial temperature difference between the layers higher above the midplane and layers close to the midplane. This temperature profile with height exists out to large radial distances.

To test this hypothesis we constructed as simple a model as possible, in which the brightness distribution of the circumstellar disk is represented by two black bodies at different temperatures, whose surface brightness decreases as a power law with $e^{-\frac{r}{\alpha}}$, where 'r' represents the radial distance and 'α' the free parameter determining the size of the black body. We chose this brightness distribution instead of a Gaussian as the temperature of the circumstellar disk decreases radially and assuming only two bodies at two different temperatures might be over-simplified. The gradual decrease in temperature with radius will result in a more "peaked" brightness distribution as represented by a Gaussian and might be better represented by the chosen distribution.

As well as the temperatures and the radial extent of the two bodies, three other free parameters enter the fit. These include the column density of silicate seen by MIDI in the upper layers of the disk. This column density determines the effective shape of the spectra emitted by the silicates in the MIDI pass-band. If the column density is low then the spectral effect due to silicate is strongest. With increasing column density the emission becomes optical thick, first in the middle of the MIDI passband, and later at the borders, until the silicates emit black-body radiation. The second parameter describes the ratio between the radiation originating from the silicates and pure black body radiation, i.e from smaller dust particles. Note that this spectral effect due to silicate emission is only included in the larger, more extended body, as silicates would not survive in the hotter smaller component. The final parameter describes the column density in a cold screen of amorphous silicates through which we see the disk. This parameter, however, does not influence the observed visibility amplitudes, as the visibility represents the ratio between the correlated and the uncorrelated flux. It does, however, influence the shape of the SED derived from the simulated bodies. For the fitting we used the lower S/N SED obtained by the 8m UT telescopes rather than the high S/N SED obtained from the ISO satellite,

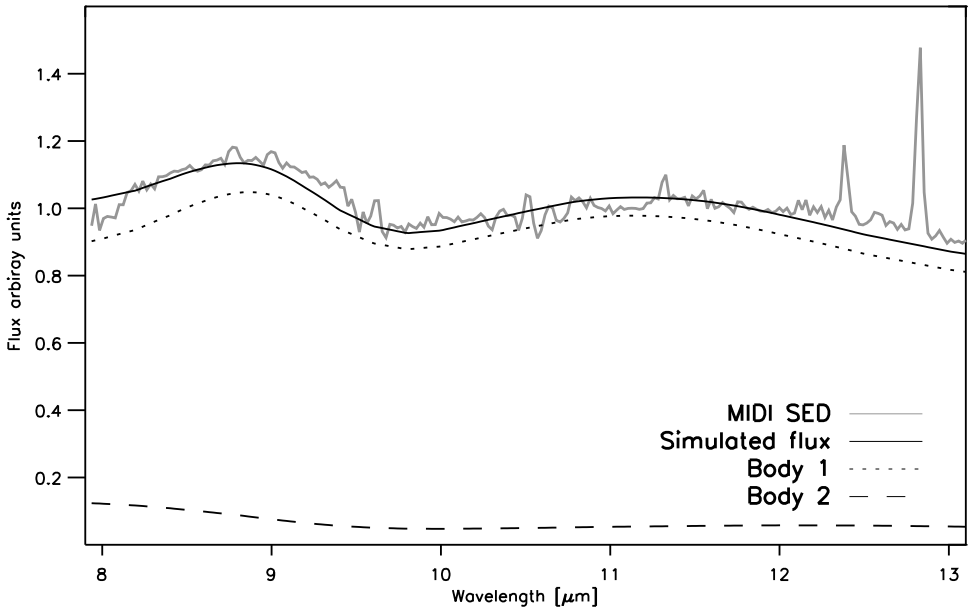

Figure 3.10 — Spectrum of MWC 349A obtained by MIDI using the UT's. Also shown as dashed line is the best fit to the visibility amplitudes and this SED.

because the beam-size of the latter is considerable bigger and therefore contains a less clean spectrum of MWC 349A. We did not attempt to calibrate the MIDI SED on an absolute scale as the extinction is not known precisely enough. Therefore the parameter found for the column density for silicate has only a limited physical meaning. Note that we included neither an inner hole, nor the star itself in our model. These were not needed as the inclination of the disk is thought to be around $\sim 70^{\circ}$, obscuring our view of the star and the inner region cleaned of dust by the intense radiation. We may, however, see one hot wall of the inner rim, which we represented here as the small hot body. The inner rim represents the inner surface of the dust disk which sees the star directly and the innermost radius where dust can survive. A simultaneous fit to the visibility amplitude in all MIDI bands (excluding the wavelengths where emission lines have been found and the wavelength region influenced strongest by Earth's atmosphere) and the scaled SED of MWC 349A in the MIDI pass-band, was carried out. We did not use an absolute scale for the SED because the absorption towards MWC 349A is not known precisely enough to further constrain the fit. Figure 3.10 displays the SED of MWC 349A in the wavelength band of MIDI, over-plotted with the fit of two black-bodies plus the effect from the silicate emission in the disk and absorption. As MWC349A has an almost edge-on disk one expects to see a certain amount of silicate in absorption as the emission from the warm disk will be seen through colder

Table 3.2 — The parameters derived from the χ^2 fit to the continuum visibility amplitudes and the SED measured by MIDI. The values in AU are given for an assumed distance of 1.2 kpc. See Section 3.3.1 for a discussion on the uncertainties.

Parameter	Best fit value
T_1	310 [K]
Surface brightness decreased by e^{-1}	0.12 [″]
Surface brightness decreased by e^{-1}	150 [AU]
ratio emission silicates/pure black body	0.21
T_2	1700 [K]
Surface brightness decreased by e^{-1}	0.0005 [″]
Surface brightness decreased by e^{-1}	0.7 [AU]

material in the outskirts of the disk. In Figures 3.6, 3.7, and 3.8 the model visibility amplitudes obtained from the fit are shown as dashed lines along with the measured visibility amplitudes from MIDI. The parameters, which fit the SED and visibility amplitudes best, are printed in Table 3.2.

Although it is clear that there is a strong directional dependency of the visibility amplitudes (see Figure 3.7 and references mentioned in the introduction), we kept this simple model with only a radial dependence of the visibilities because it was only possible to obtain measurements at position angles between $\sim 0^\circ$ and $\sim 30^\circ$. With the position angle of MWC 349A's elongation axis being $\sim 100^\circ$ degrees this means that it is not possible to get a reliable axial ratio. Note that the visibility amplitudes at baselines of 16 m and 32 m show only a very weak dependence on position angle, while the visibilities at baseline of ~ 50 m show a strong dependence. This means that the directional dependency is more important for the smaller hotter component than for the colder extended component. We estimate from the use of slightly different brightness distributions that the size parameter derived for the colder body is fairly robust $\sim 30\%$ while the size of the smaller body is only an order of magnitude estimate. The temperature of the colder (~ 300 K) is fairly well constrained by the flat SED of MWC 349A in the N band. The temperature of the smaller body is found vary between 1000 - 1800 K for different models. The ratio between the emission by silicates and pure black body radiation is a function of the chosen mass absorption coefficient, which we assumed to be that of small amorphous silicate grains. Finally, we find that the density of amorphous silicate along the line of sight is so low that its emission does not become optically thick. This finding is not surprising as the silicate resonance is the feature in our model which is mainly responsible for reproducing the characteristic observed visibility amplitude change with wavelength.

3.3.2 Hydrogen lines

The observed visibilities show a rich structure as a function of wavelength, due to the presence of strong emission lines. This makes it possible to independently probe the sizes and geometries of the disk, and the regions in which the hydrogen recombination lines originate. The MIDI visibility amplitudes and phases, for which one (u, v) sample is shown in Figure 3.4 and Figure

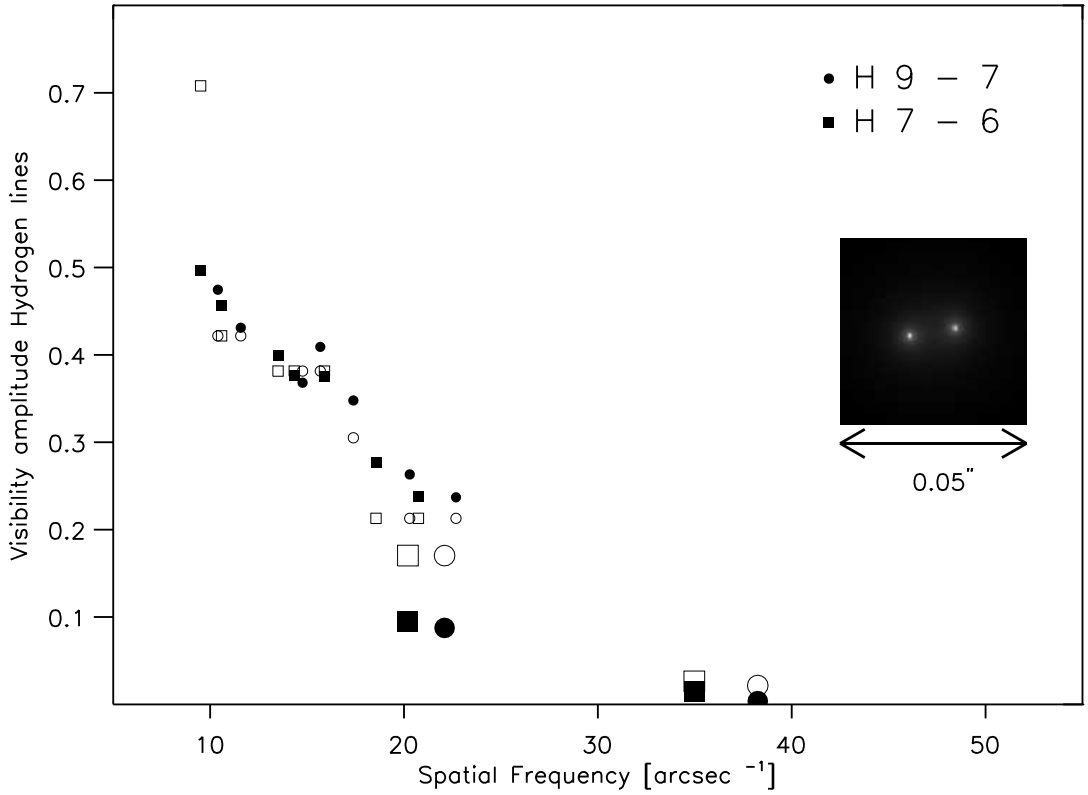

Figure 3.11 — Visibility amplitudes of the hydrogen recombination lines plotted as a function of spatial frequency. The filled squares indicate visibilities measured for the H 7-6 line and the open squares indicate visibilities measured for the H 9-7 line. Most visibilities have been obtained at wavelengths with position angles of $\sim 30°$. The bigger symbols have been obtained at an position angle of $\sim 0°$. The closed symbols represent the measurements, and the open symbols the calculated visibility amplitudes for our best fitting model for the hydrogen lines. The small pictogram shows the sky brightness distribution of this model (see Section 3.3.2)

.

3.5, provide information on a number of strong emission lines. We indicated in these plots the positions of all hydrogen lines which lie in the passband of MIDI.

In order to obtain the visibility amplitudes for the emission lines, the flux from the continuum has to be subtracted at the wavelengths of the emission lines in the correlated, and uncorrelated flux. The visibility $V_{\rm line}$ is then obtained by dividing these two quantities,

$$V_{line} = \frac{\mathrm{Cor_{line}} - \mathrm{Cor_{cont}}}{\mathrm{Pho_{line}} - \mathrm{Pho_{cont}}}, \tag{3.1}$$

where 'line' indicates a measurement of the total flux in the wavelength channels of a line and 'cont' indicates flux measurements in the adjacent continuum channels interpolated to the

Table 3.3 — Parameters derived from the fit to the visibility amplitudes of the H 7-6 and H 19-7 lines. See Section 3.3.2 for a discussion on the uncertainties.

Parameter	Best fit value
Distance of the emitting regions from each other	18 [mas]
Power law index α	1.2

wavelength of the emission line. 'Cor' stands for a measurement of the correlated flux and 'Pho' for the measurement of the total flux. This equation only holds if there is no differential phase between the continuum and the emission line, otherwise one has to calculate the complex visibility including the differential phase. As the phase differences between the lines are relatively small (see Figure 3.5) this can, at the level of the accuracy of our data, be ignored.

Figure 3.11 shows the visibility amplitudes of the two strongest hydrogen recombination lines in the MIDI band, H 7-6 and H 9-7, as a function of the spatial frequency. Note that although H7-6 is blended with H 11-9, which has a flux about ten times lower, we did not correct for this blending. From a comparison of the high visibilities found in the hydrogen lines with the significantly lower visibilities found in the continuum, it is clear that the region from which the hydrogen emission lines originate is a much more compact region than the region from where the continuum emission originates. This can place the emission of these hydrogen lines in the same area as the hydrogen recombination line masers, found at 40 AU in the disk (Martin-Pintado et al. 1989; Thum et al. 1994b). Recent very high S/N ratio observations of the H30α recombination line at 231.9 GHz confirmed these measurements (Weintroub et al. 2008) .

To better understand the distribution of the emission lines in the MIDI passband we create a simple model to reproduce the measured visibility amplitudes. It has been found by the authors mentioned above that most maser activity comes from two areas, each displaced by ~ 0.024 arcsec from the center of MWC 349A. We therefore create a model with two emitting bodies. As free parameters we have the separation of the two bodies from each other and the power law exponent α with which each body decreases in luminosity with radius; $r^{-\alpha}$. The power law index is assumed to be the same for both bodies, and the model is point symmetric around the center of MWC 349A. The last parameter is the position angle of the line which connects these two bodies, which we keep fixed to 100°, the same position angle found observationally for the disk, because we have only a limited number of measurements. Also previous observations suggest that the hydrogen emission line regions have a similar position angle as the disk, which is to be expected if the masers originate from the upper hot layers of the disk (Weintroub et al. 2008). The best fitting parameters are shown in Table 3.3 and the visibility amplitudes inferred are displayed as open symbols in Figure 3.11. Also the sky brightness of our model is shown as an insert in this figure. As in Section 3.3.1 we estimate the uncertainties in the derived parameters by fitting slightly different models to the visibility amplitudes. We estimate for the two parameters shown Table 3.3 an uncertainty of 50%.

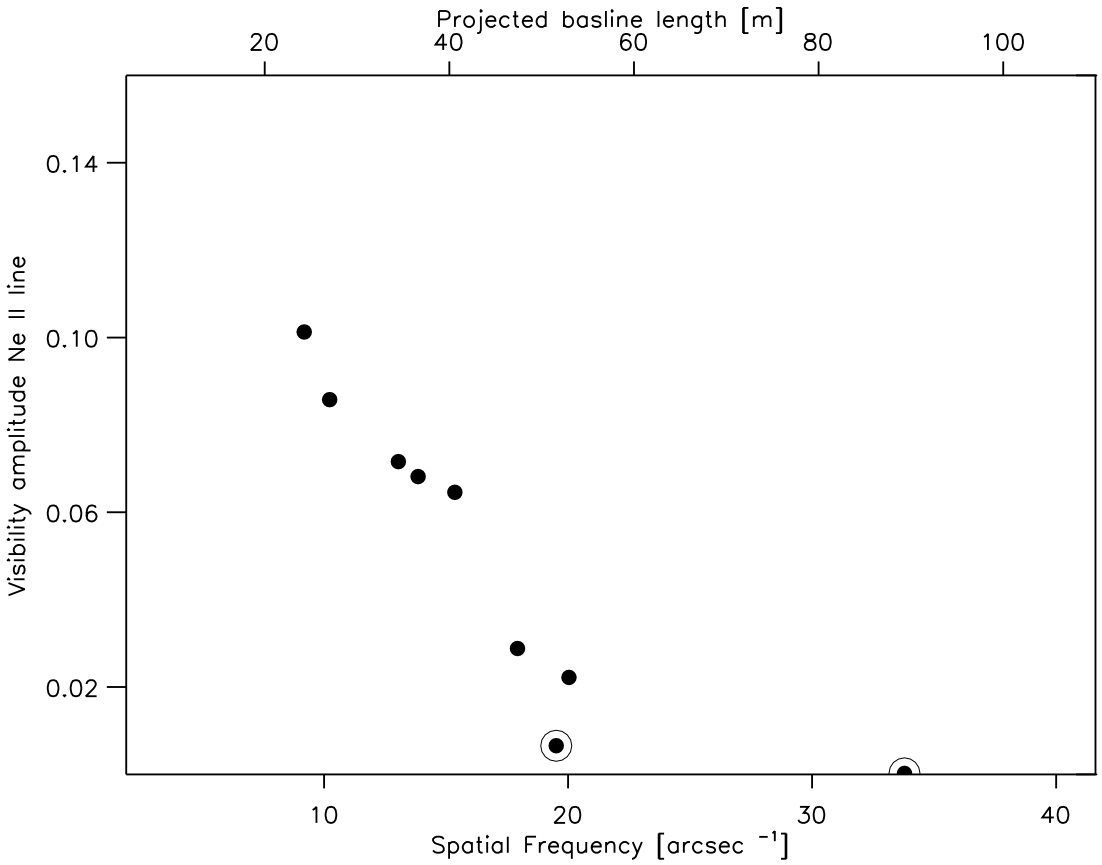

Figure 3.12 — Visibility amplitudes as determined for the [Ne II] line using Equation 3.1 plotted as function of spatial frequency. length. As for the visibilities of the hydrogen lines, most have been obtained at wavelengths with position angles of $\sim 30°$. The symbols which are surrounded by an open circle have been obtained at an position angle of $\sim 0°$.

3.3.3 Forbidden lines

The observed visibility amplitudes decrease at the positions of the forbidden lines [Ne II] 12.81 μm and [Ar III] 8.99 μm, respectively (Figure 3.4). A similar drop would be expected at the position of SIV 10.51 μm, but this line is blended with a strong hydrogen recombination line. Using Equation 3.1 the visibilities in the [Ne II] are calculated and plotted as a function of projected baseline length (i.e. spatial frequency) in Figure 3.12. The low values indicate that the [Ne II] emission is more extended than the hydrogen emission region and the disk emission region at the position angle probed, as expected in models in which the forbidden lines are formed in a wind that originates from the disk. Here we make no attempt to model the brightness distribution of the forbidden lines because the measured visibilities are low and represent the high spatial frequency variations in a brightness distribution with large spatial extent. In the future we intend to used the approach by Alexander (2008) who developed a model for [Ne II] around low mass stars. Since this model is scale free, it can be adapted for MWC 349A.

3.4 Discussion

The simple modelling of the circumstellar disk in Section 3.3.1 allows us to draw some interesting conclusions about the circumstellar material of MWC 349A. The overall shape of the visibility amplitudes with wavelength shows a decrease from short wavelengths towards 10 μm and a rise towards the longest wavelengths, something which could be explained by the influence of amorphous silicates in the disk. This feature also tells us something about the temperature structure of the disk. From the inner radius towards a radius of a few hundred AU the temperature in the disk has to have a strong gradient with height above the mid-plane and the temperature of the disk surface decreases less quickly with radius as for low mass stars.

A change of temperature with disk-height also exists in disks around T-Tauri stars ($M < 2M_{\odot}$) and Herbig AeBe stars ($2 < M_{\odot} M < 8M_{\odot}$). For these stars, however, the circumstellar disk at larger radii can be self-shadowed, and the distance from the star towards the outer parts of the disk, and the angle under which the star is seen by the disk, limit the maximum temperature reached at the surface of the disk at larger radii. This limits the overall contribution to the SED and visibility amplitudes in the N-band of the outer parts of the disk.

Using the models by Dullemond (2002) and Dullemond & Dominik (2004) we tested these assumptions about the disk temperatures heated by a central star. In these models the vertical structure of the disk is determined by hydrostatic equilibrium; dust sublimation creates an inner hole and an iterative process is used to obtain a solution for the temperature profile based on radiative transfer modeling. We have not been able to reproduce the observed visibility amplitudes and SED shape. This is expected as these models have been designed to represent the disks around low to medium mass stars, with the central stars as the main luminosity source. The presence of an ionized region around the central star would however naturally explain the assumed disk temperature structure out to large radii as it would illuminate the disk from *above* and *below*, and would be visible from the disk also at large radii. Our disk modelling shows therefore indirectly, as already shown by the low termination velocity of the wind (50 km s^{-1}), the presence of a H II region around the central star of MWC 349A. Currently we are implementing the effect of a Strömgren-sphere into the model by Dullemond (2002).

What can we say about the mineralogy of the disk? Having found that the measured visibility amplitudes can be modelled using small unprocessed amorphous silicate grains, does not mean that this is the dominant species in the disk. More processed species may not leave a signature in the visibility amplitudes as these bigger grains settle down towards the mid-plane of the disk, where they are difficult to observe, due to the optical depth and reduced temperature.

The derived size for the disk at 300 K is in agreement with what is found by Danchi et al. (2001), taking into account the smaller wavelengths used by these authors, and the resulting greater sensitivity to hotter structures. They found linear sizes of 44 AU and 57 AU at 1.65 μm and 2.27 μm, respectively. Our estimate of the decrease of the disk brightness to e^{-1} at 150 AU does however only refer to the brightness distribution along a position angle of $\sim 30°$. As explained above we did not include any directional dependency in our model, even if it is evident from earlier studies (e.g Danchi et al. 2001) that this should be present. The relatively small dependence of the lowest spatial frequencies (larger structures) on the position angle (Figure 3.8) and the strong dependency of the high spatial frequencies (smaller structures) on the position angle (Figure 3.7) shows that the innermost, hottest parts of the disk, can be interpreted as observing the hot inner wall of the inner rim which is directly illuminated by the central star.

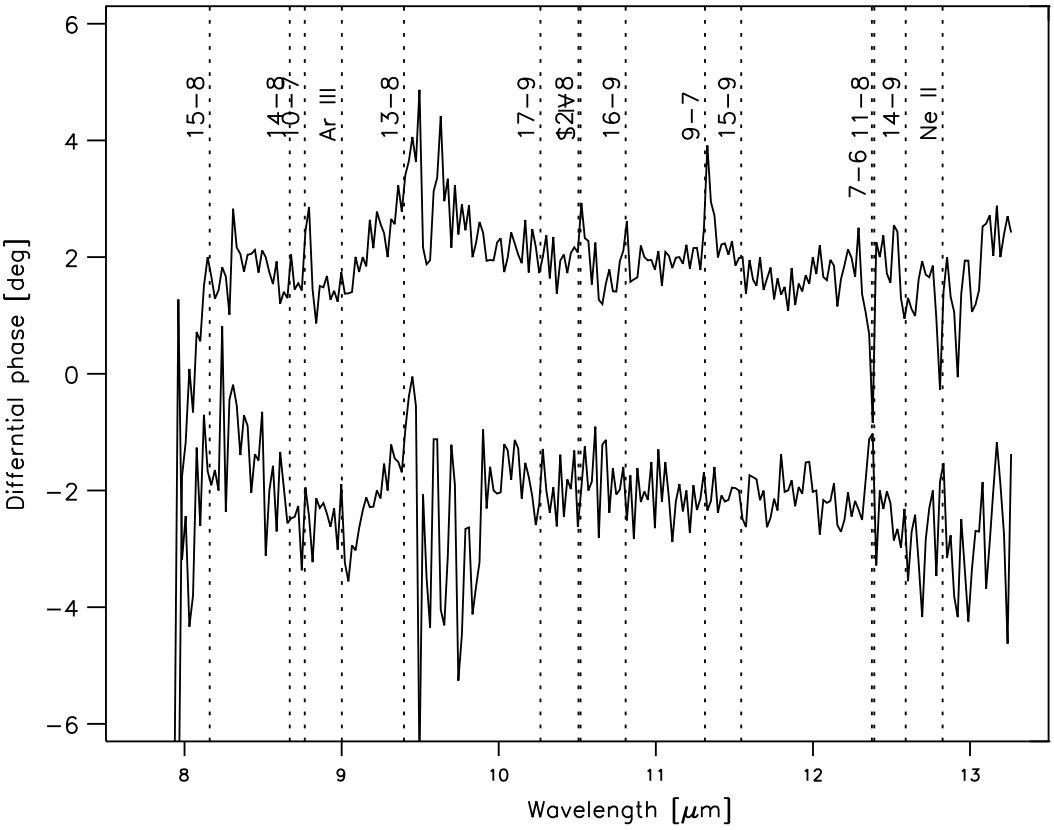

Figure 3.13 — The visibility phases of two (u,v) points. The upper line (moved up by 3 degrees) represents the differential phase obtained at a (u,v) point with a angle of $\sim 32^\circ$ and a projected baseline length of 52m. The lower line (moved down by 3 degrees) represents the differential phase obtained at a (u,v) point with a position angle of $\sim 4^\circ$ and a projected baseline length of 51m. This should be compared to the visibility amplitudes displayed in Figure 3.7.

In Section 3.3.2 we modeled the visibility amplitudes of the H 7-6 line at 12.36 μm and the H 9-7 line at 11.3 μm with a model consisting of two spherical bodies, separated by 18 mas from each other. This model is consistent with these hydrogen lines being emitted in the same region as hydrogen lines with higher n. Our model does not represent the directional dependency of the visibility amplitudes of the emission lines very well. This may be the result of a small mismatch between the position angle of 100° which we fixed in our model, and the real angle. Furthermore, our model may be too simplistic. Even if the bulk of the emission in the hydrogen lines comes from two regions, there is also fainter emission from a bar between the two spots which we have not modeled (see Weintroub et al. 2008).

The phase offset between the lines and the continuum emission shows that there is a small

position offset between the center of the continuum emission and the emission from the hydrogen lines. This is consistent with the picture that the emission lines originate on the "surface" of the inclined circumstellar disk, which produces the offset between the continuum emission and the line emission in the N-S direction, due to the E-W orientation of the circumstellar disk. In this picture there should be little or no offset along the E-W direction for the hydrogen emission. Indeed the differential phase of the two emission lines relative to the continuum for the (u,v) point with a position angle of $\sim 32^\circ$ and a projected baseline length of 52m, is bigger than for the measurement at the (u,v) point of a position angle of $\sim 4^\circ$ and a projected baseline length of 51m (see Figure 3.13). For the latter measurement the phase offset between the H 7-6 line and the continuum is barely detectable. Note however the lower S/N ratio for the latter differences between the continuum flux and the emission lines represent a direct confirmation that there is a small but significant difference in position between the centroid of the continuum flux and the hydrogen emission. This would have been difficult to establish if observations of the continuum and the maser activity would have been done in different observations.

We performed no modeling of the visibility amplitudes and differential phases found for the forbidden lines for reasons explained in Section 3.3.3. We will however in the future try to interpret the measurements for the [Ne II] line emission using the approach developed by Alexander (2008).

3.5 Summary and future work

In this chapter we presented high spatial resolution observations of MWC 349A obtained with the VLTI and MIDI. We showed that the measured visibility amplitudes can be successfully modelled using two black bodies, one hot and small, and another colder and extended, with the colder (300 K) body showing a clear signature of amorphous silicate. We argue that the smaller, hotter body can be interpreted as the inner rim of the disk, which is directly illuminated by the central star. We further argue that the strong silicate feature seen in the visibility curves over all but the highest spatial frequencies is an indication of a strong temperature variation with height in the circumstellar disk. This differentiates this disk around the massive 30 $M_\odot$ star from disks around intermediate and low mass stars, where the silicate resonance feature is seen to a much lesser extent, and where the gradient in disk temperature has a strong radial dependence. Our explanation for the temperature variation with disk height is the presence of an ionized region around the central star, which illuminates the disks from below and above. The use of more physically realistic models should confirm this picture and reveal the dimensions of the different components. It will also reveal the extent to which crystalline silicates are important. Furthermore, we plan to use the phase information obtained by MIDI after their correction for the earth atmosphere using the approach of Tubbs et al. (2004).

We show that the visibility amplitudes found in the hydrogen emission lines can be interpreted by modelling the emission as coming from two regions which are few tens of AU apart, and could represent the inner parts of the circumstellar disk. This is consistent with what is found at radio wavelengths for hydrogen maser lines. Our differential phase measurements of the lines show that the centroid of the continuum emission could come from the same region as

the hydrogen line emission, while there exists a small offset which we will attempt to quantify in a future work. This ties the optical center of MWC 349A firmly together with the center seen in the radio regime.

A further step will be the modeling of the wind, using the constraints from the visibility amplitudes and phases of the forbidden lines. This should ultimately lead to a comprehensive view of the environment of MWC 349A, based on the many complementary data sets that have been obtained for this unique object.

Acknowledgments

We thank Richard Alexander, Kees Dullemond, and Roy van Boekel very much for useful discussions.

APPENDIX

Table A.1 — Log of the MIDI observations of MWC 349A.

Nr.	Target	Night	UT	ra	Dec	Baseline	Base proj.	Mode	Disp. elem.	angle
			[h:m]	[h:m:s]	[d:m:s]	[m]	[m]			[deg]
0	HD120404	2005-05-26	22:57	13 51 47.5	-69 24 4.6	46.6	42.6	HIGH_SENS	P	78.8
1	HD112213	2005-05-27	01:06	12 55 19.4	-42 54 56.1	46.6	45.5	HIGH_SENS	P	50.0
2	HD120404	2005-05-27	02:02	13 51 47.4	-69 24 4.2	46.6	39.6	HIGH_SENS	P	42.6
3	HD112213	2005-05-27	02:54	12 55 19.3	-42 54 56.1	46.6	41.6	HIGH_SENS	P	36.3
4	HD120404	2005-05-27	03:40	13 51 47.5	-69 24 4.3	46.6	36.3	HIGH_SENS	P	22.9
5	Alp_Lyr	2005-05-27	05:30	18 36 56.4	38 47 3.1	46.6	24.1	HIGH_SENS	G	23.3
6	Alp_Lyr	2005-05-27	05:52	18 36 56.4	38 47 3.1	46.6	26.8	HIGH_SENS	G	24.1
7	Del_Lyr	2005-05-27	06:16	18 54 30.2	36 53 56.0	46.6	28.1	HIGH_SENS	G	26.7
8	Del_Lyr	2005-05-27	06:38	18 54 30.2	36 53 56.0	46.6	30.6	HIGH_SENS	G	27.5
9	13_Lyr	2005-05-27	07:04	18 55 20.2	43 56 47.2	46.6	31.5	HIGH_SENS	G	22.2
10	MWC349A	2005-05-27	07:30	20 32 45.6	40 39 37.3	46.6	24.3	HIGH_SENS	G	20.6
11	MWC349A	2005-05-27	07:53	20 32 45.6	40 39 37.3	46.6	27.0	HIGH_SENS	G	22.0
12	Alp_Lyr	2005-05-27	08:17	18 36 56.5	38 47 2.8	46.6	40.4	HIGH_SENS	G	34.5
13	Alp_Lyr	2005-05-27	08:39	18 36 56.5	38 47 2.8	46.6	41.7	HIGH_SENS	G	36.6
14	MWC349A	2005-05-27	09:04	20 32 45.5	40 39 36.3	46.6	34.5	HIGH_SENS	G	27.3
15	MWC349A	2005-05-27	09:28	20 32 45.5	40 39 36.3	46.6	36.6	HIGH_SENS	G	29.4
16	Gam_Cyg	2005-05-27	09:57	20 22 13.7	40 15 23.8	46.6	39.7	HIGH_SENS	G	33.3
17	MWC349A	2005-05-27	10:23	20 32 45.6	40 39 37.6	46.6	40.6	HIGH_SENS	G	34.6
18	hd116870	2005-05-27	23:48	13 26 43.5	-12 42 27.9	56.6	53.0	HIGH_SENS	P	77.7
19	hd116870	2005-05-28	01:25	13 26 43.5	-12 42 27.6	56.6	55.2	HIGH_SENS	P	65.5
20	hd100407	2005-05-28	02:53	11 33 0.1	-31 51 27.9	56.6	49.9	HIGH_SENS	P	49.3
21	hd100407	2005-05-28	04:28	11 33 0.1	-31 51 27.0	56.6	42.1	HIGH_SENS	P	47.3
22	Alp_Lyr	2005-05-28	06:39	18 36 56.4	38 47 1.4	102.4	63.6	HIGH_SENS	G	34.9
23	13_Lyr	2005-05-28	07:06	18 55 20.1	43 56 46.1	102.4	61.7	HIGH_SENS	G	29.5
24	MWC349A	2005-05-28	07:33	20 32 45.5	40 39 37.2	102.4	47.4	HIGH_SENS	G	32.8
25	MWC349A	2005-05-28	07:55	20 32 45.5	40 39 37.2	102.4	52.9	HIGH_SENS	G	32.4
26	Alp_Lyr	2005-05-28	08:48	18 36 56.5	38 47 0.9	102.4	87.3	HIGH_SENS	G	41.5
27	MWC349A	2005-05-28	09:15	20 32 45.5	40 39 36.7	102.4	70.9	HIGH_SENS	G	34.5
28	MWC349A	2005-05-28	09:37	20 32 45.5	40 39 36.7	102.4	75.2	HIGH_SENS	G	35.8
29	MWC349A	2005-05-28	10:00	20 32 45.5	40 39 36.7	102.4	79.3	HIGH_SENS	G	37.3
30	MWC349A	2005-05-28	10:22	20 32 45.5	40 39 36.7	102.4	82.9	HIGH_SENS	G	38.9
31	Eps_Cyg	2005-05-28	10:49	20 46 12.8	33 58 14.0	102.4	89.2	HIGH_SENS	G	43.1
32	HD165135	2005-07-20	23:12	18 5 48.4	-30 25 29.2	62.5	41.3	HIGH_SENS	P	5.7
33	HD165135	2005-07-20	23:21	18 5 48.4	-30 25 29.2	62.5	42.9	HIGH_SENS	P	4.3
34	HD165135	2005-07-21	00:33	18 5 48.4	-30 25 29.1	62.5	53.4	HIGH_SENS	P	-4.7
35	HD178345	2005-07-21	01:57	19 10 1.7	-39 20 27.5	62.5	55.4	HIGH_SENS	P	-2.5
36	HD173484	2005-07-21	02:55	18 46 47.2	-29 37 54.0	62.5	61.6	HIGH_SENS	P	-16.4
37	HD165135	2005-07-21	03:43	18 5 48.5	-30 25 27.4	62.5	61.8	HIGH_SENS	P	-27.6
38	HD173484	2005-07-21	04:57	18 46 47.2	-29 37 53.4	62.5	60.4	HIGH_SENS	P	-32.4
39	GamCyg	2005-07-21	06:12	20 22 13.7	40 15 23.3	62.5	53.5	HIGH_SENS	G	0.9
40	MWC349A	2005-07-21	06:40	20 32 45.5	40 39 37.2	62.5	51.6	HIGH_SENS	G	4.1
41	hd150052	2005-08-24	23:22	16 38 47.7	-8 37 6.3	89.4	89.4	HIGH_SENS	P	7.8
42	HD157236	2005-08-25	01:40	17 23 21.5	-28 8 34.0	89.4	81.5	HIGH_SENS	P	-4.1
43	GamCyg	2005-08-25	02:51	20 22 13.7	40 15 24.4	89.4	88.7	HIGH_SENS	G	4.0
44	MWC349A	2005-08-25	03:25	20 32 45.5	40 39 37.4	89.4	89.3	HIGH_SENS	G	7.7
45	GamCyg	2005-08-25	03:54	20 22 13.7	40 15 24.3	89.4	89.2	HIGH_SENS	G	14.1
46	hd178345	2005-08-25	04:24	19 10 1.7	-39 20 26.8	89.4	74.2	HIGH_SENS	P	-19.8
47	HD123139	2006-05-25	23:15	14 6 41.0	-36 22 11.8	32.0	28.1	HIGH_SENS	P	54.9
48	HD150798	2006-05-25	23:56	16 48 39.9	-69 1 39.8	32.0	31.9	HIGH_SENS	P	88.3
49	HD150798	2006-05-26	01:17	16 48 39.9	-69 1 39.8	32.0	32.0	HIGH_SENS	P	68.9
50	HD150798	2006-05-26	01:32	16 48 39.9	-69 1 39.8	32.0	32.0	HIGH_SENS	P	65.3
51	HD150798	2006-05-26	02:58	16 48 39.9	-69 1 39.8	32.0	32.0	HIGH_SENS	P	45.3
52	HD150798	2006-05-26	03:38	16 48 39.9	-69 1 39.8	32.0	31.9	HIGH_SENS	P	36.1
53	HD150798	2006-05-26	04:19	16 48 39.9	-69 1 39.8	32.0	31.7	HIGH_SENS	P	26.8
54	HD150798	2006-05-26	05:27	16 48 39.9	-69 1 39.8	32.0	31.0	HIGH_SENS	P	11.3
55	HD146051	2006-05-26	07:27	16 14 20.7	-3 41 39.6	32.0	26.9	HIGH_SENS	P	18.2
56	HD123139	2006-05-26	07:54	14 6 41.0	-36 22 11.8	32.0	13.5	HIGH_SENS	P	-45.9
57	MWC349	2006-05-26	08:51	20 32 45.4	40 39 36.8	32.0	30.3	SCI_PHOT	P	7.0
58	MWC349	2006-05-26	09:03	20 32 45.4	40 39 36.8	32.0	30.7	HIGH_SENS	G	8.8
59	MWC349	2006-05-26	09:57	20 32 45.4	40 39 36.8	32.0	31.8	SCI_PHOT	P	17.2
60	MWC349	2006-05-26	10:08	20 32 45.4	40 39 36.8	32.0	31.9	HIGH_SENS	G	19.0
61	EpsPeg	2006-05-26	10:34	21 44 11.2	9 52 30.0	32.0	31.9	SCI_PHOT	P	16.6
62	HD120323	2006-06-16	23:54	13 49 26.7	-34 27 2.8	16.0	15.9	HIGH_SENS	P	26.9
63	HD123139	2006-06-17	01:56	14 6 40.9	-36 22 11.8	16.0	15.6	HIGH_SENS	P	11.7
64	HD146051	2006-06-17	03:23	16 14 20.7	-3 41 39.6	16.0	16.0	HIGH_SENS	P	17.6
65	HD169916	2006-06-17	04:19	18 27 58.2	-25 25 18.1	16.0	15.5	HIGH_SENS	P	27.2
66	MWC349	2006-06-17	06:35	20 32 45.4	40 39 36.8	16.0	14.1	SCI_PHOT	P	-0.9
67	MWC349	2006-06-17	06:54	20 32 45.4	40 39 36.8	16.0	14.6	HIGH_SENS	G	2.2
68	EpsPeg	2006-06-17	07:21	21 44 11.2	9 52 30.0	16.0	13.8	SCI_PHOT	P	14.2
69	MWC349	2006-06-17	07:46	20 32 45.4	40 39 36.8	16.0	15.5	SCI_PHOT	P	10.4
70	MWC349	2006-06-17	07:58	20 32 45.4	40 39 36.8	16.0	15.6	HIGH_SENS	G	12.1
71	EpsPeg	2006-06-17	08:24	21 44 11.2	9 52 30.0	16.0	15.4	SCI_PHOT	P	15.3
72	MWC349	2006-06-17	08:39	20 32 45.4	40 39 36.8	16.0	15.9	SCI_PHOT	P	18.6
73	MWC349	2006-06-17	08:50	20 32 45.4	40 39 36.8	16.0	16.0	HIGH_SENS	G	20.3
74	EpsPeg	2006-06-17	09:16	21 44 11.2	9 52 30.0	16.0	16.0	SCI_PHOT	P	17.0
75	HD4128	2006-06-17	09:45	0 43 35.4	-17 59 11.8	16.0	14.2	HIGH_SENS	P	31.4
76	hd120323	2006-06-18	22:45	13 49 26.7	-34 27 2.8	16.0	30.4	HIGH_SENS	G	37.0
77	2Cen	2006-06-18	23:09	13 49 26.7	-34 27 2.8	32.0	31.0	SCI_PHOT	P	32.9
78	HD150798	2006-06-19	00:51	16 48 39.9	-69 1 39.8	32.0	32.0	HIGH_SENS	P	52.9
79	2Cen	2006-06-19	03:16	13 49 26.7	-34 27 2.8	32.0	26.4	SCI_PHOT	P	-2.1
80	HD150798	2006-06-19	04:01	16 48 39.9	-69 1 39.8	32.0	30.9	HIGH_SENS	P	9.2
81	HD169916	2006-06-19	06:12	18 27 58.2	-25 25 18.1	32.0	31.4	HIGH_SENS	P	13.7
82	MWC349	2006-06-19	06:38	20 32 45.4	40 39 36.8	32.0	28.8	SCI_PHOT	P	0.8
83	MWC349	2006-06-19	06:49	20 32 45.4	40 39 36.8	32.0	29.2	HIGH_SENS	G	2.6
84	EpsPeg	2006-06-19	07:15	21 44 11.2	9 52 30.0	32.0	27.7	SCI_PHOT	P	14.3
85	HD187642	2006-06-19	07:34	0 43 35.4	-17 59 11.8	32.0	21.0	HIGH_SENS	P	57.7
86	HD4128	2006-06-19	08:45	0 43 35.4	-17 59 11.8	32.0	25.3	HIGH_SENS	P	40.1
87	BetGru	2006-06-19	09:09	22 42 40.1	-46 53 4.5	32.0	32.0	SCI_PHOT	P	22.2
88	BetGru	2006-06-19	09:29	22 42 40.1	-46 53 4.5	32.0	31.8	SCI_PHOT	P	18.5
89	BetGru	2006-06-19	09:50	22 42 40.1	-46 53 4.5	32.0	31.6	SCI_PHOT	P	14.9

Bibliography

Alexander, R. D. 2008, MNRAS, 391, L64 54, 57
Altenhoff, W. J., Thum, C., & Wendker, H. J. 1994, A & A, 281, 161 38
Baldwin, J. E., Harris, C. S., & Ryle, M. 1973, Nature, 241, 38 38
Danchi, W. C., Tuthill, P. G., & Monnier, J. D. 2001, The Astrophysical Journal, 562, 440 39, 55
Dullemond, C. P. 2002, A & A, 395, 853 55
Dullemond, C. P. & Dominik, C. 2004, A & A, 417, 159 55
Gordon, M. A. 1992, The Astrophysical Journal, 387, 701 38
Hamann, F. & Simon, M. 1986, The Astrophysical Journal, 311, 909 38
Hofmann, K.-H., Balega, Y., Ikhsanov, N. R., Miroshnichenko, A. S., & Weigelt, G. 2002, A & A, 395, 891 39
Leinert, C., Graser, U., Przygodda, F., et al. 2003, Astrophysics and Space Science, 286, 73 39
Leinert, C., van Boekel, R., Waters, L. B. F. M., et al. 2004, A & A, 423, 537 45
Martin-Pintado, J., Bachiller, R., Thum, C., & Walmsley, M. 1989, A & A, 215, L13 38, 39, 53
Martín-Pintado, J., Gaume, R., Bachiller, R., Johnston, K., & Planesas, P. 1993, The Astrophysical Journal Letters, 418, L79 38
Meyer, J. M., Nordsieck, K. H., & Hoffman, J. L. 2002, The Astronomical Journal, 123, 1639 38
Planesas, P., Martin-Pintado, J., & Serabyn, E. 1992, The Astrophysical Journal Letters, 386, L23 38
Quirrenbach, A., Frink, S., & Thum, C. 2001, in ASP Conf. Ser. 242: Eta Carinae and Other Mysterious Stars: The Hidden Opportunities of Emission Spectroscopy, ed. T. R. Gull, S. Johannson, & K. Davidson, 183 38, 39
Tafoya, D., Gómez, Y., & Rodríguez, L. F. 2004, The Astrophysical Journal, 610, 827 38
Thum, C. & Martin-Pintado, J. 1994, in ASP Conf. Ser. 62: The Nature and Evolutionary Status of Herbig Ae/Be Stars, ed. P. S. The, M. R. Perez, & E. P. J. van den Heuvel, 265 38
Thum, C., Martin-Pintado, J., & Bachiller, R. 1992, A & A, 256, 507 38
Thum, C., Martin-Pintado, J., Quirrenbach, A., & Matthews, H. E. 1998, A & A, 333, L63 39
Thum, C., Matthews, H. E., Harris, A. I., et al. 1994a, A & A, 288, L25 38
Thum, C., Matthews, H. E., Martin-Pintado, J., et al. 1994b, A & A, 283, 582 38, 39, 53
Tubbs, R. N., Meisner, J. A., Bakker, E. J., & Albrecht, S. 2004, in Society of Photo-Optical Instrumentation Engineers (SPIE) Conference Series, Vol. 5491, Society of Photo-Optical Instrumentation Engineers (SPIE) Conference Series, ed. W. A. Traub, 588 57
van Boekel, R., Dullemond, C. P., & Dominik, C. 2005, A&A, 441, 563 47
Weintroub, J., Moran, J. M., Wilner, D. J., et al. 2008, ApJ, 677, 1140 53, 56
White, R. L. & Becker, R. H. 1985, The Astrophysical Journal, 297, 677 38

Chapter 4

The spin axes orbital alignment of both stars within the eclipsing binary system V1143 Cyg using the Rossiter-McLaughlin effect.

The Rossiter–McLaughlin (RM) effect, a rotational effect in eclipsing systems, provides unique insight into the relative orientation of stellar spin axes and orbital axes of eclipsing binary systems.

Our aim is to develop a robust method to analyze the RM effect in an eclipsing system with two nearly equally bright components. This gives access to the orientation of the stellar rotation axes and may shed light on questions of binary formation and evolution. For example, a misalignment between the spin axes and the angular momentum of the system could bring the observed and theoretical apsidal motion into better agreement for some systems, including V1143 Cyg.

High-resolution spectra have been obtained both out of eclipse and during the primary and secondary eclipses in the V1143 Cyg system using the 0.6 m Coudé Auxiliary Telescope (CAT) and the Hamilton high-resolution spectrograph at the Lick Observatory. The Rossiter–McLaughlin effect is analyzed in two ways: (1) by measuring the shift of the line center of gravity during different phases of the eclipses and (2) by analysis of the line shape change of the rotational broadening function during eclipses.

We measured the projection of the stellar rotation axes using the rotation effect for both main-sequence stars in an eclipsing binary system. The projected axes of both stars are aligned with the orbital spin within the observational uncertainties, with the angle of the primary rotation axis $\beta_p = 0.3 \pm 1.5^\circ$, and the angle of the secondary rotation axis $\beta_s = -1.2 \pm 1.6^\circ$, thereby showing that the remaining difference between the theoretical and observed apsidal motion for this system is not due to a misalignment of the stellar rotation axes. Both methods utilized in this paper work very well, even at times when the broadening profiles of the two stars overlap.

S. Albrecht, S. Reffert, I.A.G. Snellen, A. Quirrenbach & D. S. Mitchell
A&A, **474**, 565 (2007)

HIP	96620	
R.A.$_{J2000}$	$19^h38^m41^s$	‡
Dec.$_{J2000}$	$54°58'26''$	‡
Parallax	$0''.02512(56)$	‡
Vmax	5.89 mag	‡
Sp. Type	F 5 V	†
Period	$7^d.6407568(6)$	⋆
Inclination	$87.0(1)°$	†
Radius$_p$	$1.346(23)R_\odot$	†
Radius$_s$	$1.323(23)R_\odot$	†
L_s/L_p	0.96(3)	†

Table 4.1 — Parameters for V1143 Cyg taken from Hipparcos (1997)‡, Andersen et al. (1987)† and Giménez & Margrave (1985)⋆. Radius$_p$ denotes the radius of the primary component and Radius$_s$ the radius of the secondary component. L_s/L_p denotes the luminosity ratio between the secondary and primary.

4.1 Introduction

Eclipsing binaries are great stellar laboratories for gathering information on stellar surface structure. During eclipses, varying parts of the stellar disk are obscured, allowing the observer to gather spatially resolved information. Without eclipses, this information is hardly accessible.

The crossing of a companion in front of a rotating star causes a change in the line profile of the eclipsed star as, for example, it first covers mainly the part of the stellar surface which is moving towards the observer. This change in the line profile results in a change in the center of gravity of the line and therefore in a change in the measured radial-velocity of the star. The strength and shape of this rotation effect is a function of the projection of the stellar axes on the sky, its inclination (for stars with differential rotation), the projected rotational velocity, the stellar radius, the radius of the companion, the stellar limb darkening, and the orbital parameters of the system.

The rotation effect was first observed by Rossiter (1924) in β Lyrae, and by McLaughlin (1924) in the Algol system. The theory of the rotation effect is well understood (e.g. Kopal 1959, Hosokawa 1953, Ohta et al. 2005, and Giménez 2006). In contrast, observations of the rotation effect in eclipsing binary systems are rare (e.g. Hube & Couch 1982 and Worek 1996). Observation and analysis of the RM effect has recently received renewed interest, caused by the possibility of observing the spin orbital alignment for transiting exoplanet systems (e.g. Queloz et al. 2000 and Winn et al. 2006) and the potential to observe features of the planetary atmosphere (Snellen 2004).

For the successful observation and interpretation of the rotation effect in a planetary system, the required S/N and precision in radial velocity are significantly higher than those required to analyze the RM effect in a stellar binary system. However, the difficulty in analyzing a stellar binary system lies in the fact that one has to deal with the additional light from the eclipsing foreground star. The spectral lines of the two stars normally blend during the eclipses, which makes an analysis of the rotation effect in the framework of the change of the center of gravity during an eclipse difficult. Nevertheless, the observation of the rotation effect is of astrophysical interest in binary systems, as it might reveal the orientation of the stellar rotation axes and provide information about stellar surface velocity fields. The knowledge of these quantities might help to answer questions related to binary formation and evolution, and to the study of apsidal motion.

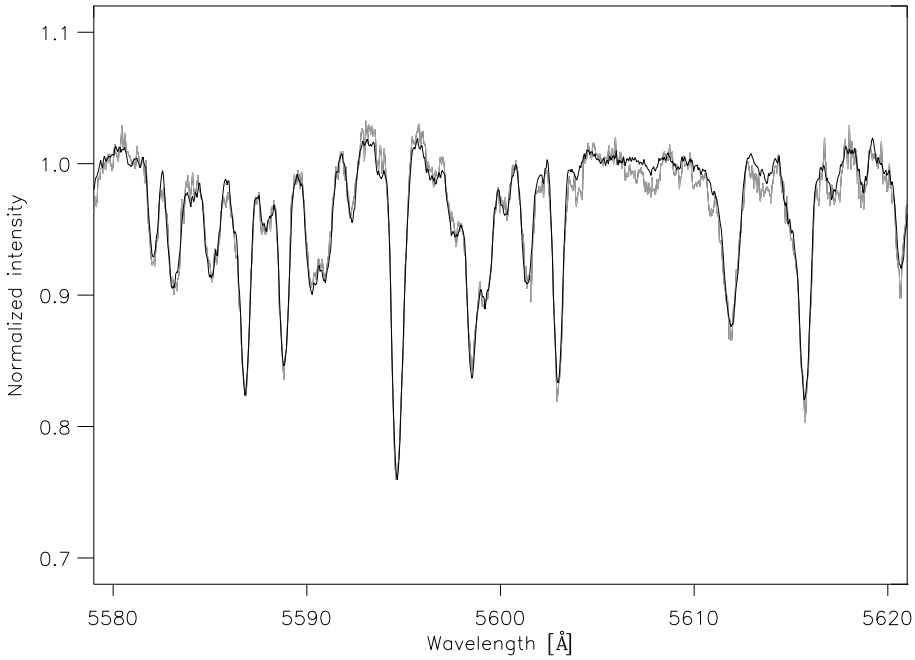

Figure 4.1 — Normalized spectrum of V1143 Cyg covering the wavelength range from 5580 to 5620 Å. The thin line represents the spectrum, and the thick line represents the convolution of the narrow-lined template with the BF obtained using the SVD algorithm. The quality of the representation of the spectrum by the BF and the template is also typical for other wavelength regions.

Accordingly, our aim in this research is twofold: I) to develop a method for deriving information about the orientation of the stellar rotation axes in an eclipsing system with two nearly equally bright components; II) to apply it to an astrophysically interesting system, V1143 Cyg (e.g. Andersen et al. 1987; Giménez & Margrave 1985). V1143 Cyg (Table 4.1) is a bright system consisting of two F5V stars, and has a high eccentricity ($e = 0.54$) that makes it an ideal candidate for testing a new algorithm. Because of the high eccentricity, the spectral lines are not as extensively blended during eclipses. V1143 Cyg is a young ($2 \cdot 10^9$ yr) system (Andersen et al. 1987), and the measured apsidal motion, i.e. the precession of the orbit in its own plane (0.000705 ± 0.000041°/cycle, Giménez & Margrave 1985), is only marginally compatible with what is expected theoretically (0.00089 ± 0.00015°/cycle, Andersen et al. 1987). The precession of the periastron is caused by a general relativistic effect and a Newtonian contribution, the latter consisting of two terms which are due to the deformation of the two stars by tides and stellar rotation. Andersen et al. (1987) suggested the possibility that it could be possible that the tidal evolution has not yet achieved parallel rotation axes of the stars and the orbit. This would reduce the expected apsidal motion, thereby bringing it into a better agreement with the measured apsidal motion.

In the following section we present our observations. Section 4.3 describes the data reduction and the two methods used to derive the orbital and stellar parameters. The results are discussed in Section 4.4. A summary is given in Section 4.5.

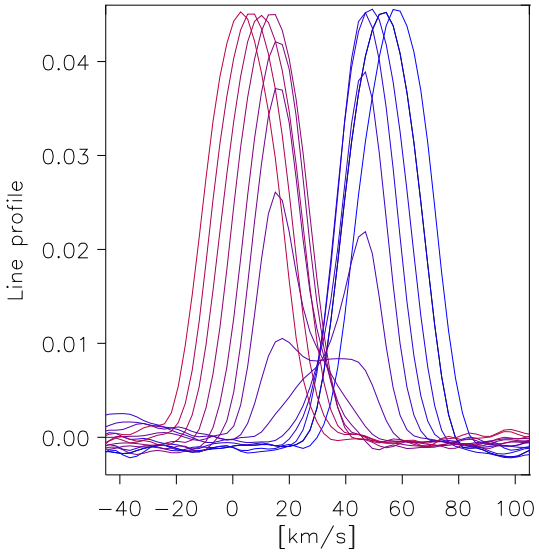

Figure 4.2 — The panel shows two BFs obtained shortly before (higher radial-velocities), nine during, and two after the primary eclipse (lower radial-velocities), with the secondary BF subtracted, in velocity space. One can see how the part of the stellar disk which is moving towards the observer is initially obscured. Later in the eclipse a more central part of the stellar disk is covered while at the end of the eclipse parts of the disk that emit red-shifted light due to the rotation are covered. Note that the BF of the primary is moving through velocity space. These observations were obtained at ≈ 30 min intervals.

4.2 Observations

V1143 Cyg was observed in the summer/autumn of 2005 and 2006 with the 0.6 m CAT telescope at the Lick observatory, equipped with the high-resolution Hamilton Echelle Spectrograph. Observations of the primary eclipse (≈ 4 hours) were made on the night of August 29/30, 2005 with two observations before, nine observations during, and four observations after the eclipse. The central part of the secondary eclipse (≈ 8 hours) was observed during the nights August 04/05 and 27/28, 2005. In addition, another 20 observations were made out of eclipse in order to obtain an accurate orbit model. During each night, we also observed a set of different radial velocity standard stars. Before and after every exposure of V1143 Cyg (≈ 20 min) or a standard star, we made a Thorium-Argon (ThAr) exposure to obtain a wavelength scale taken close in time to the observation, minimizing the influence of drifts in the spectrograph on our measurements. Data from the secondary eclipse taken on August 27/28 had to be discarded from the final analysis, because of an erroneous ThAr wavelength calibration during that night.

4.3 Analysis and results

For our analysis we used a wavelength range from 4430 Å to 5750 Å, excluding the regions with telluric lines, Hβ, and areas for which an insufficient continuum correction was achieved in the spectra (usually the edges of the orders). The first steps of the data reduction consisted of bad-pixel exclusion and continuum normalization. The latter was carried out by fitting a polynomial of 5^{th} order to the spectra and subsequently dividing the spectra by it.

In the next step, a weighted mean of the two wavelength scales, based on the two ThAr spectra obtained directly before and after each observation, was constructed. The weighting took into account time differences of the photon weighted midpoint of the observation and the times of the ThAr exposures. The resulting error in the calculated radial-velocity due to the drift of the spectrograph during the observation was estimated to be 75 m/s on the basis of comparisons of several ThAr exposure pairs.

The Broadening Function (BF) was calculated to retrieve the line profiles of the two stars,

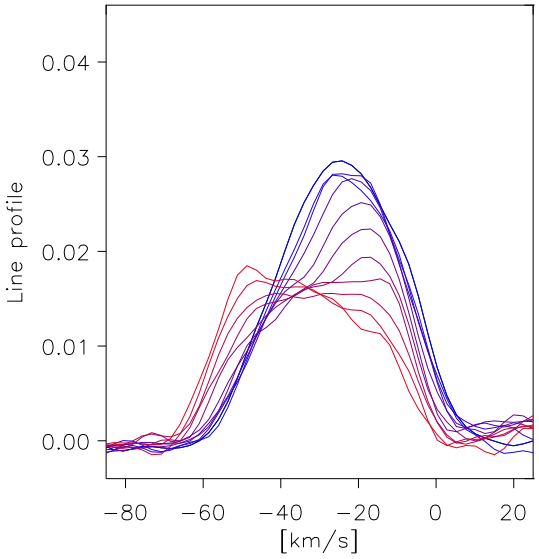

Figure 4.3 — The same as Fig. 4.2 but for the secondary eclipse. One can see BFs of the eleven observations obtained during the secondary eclipse with the line profile of the primary subtracted. The change in radial-velocity during the secondary eclipse is smaller than during the primary eclipse, also the coverage of the secondary is less than the coverage of the primary during its eclipse. This is due to the orbital inclination not being 90°, and the greater distance between the two stars along the line of sight during secondary eclipse (See Fig. 4.5).

governed by the velocity fields on the stellar surface and stellar rotation. The BF represents the function that projects a narrow-lined template onto the broadened spectrum. We calculated the BF using the singular value decomposition (SVD) technique. This approach is clearly described in Rucinski (1999), whereas the SVD algorithm itself can be found in Press et al. (1992).[1] In order to calculate the BF one needs a narrow-lined template; we used the spectrum of the F7V star HD 222368 (Udry et al. 1999), obtained as one of the radial-velocity standard stars. Before using the spectrum of HD 222368 as a narrow-lined template we deconvolved it using the maximum-likelihood method in conjunction with a kernel calculated with the same code as applied in Section 4.3.2. An iterative approach was used to identify the kernel that gave the best results. The most satisfactory results are achieved when using a kernel with a projected rotational velocity ($v \sin i$) of 5 km/s. Figure 4.1 shows a part of a typical spectrum obtained from the V1143 Cyg system. It also shows for comparison the convolution of the narrow-lined template with the BF. As V1143 Cyg is a double-lined binary system with two components of the same spectral type, the BF itself consists of two peaks that represent the broadening functions of the two stars, shaped by the corresponding rotation and velocity fields.

In this study we are primarily interested in the data taken during the eclipses and their interpretation in the framework of the RM effect. Because of the high eccentricity ($e = 0.54$) of the system, the midpoints of the eclipses do not occur when the radial-velocities of the stars are equal, but shortly before and after the time of equal velocity, for the primary and secondary eclipses, respectively. During the middle and the end of the primary eclipse the lines of the two stars are blended. The same situation occurs during the beginning and the middle of the secondary eclipse. Hence, although the line blending is not as severe as in the case of a circular orbit, the light from the foreground star cannot be ignored.

We followed two different approaches to derive the spin axis of the eclipsed star with blended lines. The first method is explained in Section 4.3.1.

[1] We took all singular values until the first derivation of the difference between the observed spectrum and the template broadened by the BF with respect to the singular values used for the calculation of the BF effectively reached zero.

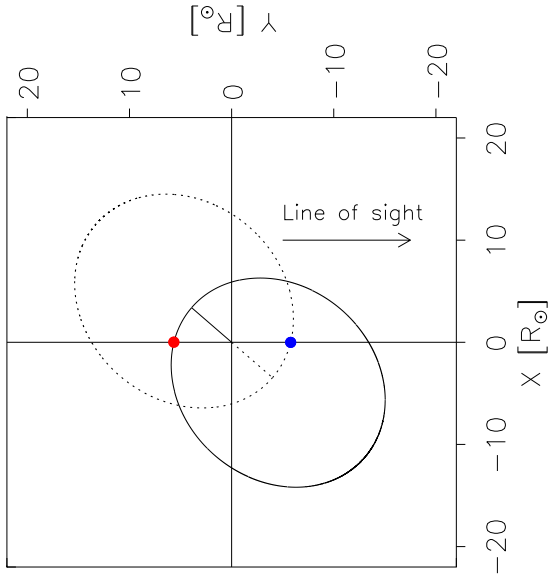

Figure 4.5 — The orbit of the binary system V1143 Cyg shown from above the orbital plane. The solid line represents the orbit of the primary component and the dashed line the orbit of the secondary. The lines from the center of gravity towards the orbits indicate the position of the periastron. The big dots indicate the positions of the stars at time of mid primary eclipse.

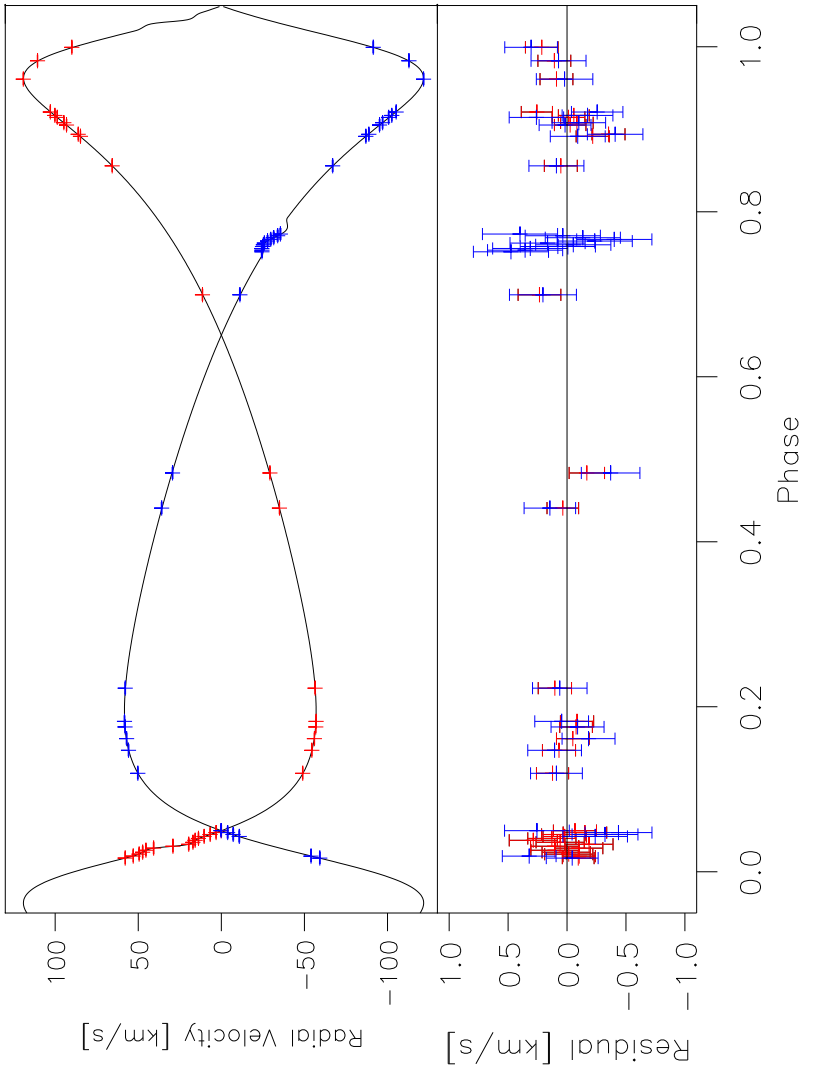

Figure 4.4 — The radial-velocity measurements of the primary and secondary components of V1143 Cyg, and the orbital solution, are plotted against orbital phase. The lower panel shows the difference between the best fit and the actual measurements of the radial-velocities of the primary and secondary component. The midpoint of the primary eclipse occurs at a phase of ≈ 0.03, and the midpoint of the secondary eclipse at a phase of ≈ 0.77. Please note that the systemic velocity in this graph and in Figs. 4.6 and 4.7 is already subtracted

We first show how the influence of the foreground star is subtracted, and subsequently how the center of gravity from the BF of the eclipsed star is calculated. In Section 4.3.2 the BFs of *both* stars are used. Here we do not use the center of gravity of the measured BFs to derive the RM effect, but the shape of the BFs and their change during the eclipse. The measured BFs are compared to simulated BFs, and thereby the parameters that govern the rotation effect are derived.

4.3.1 Method 1: The BF's center

Before determining the parameters involved in the RM effect, an orbital model has to be obtained. To derive the radial-velocities of the components out of eclipse, we fitted two Gaussians to the two peaks in the BFs. A χ^2 fit was applied to extract the orbital parameters. In this work, we adopted the orbital period ($7\overset{\mathrm{d}}{.}6407568 \pm 6 \times 10^{-7}$) for all fits, since it is derived at much higher accuracy from eclipse photometry than from radial-velocity variations (Giménez & Margrave 1985). The inclination of the orbit ($87.0 \pm 0.1^{\circ}$), and the sizes of the components $1.346 \pm 0.023 R_{\odot}$ and $1.323 \pm 0.023 R_{\odot}$ have been adopted from Andersen et al. (1987); these are needed for later analysis. The fitted parameters are shown in the second column of Table 4.2 with their 1-σ uncertainties. In addition, the orbital parameters given by Andersen et al. (1987) and Giménez & Margrave (1985) are shown for comparison in column five.

The tomography algorithm of Bagnuolo & Gies (1991) is used to disentangle the primary and secondary spectra. This algorithm uses the spectra obtained at different phases of the orbit and the orbital parameters of the system as input. It starts with two synthetic spectra without spectral lines for the two components in V1143 Cyg. For all observations taken outside the eclipses, it shifts the observed spectra in the rest-frames of each component using the newly-obtained orbital parameters. Subsequently, the synthetic spectra are compared with the observed spectra. The mean of all the differences between the synthetic and observed spectra is added to the synthetic spectra. This complete process is repeated 50 times, but in our case it converged after only a few iterations.

In the next step, the spectrum of the foreground star is subtracted. For an observation out of eclipse this is straightforward, using the spectrum shifted in velocity space to the appropriate position. During eclipses, one has to incorporate the change in the light ratio of the two stars due to the eclipses. For this we assumed a linear limb darkening law with a limb-darkening coefficient (u) of 0.6 for both stars. Subsequently, the BF was calculated with only one star in the spectrum. Figures 4.2 and 4.3 show the BFs of the primary and secondary stars during their eclipses, after subtraction of the foreground star. Note that, for computational reasons, the continua of the observed spectra were set to zero and the signs of the spectra have been changed; this results in positive BFs.

The center of gravity of the absorption lines can now be extracted from the BFs and used to calculate the radial-velocity of the eclipsed star, including the radial-velocity anomaly introduced by the RM effect. Using the orbital model and the formula by Kopal (1959) and Hosokawa (1953)[2] to calculate the rotation anomaly, the orbital parameters and the parameters relevant for the RM effect of the two stars can be derived jointly with a χ^2 minimization algorithm; therefore $v \sin i$ and the angles β_p and β_s enter as new parameters. β is the angle between

[2]Equation 5 has to be adopted for eccentric orbits.

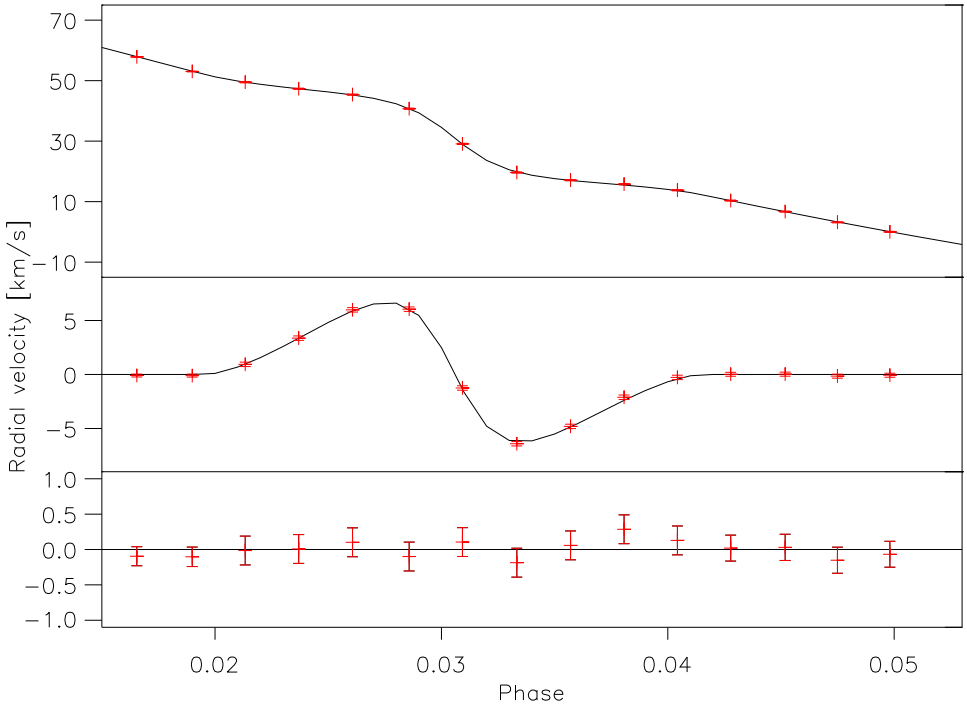

Figure 4.6 — The rotation effect during the primary eclipse. The shift of the center of gravity is plotted against the orbital phase. The upper panel shows the measured radial velocities along with the best fit. In the second panel the radial velocity due to the orbital motion is subtracted from the data and the fit. The residuals between data and fit are shown in the third panel.

the stellar spin axis projected onto the plane of the sky and the orbital spin axis projected onto the plane of the sky. $\beta = 0°$ would indicate a projected rotation axis perpendicular to the orbital plane, whereas $\beta = 90°$ would indicate that the rotation axis lies in the orbital plane. The longitude of the ascending node of the orbit (Ω) is not known, resulting in an ambiguity in the sign of the angle β. In our definition, a positive β indicates that the RM-effect, integrated over the complete eclipse, would give a positive residual in radial-velocity. The companion passes over a larger stellar surface area which is moving towards the observer than over surface area which is moving away from the observer. The linear limb-darkening coefficients of both stars are fixed during the fits to 0.6 as they are only weakly constrained by our fits. In the χ^2 fit, all data points out of eclipse and all data points during the primary and secondary eclipses are fitted simultaneously. Our radial-velocity data points, the best, fit can be seen in Fig. 4.4 for the complete orbit including the two eclipses. Figure 4.5 shows the orbit from a point above the orbital plane. Figures 4.6 and 4.7 display the radial-velocities of the primary and secondary stars during and around their eclipses. The best fit parameters are listed in the third column of Table 4.2 with their 1-σ uncertainties, as derived from the χ^2 fit. All radial-velocity measurements are given with their epochs in Table 4.3 in the Appendix. The radial-velocities directly after the primary eclipse, and the data point at a phase of 0.7, have been extracted using a Gaussian fit to the BF of one star after the subtraction of the other star in the spectrum; however, there is no significant change in the derived parameters if these data points are omitted. The average uncertainties

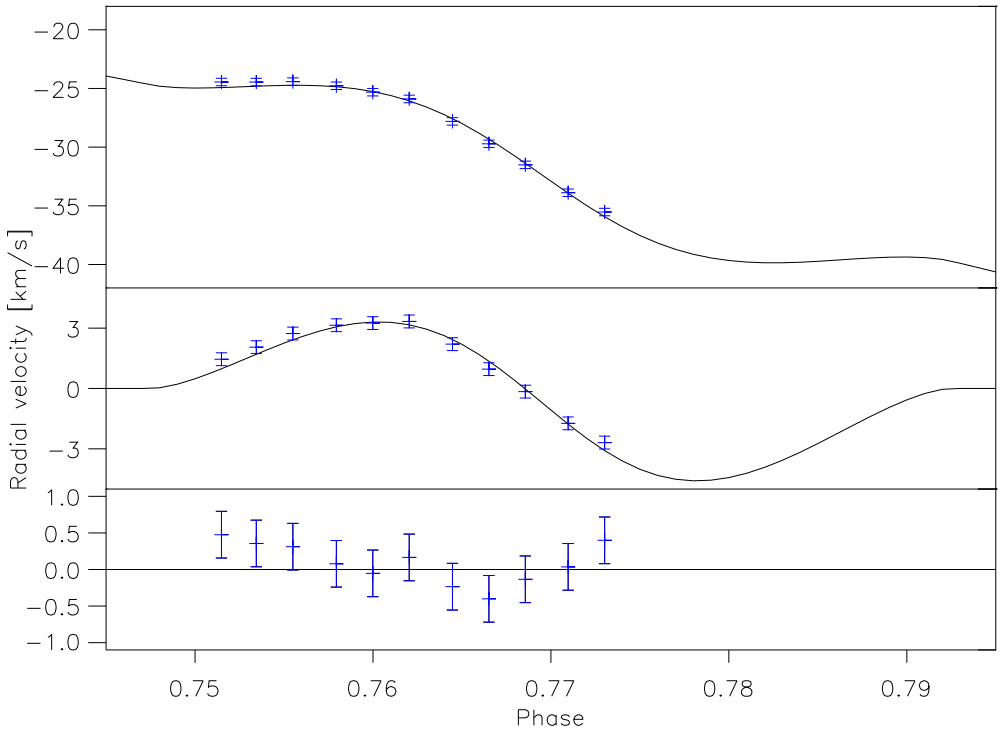

Figure 4.7 — The same as for Fig. 4.6 but this time for the secondary eclipse.

in the radial-velocities, out of the eclipses, are 0.15 km/s for the primary and 0.25 km/s for the secondary. The uncertainties of those radial-velocity measurements that were determined from the centers of the lines, we estimated to be 0.20 km/s for the primary and 0.32 km/s for the secondary. This was calculated by comparing them with the velocities obtained from a Gaussian fit outside the eclipses.

4.3.2 Method 2: Variation of the BF profile

In our second approach, to derive information about the binary orbit and the orientation of the rotation axes, we simulated the shape of the BF of the two stars, as governed by the orbital motion, stellar rotation, orientation of the stellar spin axes, velocity fields on the stellar surface, limb-darkening and, in case of a measurement taken during an eclipse, the fraction of the stellar disk which is covered by the companion at the time of the measurement. These simulated BFs were subsequently compared to the measured BFs, and the relevant parameters determined. With this method, we not only use the first moment of the stellar absorption lines during the analysis, but we utilize the complete BF and its change over the course of the eclipse as a diagnostic tool for determining the orbital and stellar parameters.

We simulated the rotation profile of the two stars in the V1143 Cyg system with a few thousand elements across the visible half-spheres with equal surface brightness. We included linear limb-darkening, asymmetric macro-turbulence and solar-like differential rotation (See Gray 2005). Accordingly, besides the parameters which were fitted in Section 4.3.1, another parameter, the Gaussian width of the macro-turbulence, is required. We kept the σ of the Gaussian for the tangential and radial-velocity fields ζ_{RT} and their covered surface fraction

equal, as the quality of the fit did not improve by including them as free parameters. The inclination of the orbit and the sizes of the two stars can be varied in our fits. However, in the final fits presented here, we used a linear limb-darkening coefficient of 0.6, solid body rotation, and the inclination and radii from the literature (see also Section 4.4).

Each exposure of V1143 Cyg had a duration of ≈ 20 min. Provided that one takes the photon midpoint of the observation, this poses no serious problem for the analysis of the center of gravity of the lines. However, looking at the line profile, one has to take two effects into account. First, the radial-velocities of the two stars change during a 20-min exposure. This effect is strongest in our data set at the time of the primary eclipse, where the change in radial-velocity is $\approx 3\,\mathrm{km/s}$ during one exposure. This artificially widens a BF taken during a 20 min exposure relative to a BF which would have been taken instantaneously. During the eclipses, a second effect becomes important; the coverage of the eclipsed stars can change considerably during 20-min. Again, this effect is stronger during the primary eclipse than during the secondary eclipse, as the primary eclipse is deeper and shorter. Sine we need an exposure over several minutes to receive a sufficiently high S/N ratio[3], we introduced the same 'smearing' in the simulated BFs. We calculated three BFs for each exposure and stacked them together: one simulated observation 6.6 minutes before the photon midpoint, one at the photon midpoint and one 6.6 minutes after the photon midpoint. We convolved each simulated BF with a Gaussian of σ = 2.5 km/s, representing roughly the resolution of the spectrograph in the wavelength range used.

In addition to the parameters describing the binary system, one parameter is included that scales all simulated BFs to the observed BFs. The primary star has a slightly higher luminosity than the secondary. Also, the template used might fit one of the two stars better than the other one. Therefore, we included another parameter scaling the height of the kernels of the two stars relative to each other. As mentioned in the beginning of this section, all spectra have been normalized. During the eclipses the absolute amount of light changes. Hence the depths of the absorption lines change relative to the normalized continuum, and therefore the height of the BFs also change. This has to be incorporated in the calculations of the BFs. We performed a fit using all 46 spectra obtained out of eclipse and during the primary and secondary eclipses. The derived values for the parameters are given in column four of Table 4.2. The measured BFs and the best fits can be seen in Fig. 4.8 for the primary eclipse and in Fig. 4.9 for the secondary eclipse. The uncertainties were calculated using the bootstrap method described in Press et al. (1992).

4.4 Discussion

4.4.1 Orbital parameters

Using the methods described in Section 4.3.1 and Section 4.3.2 we obtained values for the orbital parameters of V1143 Cyg and for the stellar parameters of the two stars. The time of periastron passage of the primary (T), the longitude of the periastron (ω), and the eccentricity (e) were determined in all three fits, and agree with each other to within the 1-σ level.

[3] Out of eclipse the spectra have a S/N between 40 and 50.

Table 4.2 — Derived parameters of V1143 Cyg are given together with their formal errors. The reduced χ^2 of the orbit fit is 0.95 and the reduced χ^2 of the joint fit is 0.96. The average uncertainty in radial-velocity for the primary is 0.16 km/s and 0.27 km/s for the secondary, in the joint fit. For comparison, values given by Andersen et al. (1987) and Giménez & Margrave (1985) are also shown. The second and third columns present the parameters obtained in Section 4.3.1. The fourth column shows the parameters derived with the method presented in Section 4.3.2. For the reasons mentioned in Section 4.4 we consider the values found in Section 4.3.2 to be our best parameters and the formal errors given for $v \sin i$ and ζ_{RT} as too small.

Parameter	Center		Shape	Andersen et al. (1987)†
	Orbit	Joint fit		Giménez & Margrave (1985)⋆
T [JD-2400000]	53536.130±0.002	53536.131±0.002	53536.1317±0.0006	
K_p [km/s]	88.1±0.04	88.1±0.1	88.01±0.05	88.2±0.2†
K_s [km/s]	90.1±0.08	90.1±0.2	89.9±0.1	91.1±0.4†
e	0.538±0.001	0.538±0.001	0.5378±0.0003	0.540±0.003†
ω [°]	49.1±0.2	49.1±0.2	49.27±0.05	49.31±0.06⋆
$a \sin i$ [$R_\odot$]	22.67±0.03	22.67±0.03	22.64±0.02	22.78±0.08†
γ [km/s]	−16.8±0.3	−16.8±0.3	−16.8±0.3	−16.5±0.7†
$M_p \sin^3 i$ [$M_\odot$]	1.357±0.005	1.357±0.008	1.350±0.004	1.386±0.016†
$M_s \sin^3 i$ [$M_\odot$]	1.327±0.004	1.327±0.007	1.322±0.003	1.341±0.013†
$v \sin i_p$ [km/s]		16.9±1.0	19.6±0.1	18±2†
$v \sin i_s$ [km/s]		28.0±5.0	28.2±0.1	27±3†
$\zeta_{RT} P$[km/s]			3.4±0.1	
$\zeta_{RT} S$[km/s]			3.3±0.1	
β_p[°]		0.5±4.0	0.3±1.5	
β_s[°]		−3.9±4.0	−1.2±1.6	

Using the values from Giménez & Margrave (1985) for ω ($48.26 \pm 0.01^\circ$) and the apsidal motion rate ($0.000705 \pm 0.000041^\circ$/cycle), and taking the time difference into account, one would derive an ω of $49.31^\circ \pm 0.06^\circ$ for the time of our observations. This is also the value stated in Table 4.2. The parameter for the semi-amplitude of the secondary (K_s) (90.0 ± 0.1 km/s) falls outside the 1-σ range of the literature value (91.1 ± 0.4 km/s). This difference can also be seen in the values for the projected semi-major axis of the system ($a \sin i$). The uncertainty in the radial-velocity of the center of gravity of the system (γ) includes the uncertainty of the radial-velocity in our template star, HD222368 (5.6 ± 0.3 km/s, Udry et al. 1999). Our calculated masses for the two components in V1143 Cyg are $M_p = 1.355 \pm 0.004\,M_\odot$ and $M_s = 1.327 \pm 0.003\,M_\odot$. These values lie in between the values calculated by Andersen et al. (1987) $M_p = 1.391 \pm 0.016\,M_\odot$ and $M_s = 1.347 \pm 0.013\,M_\odot$, and the values given by Giménez & Margrave (1985) $M_p = 1.33 \pm 0.03\,M_\odot$ and $M_s = 1.29 \pm 0.03\,M_\odot$.

4.4.2 Stellar parameters

The stellar parameters obtained in Section 4.3.1 are derived by analyzing the shape of the rotation anomaly in the radial velocity. The method relies on a clean subtraction of the foreground star from the spectra before calculating the BF's, which depend on orbital parameters derived from out-of-eclipse measurements, values for the stellar radii, the stellar limb-darkening and the light ratio between the two stars during the subtraction process, which have been taken from the literature.

In Section 4.3.2, the change in the shape of the absorption lines is used instead of the rotation anomaly. Looking at Figs. 4.8 and 4.9, one can see that the simulated BFs are somewhat "rounder" during eclipses than the observed BFs. This can clearly be seen during the central phase of the primary eclipse (Fig. 4.8 panels in the second row) and during the secondary eclipse (Fig. 4.9).

The agreement between the measured BF and the observed BF can be improved if u is included in the fit. The derived values for u would be 0.9 ± 0.1 for the primary and 0.8 ± 0.1 for the secondary. As these values are probably to high (Gray 2005) and the derived values for β would not change significantly ($\beta_p = -0.6 \pm 1.4^\circ$ and $\beta_s = -0.3 \pm 1.2^\circ$), we kept u fixed to 0.6 in the final fits.

Including solar-like differential rotation, the orbital inclination and the stellar radii as free parameters in the fits also leads to a better agreement between data and simulation. However, the derived differential rotation parameters are negative for both stars; the angular rotation speed is faster at the poles than at the equator. Furthermore, the fitted radii are not in agreement with the literature values; the primary radius is increased relative to the literature value and the secondary decreased relative to its literature value. The value for the orbital inclination of V1143 Cyg in the literature is reproduced by our fit, but weakly constrained. A negative differential rotation parameter would give the BFs during the eclipses a more box-like shape. A bigger difference between the stellar radii would further improve the agreement between simulation and data during the central part of the primary eclipse. However, a bigger difference in stellar radii would also mean a bigger difference in stellar masses, which would not agree with the nearly equal semi-amplitudes found in the radial-velocity.

We favor a different explanation for the difference of "roundness" between the measured and simulated BFs. Looking at an absorption line originating from one small area of the stellar

disk (i.e. no rotational broadening), the core of an absorption line is formed higher up in the stellar atmosphere than the wings (see Gray 2005), as the same optical depth is reached earlier in the core than in the wings of the absorption line. One can now compare the effect that limb-darkening has on the core and the wings of the absorption lines. In the core of an absorption line, a high optical depth is reached in a high layer of the atmosphere looking down on a stellar atmosphere. This also means that looking from an angle into the stellar atmosphere (i.e. at the limb) will result in a small change in the average height at which the core of the line is formed: Still only the outer cooler parts of the atmosphere are probed. For the wings of the absorption lines the situation is different; the height at which the wings of the observed absorption line are formed changes more from the center to the limb of the stellar disk. Therefore, in going from the center to the limb of a stellar disk the absorption lines become more box-like. The particular shape change of an absorption line originating under different angles relative to the observer depends on the details of the stellar atmosphere. This would result in a non-linear limb-darkening law. Out of eclipse, the light is integrated over the whole stellar surface, but for example, during the central part of the primary eclipse light is only received from the outer part of the stellar disk (See Fig. 4.8, icon in the panel of the third column and second row). Therefore, the shape change of the absorption lines originating from different parts of the stellar disk might explain the difference between the observed BFs and the simulated BFs (e.g., Pierce & Slaughter 1982, Balthasar 1988 or Hadrava 2007).

Using the broadening of about 1000 lines, we obtained macro-turbulence parameters (ζ_{RT}) of 3.4 km/s and 3.3 km/s for the primary and secondary, respectively. For comparison, the macro-turbulence parameter found for the Sun, as a disk-integrated star, for weak and moderately strong lines is ≈ 4.0 km/s (Takeda 1995).

The values obtained for the $v \sin i$ of the secondary, using the two different methods described above, agree with each other and are also consistent with the literature value. Note that there might be a systematic difference between the obtained radial-velocities of the secondary during the secondary eclipse and the fit to the radial-velocities (Fig. 4.7). This might be caused by too high an uncertainty in the orbital parameters used during the data analysis in Section 4.3.1. The values obtained for the primary $v \sin i$ do agree with the literature value within their 1-σ error, but do not agree with each other within their 1-σ errors. The method applied in Section 4.3.1 uses the amplitude of the RM effect to derive the value for the projected rotational velocity. It assumes a linear limb-darkening coefficient. As mentioned in the last paragraph, this might not be sufficient. Also in Section 4.3.2 a linear limb-darkening coefficient is used, but $v \sin i$ is derived not only by the use of the RM effect, but also by the shape of the BF outside of the eclipse. Therefore, we disregard the value for $v \sin i$ obtained in Section 4.3.1 and take the value of 19.6 km/s from Section 4.3.2 as the projected rotational velocity for the primary star in V1143 Cyg. Due to the remaining mismatch between the data and the simulation, which might be due to the use of too simple a model, we consider the formal errors for ζ_{RT} and $v \sin i$ as too small.

We would like to point out that the methods used are still in their infancy. Even with the derived values for the stellar radii, the orbital inclination, limb-darkening and differential rotation are not free of errors yet; these parameters are not normally accessible, or only with great difficulty, via spectroscopic data.

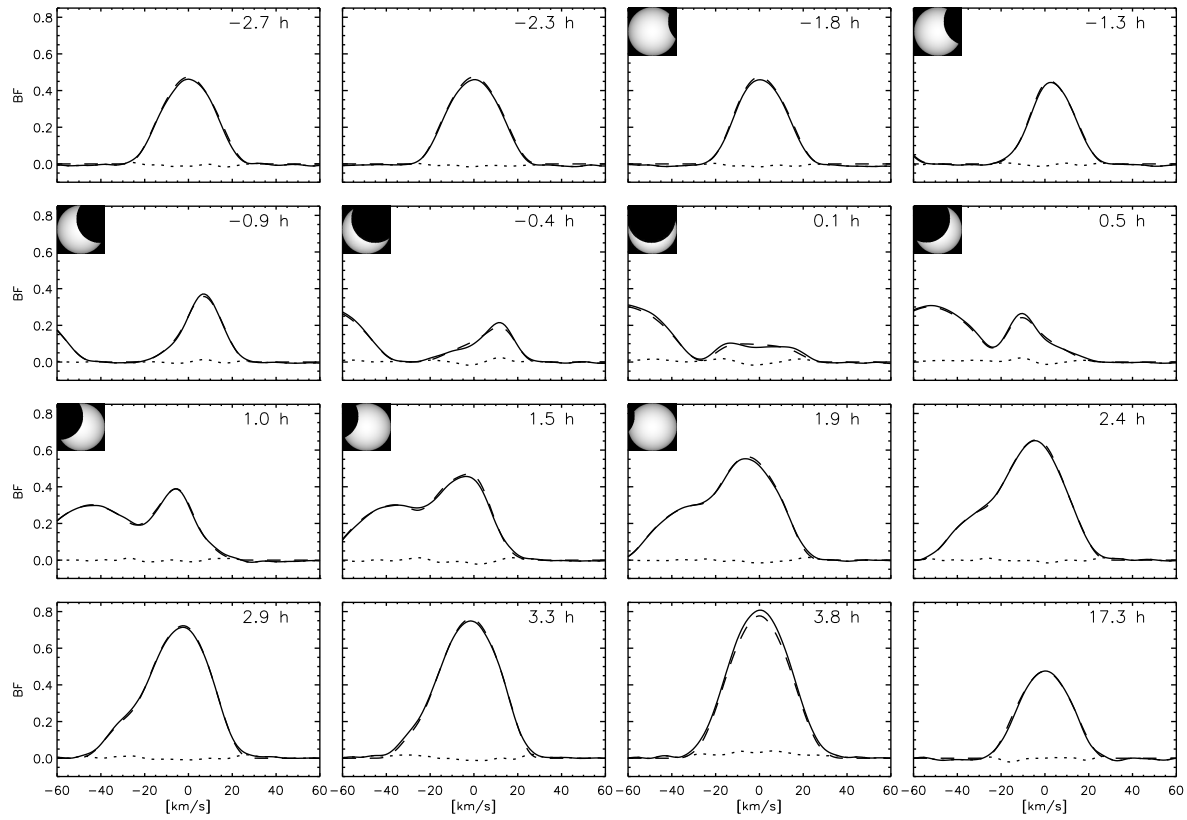

Figure 4.8 — BFs during the primary eclipse centered in the frame of the primary. Each panel represents one measurement. The solid line represents the measured BF, the dashed line shows the best fit BF, while the dotted line represents the difference between the fit and the measurement. The numbers in the upper right corner of each observation indicate the time difference between the midpoint of the observation and the midpoint of the eclipse in hours. In the upper left corner one can see the uncovered part of the primary half-sphere for the midpoint of that measurement if the star was eclipsed during this measurement. One can see that the BF of the secondary moves closer to the primary BF in velocity space over the course of the eclipse. Please note that the scale of the ordinate is arbitrary. The panel in the lower right corner shows the BF of the primary for an observation out of eclipse.

4.4.3 Orientation of the rotation axes

The main focus of this work is the robust determination of the orientation of the stellar rotation axes. The values derived for the projection of the rotation axes onto the plane of the sky are given in the last two rows of Table 4.2. The βs derived from the two different methods agree to within their errors despite the different systematic problems of each method. Therefore, the projections of the rotation axes of both stars are, to within their uncertainties, perpendicular to a vector that lies in the plane of the orbit and is perpendicular to the line of sight. What does that mean for the orientation axes of the stars? It is highly unlikely that the geometry is such that we see the projection of the rotation axes perpendicular to the orbital plane, but that the stellar rotation axes have a high inclination towards the observer. We therefore conclude that the stellar

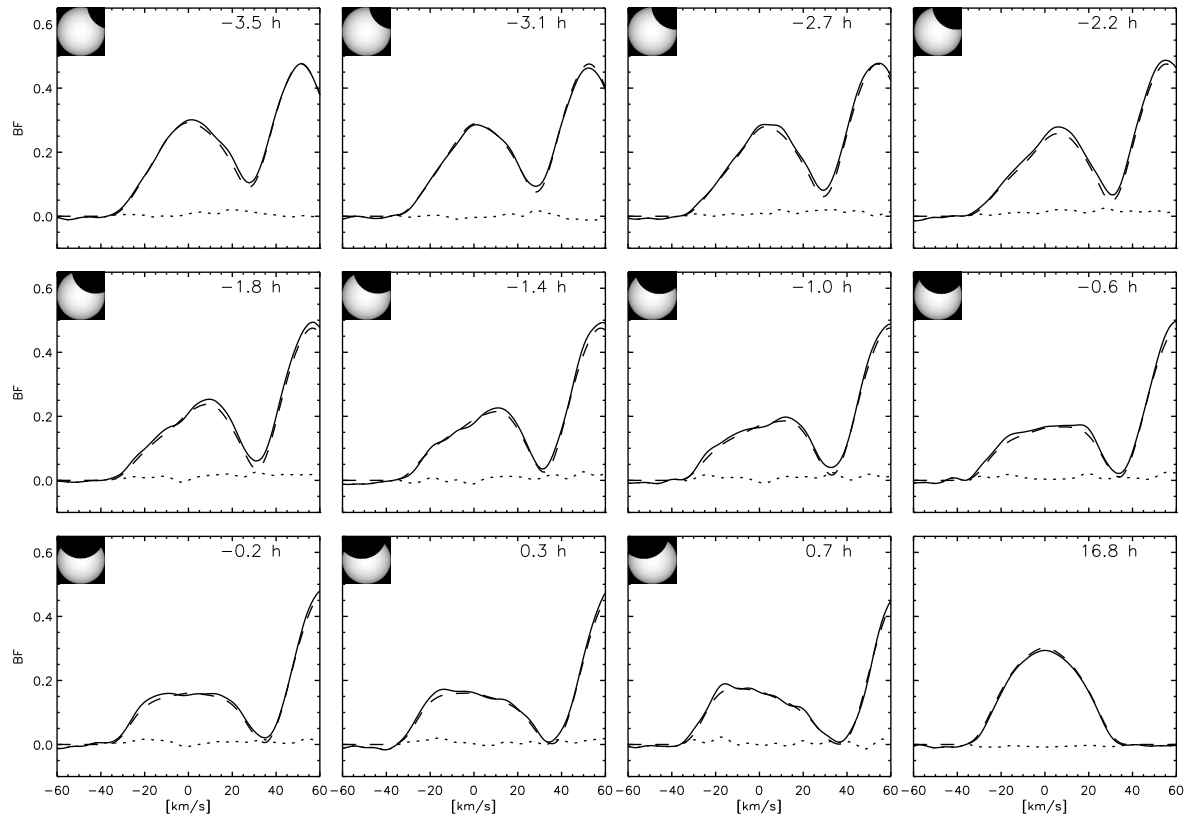

Figure 4.9 — The same as Fig. 4.8 but for the secondary eclipse. One can see that the BF of the primary moves further away from the secondary BF in velocity space over the course of the eclipse. The panel in the lower right corner shows the BF of the secondary for an observation out of eclipse.

rotation axes are normal to the orbital plane, and aligned with each other and the rotation axis of the system.

This leaves the theoretical prediction of the apsidal motion unaltered for V1143 Cyg. Hence, the difference between expected (0.00089 ± 0.00015 °/cycle) and measured apsidal motion (0.000705 ± 0.000041 °/cycle), which just lies outside the 1-σ error bars, is also unchanged. The effect of a misalignment between the stellar rotation axes and the orbital spin axis on the apsidal motion has been studied by Kopal (1978), Shakura (1985), Company et al. (1988), and Petrova & Orlov (2003). The contribution of the stellar rotation to the advance of the longitude of the periastron is reduced if the stellar rotation axis is tilted against the orbit spin axis until finally, when the axis of stellar rotation lays in the orbital plane, its contribution is half as large and with the opposite sign as when the stellar and orbital axes would be parallel. In this situation, it contributes to a retrograde rotation of the periastron. The contribution of the stellar rotation to the apsidal motion depends not only on the orientation of the axis, but also on the square of the angular stellar rotation rate. As one measures only $v \sin i$, a greater inclination towards the observer would mean a higher angular stellar rotation rate, and therefore a greater contribution of the rotation term to the overall apsidal motion. We derive that if the rotation axes of both stars would lie in the orbital plane, but have no inclination towards the

observer, then the complete apsidal motion would be 0.00073°/cycle. If the rotation axes would have an inclination towards the observer of $i \approx 70^\circ$ in either of the two stars, or of $i \approx 60^\circ$ in both stars, only then would the expected and measured apsidal motion be in agreement. The secondary, due to its higher $v \sin i$, has a larger influence on the rotational term of the apsidal motion than the primary component. As already pointed out, it is very unlikely that the stellar and orbital spin axes span a large angle, while their projections on the sky are, in their uncertainties, parallel. Our findings do not support the hypothesis advocated by Petrova & Orlov (2003), that a misalignment of the stellar rotation axes with the orbital spin could bring the theoretical and measured apsidal motion for a number of binary systems, including V1143 Cyg, into better agreement.

Our work has excluded the option of a misalignment between the stellar rotation axes as a possible explanation for the difference between the expected and measured apsidal motion in V1143 Cyg. It is therefore interesting to look at other possibilities that might explain this difference. As the apsidal motion constant (k_2) is an important source of uncertainty in the calculation of the expected apsidal motion, a new calculation of the apsidal motion constant for V1143 Cyg using modern codes for stellar evolution might be of value.

In our analysis of the orbital data we found no indication of a third body in the V1143 Cyg system, whose influence might also alter the apsidal motion. However, because of the limited coverage in time (one year) and the limited accuracy in radial-velocity, combined with the possibility that the orbit of a third body could have a lower inclination, a third body cannot be excluded.

The alignment of the stellar rotation axes could also set a lower limit to the age of the system, if the axes were not aligned at the birth of the system. However, this is not a straightforward argument, since, during the pre-main-sequence phase, synchronizing forces must have been larger, due to the larger sizes of the stars. Proper modeling of the evolution of V1143 Cyg might reveal whether it had enough time to align its axes. If the time-span to align the axes is longer than the lifetime of the system, it would mean that V1143 Cyg, with its high eccentricity of 0.54, was born in this way, with all spin and orbital axes aligned.

4.5 Conclusions

We measured the Rossiter – McLaughlin effect for both components in the binary system V1143 Cyg. We developed two different methods to derive the angle β between the stellar spin axis projected onto the plane of the sky and the orbital spin axis projected onto the plane of the sky.

Using the first method, i.e. by determination of the center of the broadening function, we showed how it is possible to subtract the absorption lines of the foreground star during an eclipse from the spectrum. This made it possible to use the shift of the center of gravity of the absorption lines as a proxy for the rotation effect, even in systems with blending occuring during eclipses, and derive values for β and $v \sin i$. However, for systems with low eccentricity, blending of the spectral lines during eclipses is stronger than in V1143 Cyg. Therefore, every systematic error in the tomography or in the subtraction of the foreground spectrum due to the parameters used in the subtraction, will have a substantial effect on the value of β derived.

The second method presented in this chapter, the modeling of the shape of the broadening

functions, avoids the problems of the first method by taking the influence of the eclipsing star into account explicitly. This makes the method more suitable for eclipsing binary systems with low eccentricity (higher blending of the spectral lines). The use of the complete BFs, instead of the center of gravity or the Gaussian fit to the line, has the additional advantage that it makes the fitting of the parameters β and $v \sin i$ more precise. However, the derived values for these parameters are not necessarily free of systematic errors. Further work is needed here to make it possible to derive information about velocity fields on the stellar surface represented by macro-turbulence, or differential rotation. If differential rotation is present it might be possible to derive some information about the inclination of the rotation axes towards the observer.

With both methods we determined orbital and stellar parameters which agree within their uncertainties with values derived in earlier studies, with the exception of the semi-amplitude of the secondary. The values derived for the angle β agree with each other. We found that the stellar rotation axes in V1143 Cyg are normal to the orbital plane for both components, which leaves the theoretical predictions for the apsidal motion unchanged. This makes V1143Cyg the first binary system with main-sequence stars for which the orientations of the rotation axes of both components are determined.

Even with progress made in the field of apsidal motion in the last years (e.g. Claret & Willems 2002), it is interesting to apply the methods discussed here to other binary systems where there is a stronger disagreement between the observed and expected apsidal motion (e.g. DI Herculis, Claret 1998), in order to investigate whether a misalignment of the stellar rotation axes can be excluded as a cause for the disagreement, or wether a misalignment contributes to the difference. Furthermore, information about the orientation of the stellar rotation axes in binary systems could be used to explore the dependence of the synchronization time scales on the semi-major axis, eccentricity of the binary system and the stellar type of its components. This might lead to new insight about the formation and evolution of binary systems and stellar interiors.

Acknowledgments

We kindly thank Saskia Hekker for taking some of the observations used in this study, as well as the staff at the Lick Observatory for their excellent support during the observations. We would also like to thank Craig Markwardt for the use of routines taken from his web page at http://cow.physics.wisc.edu/~craigm/idl/idl.html. This research has made use of the Simbad database located at http://simbad.u-strasbg.fr/ and the Vienna Atomic Line database (VALD) located at http://ams.astro.univie.ac.at/vald/.

4.6 Data

Table 4.3 — Radial velocity measurements of V1143 Cyg out of eclipse and during the primary and secondary eclipse. The photon midpoints of the observations are given in the first column, while the radial velocities of the primary and secondary are given in the second and third row.

HJD	Vel. P	Vel. S
[JD-2400000]	[km/s]	[km/s]
53612.665	35.40±0.13	−81.71±0.22
53612.683	30.58±0.14	−76.43±0.23
53651.654	−71.40±0.14	27.82±0.22
53613.663	−76.90±0.14	33.40±0.23
53613.771	−78.44±0.14	34.56±0.22
53613.880	−79.27±0.14	35.48±0.23
53934.843	−79.49±0.14	35.83±0.23
53583.676	−78.86±0.14	35.39±0.23
53936.818	−57.40±0.13	13.47±0.22
53585.669	−51.69±0.15	6.91±0.25
53649.639	43.23±0.14	−89.43±0.23
53611.709	62.33±0.14	−109.40±0.23
53611.728	63.65±0.14	−111.21±0.24
53611.814	70.69±0.13	−117.65±0.22
53611.835	72.30±0.14	−119.47±0.23
53611.884	76.29±0.14	−123.12±0.23
53611.903	77.69±0.13	−125.03±0.22
53932.846	80.45±0.13	−127.61±0.22
53581.675	96.71±0.14	−144.12±0.24
53650.612	88.17±0.14	−135.32±0.23
53650.737	67.50±0.14	−113.86±0.22
53612.865	−12.10±0.18	−33.23±0.27
53612.884	−15.74±0.19	−29.58±0.28
53612.901	−19.29±0.18	−26.26±0.28
53612.919	−22.44±0.18	−22.26±0.27
53579.678	−11.09±0.18	−33.60±0.28
53612.701	27.01±0.20	
53612.719	24.88±0.20	
53612.737	22.93±0.20	
53612.757	18.28±0.20	
53612.775	6.63±0.20	
53612.793	−2.84±0.20	
53612.811	−5.44±0.20	

continued on next page

Table 4.3 — Radial velocity measurements of V1143 Cyg

HJD	Vel. P	Vel. S
[JD-2400000]	[km/s]	[km/s]
53612.829	−6.75±0.20	
53612.847	−8.71±0.20	
53587.717		−46.88±0.32
53587.732		−46.88±0.32
53587.748		−46.85±0.32
53587.767		−47.20±0.32
53587.782		−47.74±0.32
53587.798		−48.19±0.32
53587.816		−50.23±0.32
53587.832		−52.14±0.32
53587.848		−53.93±0.32
53587.866		−56.31±0.32
53587.882		−57.96±0.32

Bibliography

Andersen, J., Nordstrom, B., Garcia, J. M., & Giménez, A. 1987, A&A, 174, 107 62, 63, 67, 71, 72

Bagnuolo, Jr., W. G. & Gies, D. R. 1991, ApJ, 376, 266 67

Balthasar, H. 1988, A&AS, 72, 473 73

Claret, A. 1998, A&A, 330, 533 77

Claret, A. & Willems, B. 2002, A&A, 388, 518 77

Company, R., Portilla, M., & Gimenez, A. 1988, ApJ, 335, 962 75

Giménez, A. 2006, ApJ, 650, 408 62

Giménez, A. & Margrave, T. E. 1985, AJ, 90, 358 62, 63, 67, 71, 72

Gray, D. F. 2005, The Observation and Analysis of Stellar Photospheres (The Observation and Analysis of Stellar Photospheres, 3rd Edition, by D.F. Gray. ISBN 0521851866. Cambridge, UK: Cambridge University Press, 2005.) 69, 72, 73

Hadrava, P. 2007, in ASP Conference Series, Vol. 370, Solar and Stellar Physics Through Eclipses, ed. O. Demircan, S. O. Selam, & B. Albayrak, 164 73

Hipparcos. 1997, ESA SP-1200 62

Hosokawa, Y. 1953, PASJ, 5, 88 62, 67

Hube, D. P. & Couch, J. S. 1982, Ap&SS, 81, 357 62

Kopal, Z. 1959, Close binary systems (The International Astrophysics Series, London: Chapman & Hall, 1959) 62, 67

Kopal, Z., ed. 1978, Astrophysics and Space Science Library, Vol. 68, Dynamics of Close Binary Systems 75

McLaughlin, D. B. 1924, ApJ, 60, 22 62

Ohta, Y., Taruya, A., & Suto, Y. 2005, ApJ, 622, 1118 62

Petrova, A. V. & Orlov, V. V. 2003, Astrophysics, 46, 329 75, 76
Pierce, A. K. & Slaughter, C. 1982, ApJS, 48, 73 73
Press, W. H., Teukolsky, S. A., Vetterling, W. T., & Flannery, B. P. 1992, Numerical recipes in FORTRAN. The art of scientific computing (Cambridge: University Press, |c1992, 2nd ed.) 65, 70
Queloz, D., Eggenberger, A., Mayor, M., et al. 2000, A&A, 359, L13 62
Rossiter, R. A. 1924, ApJ, 60, 15 62
Rucinski, S. 1999, in ASP Conf. Ser. 185: IAU Colloq. 170: Precise Stellar Radial Velocities, ed. J. B. Hearnshaw & C. D. Scarfe, 82 65
Shakura, N. I. 1985, Soviet Astronomy Letters, 11, 224 75
Snellen, I. A. G. 2004, MNRAS, 353, L1 62
Takeda, Y. 1995, PASJ, 47, 337 73
Udry, S., Mayor, M., Maurice, E., et al. 1999, in ASP Conference Series: IAU Colloq. 170: Precise Stellar Radial Velocities, ed. J. B. Hearnshaw & C. D. Scarfe, Vol. 185, 383 65, 72
Winn, J. N., Johnson, J. A., Marcy, G. W., et al. 2006, ApJ, 653, L69 62
Worek, T. F. 1996, PASP, 108, 962 62

Chapter 5

Misaligned spin axes in the DI Herculis system

DI Herculis is one of the most interesting young eclipsing binary systems known. Its apsidal motion, the rotation of the orbit in its own plane, has been measured to be significantly lower ($2.9 \times 10^{-4} \pm 0.4 \cdot 10^{-4}$ °/cycle) than the expected value ($1.25 \cdot 10^{-3}$ °/cycle). Until now the reason why its apsidal motion is much slower than theoretically expected escapes a solid explanation. A number of theories have been put forward to explain this apparent discrepancy, including a revision of general relativity.

However the underlying calculations are based on the premise of co-aligned stellar rotation axes. To test this assumption we observed the DI Herculis system during both primary and secondary eclipse with the high resolution Echelle spectrograph Sophie of the Oberservatorie de Haute Provence.

Using our newly developed analysis tools (Chapter 4) we find a strong misalignment between the projections of the stellar spin axes and the orbital spin axis on the sky. The angle between, the projected stellar spin axes and the projected orbital spin axis is ($71 \pm 4°$) for the primary and ($93 \pm 8°$) for the secondary. This is the first time that such a strong degree of misalignment between the different spin axes in a close binary system has been demonstrated.

The observed misalignment has two immediate consequences. 1) The expected apsidal motion for this system is reduced to ($4.9 \cdot 10^{-4}$ °/cycle). As we are not sensitive to a possible inclination of the stellar spin axes, the calculated value represents an upper limit for the expected apsidal motion. Allowing for a moderate amount of inclination ($\sim 30°$), with respect to the line of sight, of both stellar axes the measured and expected apsidal motion are in perfect agreement. 2) So far most studies of binary formation and evolution, theoretical and observational, assume co-aligned spin axes in close systems. This assumption might not always be true, and as demonstrated for DI Herculis, can have important consequences for the evolution of the system. Finally, we shortly discuss possible ways towards strong misalignment of stellar spin axes.

S. Albrecht, S. Reffert, I.A.G. Snellen, J. N. Winn, R. N. Tubbs & A. Giménez
in preparation

5.1 Introduction

DI Herculis (spectral type B4 V and B5 V, P = 10.55 d, e = 0.49) is one of the most fascinating eclipsing binaries systems known. The most striking feature of the DI Herculis system is the much lower measured apsidal motion rate than expected and the lack of a convincing explanation for this (Guinan & Maloney 1985; Claret 1998). The apsidal motion describes the precession of the orbit in its own plane, i.e. the change of the argument of the periastron (ω) over time. It is caused by both a general relativistic effect and a Newtonian contribution, the latter consisting of two terms which are due to the deformation of the two stars by tidal forces and stellar rotation. The expected apsidal motion for DI Herculis is 0.00125°/cycle (Claret 1998), including the apsidal motion due to the Newtonian term (0.00056°/cycle) and that caused by the general relativity term (0.000676°/cycle; Company et al. 1988). This value for the expected apsidal motion is in strong contrast to the measured value of the apsidal motion (0.00029±0.000043°/cycle) found by Guinan et al. (1994). Even the relativistic term alone is greater than the measured value.

Historically, also for a number of other eclipsing binary systems a discrepancy between the theoretical and measured apsidal motion has existed, but thanks to new observations and new stellar evolution codes, these discrepancies have been reduced and the expected and measured apsidal motion rates for these systems are now in good agreement (Claret & Gimenez 1993; Claret & Willems 2002). However, for DI Herculis this is not the case. A number of different scenarios have been suggested to explain this discrepancy (See Guinan & Maloney 1985; Claret 1998, for a summary.). For example a modification to the theory of gravity was suggested. Also a third companion of smaller mass could alter the apsidal motion rate. However none of the explanations are satisfactory as they are, at the moment, very difficult to prove or reject. For example searches for a low mass star or massive planetary object around the bright early type stars are very difficult to conduct and so far have neither excluded this possibility nor found candidates (Guinan & Maloney 1985; Marshall et al. 1995).

There is however one suggested mechanism which could reduce the apsidal motion that we can test. A misalignment between the stellar rotation axes and the orbital spin axis would reduce the apsidal motion. The impact of misaligned stellar spin axes on apsidal motion has been studied for different systems by different authors (e.g. Kopal 1978; Shakura 1985; Company et al. 1988; Petrova & Orlov 2003). For the case of DI Herculis it was found that a strong misalignment could indeed be sufficient to account for the difference between the expected and measured apsidal motion rates. As every close binary system, also DI Herculis experiences synchronization forces. DI Herculis is however a very young system ($5 \cdot 10^6$ years) and the time scale for alignment is 20 time greater than its age (Claret 1998). Therefore one would find inclined rotation axes, if they were initially inclined.

Unfortunately, it is not straight forward to measure the orientation of the stellar rotation axes for all but a few stars, as nearly all stars are unresolved and the telescope integrates the light from the complete stellar surface. Thus only the radially-projected rotational velocity $v \sin i$ can be measured. During eclipses, however varying parts of the stellar disk are obscured, allowing the observer to gather spatially resolved information. The crossing of a companion in front of a rotating star causes a change in the line profile of the eclipsed star. This rotation or Rossiter-

Table 5.1 — Parameters for DI Herculis DI Herculis taken from Hipparcos (1997)‡ and Guinan & Maloney (1985)†. Radius$_p$ denotes the radius of the primary component and Radius$_s$ the radius of the secondary component. The masses and effective temperatures of the components are denoted by Mass$_i$ and T$_{\mathrm{eff}\,i}$, respectively.

HIP	92708	
HD	175227	
R.A.$_{\mathrm{J2000}}$	$18^{\mathrm{h}}53^{\mathrm{m}}26^{\mathrm{s}}$	‡
Dec.$_{\mathrm{J2000}}$	$24^{\circ}16'41''$	‡
Vmax	8.45 mag	‡
Sp. Type	B 4/5 V	†
Period	$10\overset{\mathrm{d}}{.}550164(1)$	†
Radius$_p$	$2.68(5)R_{\odot}$	†
Radius$_s$	$2.48(5)R_{\odot}$	†
Mass$_p$	$5.15(10)M_{\odot}$	†
Mass$_s$	$4.52(6)M_{\odot}$	†
T$_{\mathrm{eff}\,p}$	17 000(800) K	†
T$_{\mathrm{eff}\,s}$	15 100(800) K	†

McLaughlin (RM) effect was first observed by Rossiter (1924) in β Lyrae, and by McLaughlin (1924) in the Algol system. Due to the Doppler effect, light emitted from the side of the stellar disk that moves towards the observer is blue-shifted and light emitted from the receding side is red-shifted. When the red-shifted (receding) part of the disk is blocked, the net starlight looks slightly blue-shifted, and vice versa. If the spin axis of the eclipsed star is aligned with the orbital axis, first blue-shifted light and later, to the same amount, red-shifted light is blocked. For a misaligned axis this is not true, and red-shifted and blue-shifted light is blocked at different times and to different amounts. We developed two methods to accurately determine the alignment of stellar rotation axes in double lined eclipsing binaries. (See Chapter 4). Recently the RM-effect has been used to determine the relative orientation of the spin axes of exoplanet host stars (see for example Winn et al. 2005). The RM-effect might also be used to probe atmospheres of transiting exoplanets Snellen (2004).

We observed DI Herculis at the Observatoire de Haute Provence (OHP) during the primary and secondary eclipses and out of eclipse to measure the relative orientation of the stellar spin axes. This way we either confirm that tilted rotation axes are responsible for the difference between the theoretical and measured apsidal motion or to exclude this possibility form the list of possible explanations. In the next section we present our data. This is followed by the description of our analysis and results in Section 5.3. In Section 5.4 we describe the implications of our results followed by our conclusion.

5.2 Data

We observed the DI Herculis system using the high resolution Echelle spectrograph Sophie at the 1.93 m telescope of the OHP during the secondary eclipse in the night 30.06 – 01.07.2008 where mid-eclipse occurs at $\sim 23:00$ UT. The total duration of the secondary eclipse is $\sim$ 7 hours. Unfortunately, we lost the first few hours of the night due to technical problems. We therefore covered only the mid to second half of the secondary eclipse. The primary eclipse

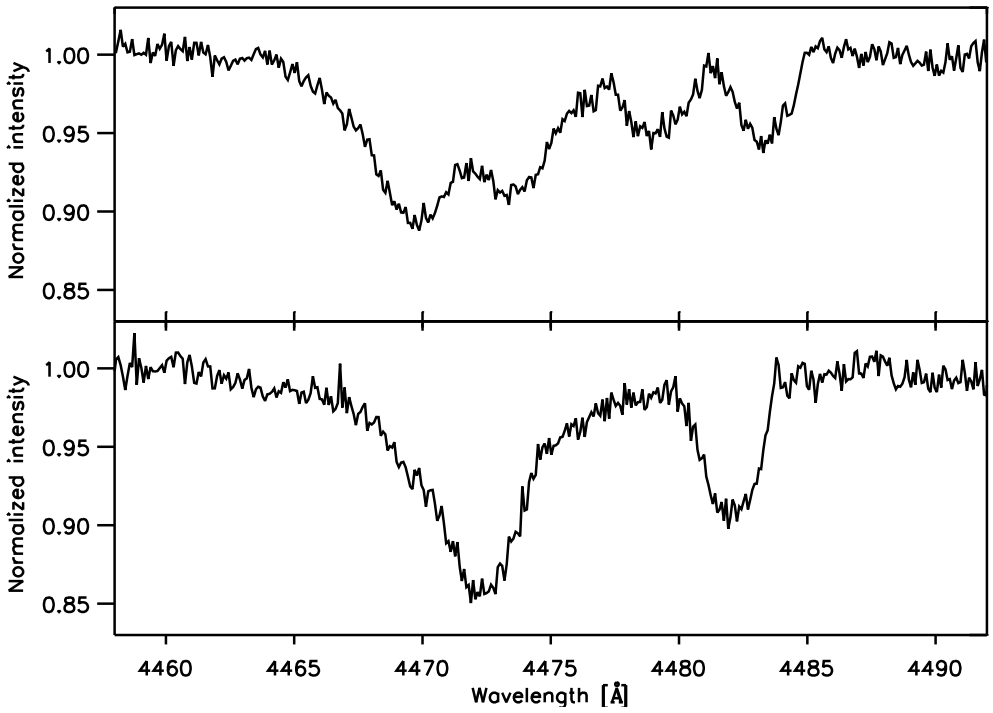

Figure 5.1 — The upper panel displays a normalized spectrum around the He I and Mg II lines of DI Herculis. It was obtained at a orbital phase (0.07) when the components have high radial-velocities relative to each other. The absorption lines of the two stars are well separated. Note the broad 'wings' of the He I line (~ 4471 Å), which is due to pressure broadening. The lower panel displays a spectrum obtained 0.1 hours before mid-point of the secondary eclipse. The received light originated nearly completely from the foreground primary.

was observed in the night 13 – 14.07.2008. Mid-eclipse occurred at $\sim 22:40$ UT. As the primary eclipse has a total duration of $11\,1/2$ hours, it can therefore not be covered in one night. We therefore had additional observations planned for the night of the 20.05.2006. Due to bad weather only one observation directly before the beginning and two in the first half of the primary eclipse were conducted. In addition eight observations out of eclipse have been obtained.

We used the High Efficiency (HE) mode of Sophie which offers a high throughput and a spectral resolution of R$\sim 40\,000$. One fibre was pointed towards DI Herculis while the second fibre was exposed to the sky. We chose an integration time of 20 min for observations during eclipses, and 15 min integration time for observations outside the eclipses. Less than one minute after the shutter was closed science grade spectra had been produced by the instrument and its software. For our further analysis we used the 2D-spectra delivered by the software.

5.3 Results

For our analysis of the RM-effect we focused on the Mg II line at 4481 Å . We chose this line as it is relatively deep in the spectra of both stars, and it is mainly broadened by stellar rotation. It

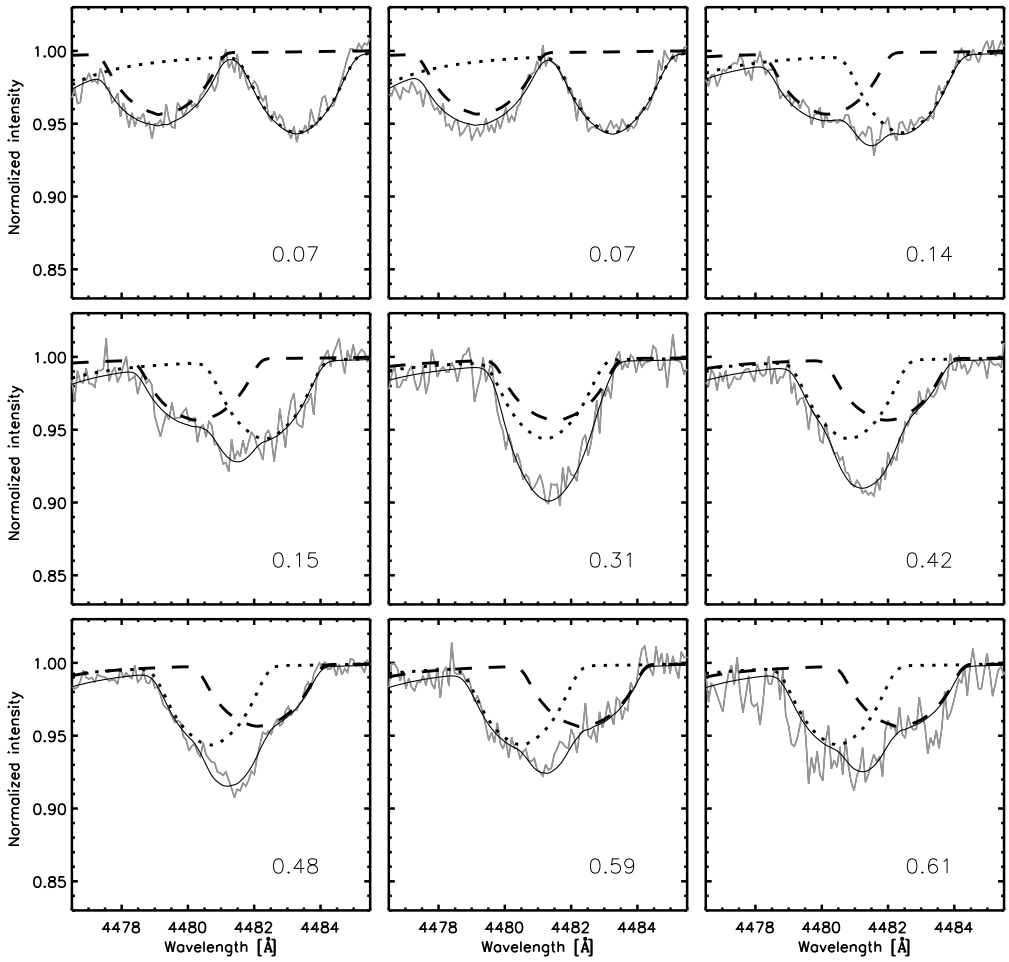

Figure 5.2 — Normalized spectra around the Mg II line at 4481 Å of DI Herculis obtained out of eclipses. Each panel shows one observation. The gray line represents the measured spectrum, while the solid line shows our best fit. The dotted line shows the contribution of the primary and the dashed line the contribution of the secondary. The numbers in the lower right corner of each panel indicate the phase of the system at the time of the observation. Note that the two observations at an orbital phase of 0.07 have been obtained at different nights.

is located in the 'red' wing of the He I line at 4471 Å. We therefore also included this, mainly pressure broadened line, into our analysis. Both lines are, in our setup, located approximately in the middle of order nr. 11 on the Sophie CCD. See Figure 5.1 for two spectra centered on these two lines.

Normalization is the first, and at the same time, one of the most critical parts of our analysis. We used, for initial normalization, the flat-fields delivered by the software of the instrument. In a second step we corrected for the residuals by fitting a third order polynomial to the remaining curvature in the science spectra. Here we excluded the wavelength regions influenced by the He I and Mg II lines. Finally we divided the science spectra by this polynomial, extrapolated over the wavelength region of the two lines of interest. In addition we corrected for bad-pixels.

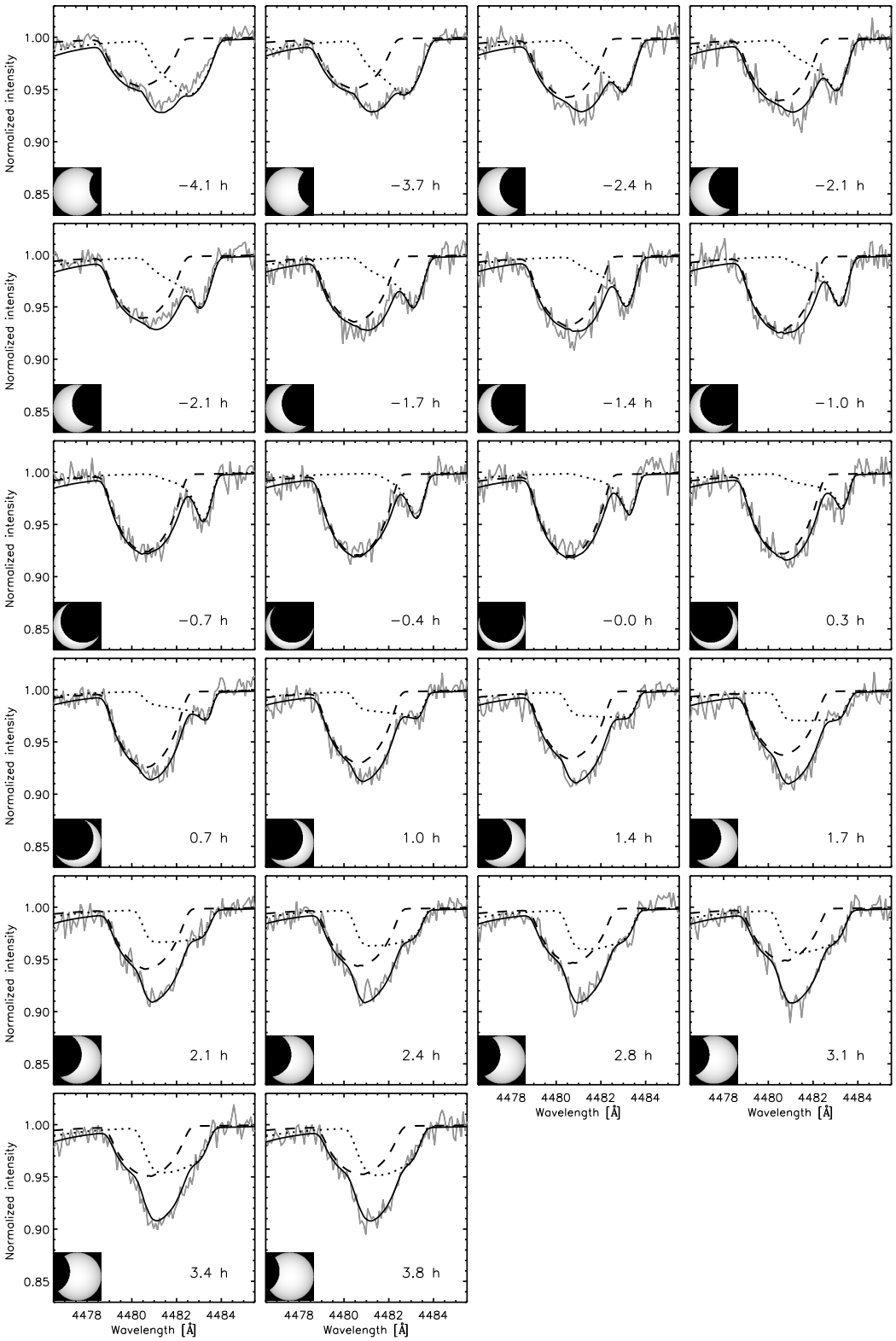

Figure 5.3 — The same as for Figure 5.2, but this time for observations during the primary eclipse. The numbers in the lower right corner of each panel indicate the time difference between the midpoint of the observation and the midpoint of the primary eclipse in hours. In the lower left corner one can see the uncovered part of the primary half-sphere for the midpoint of that measurement. The projected angle between the spin axis of the primary and the orbital axis is 71° for our best fitting model shown here.

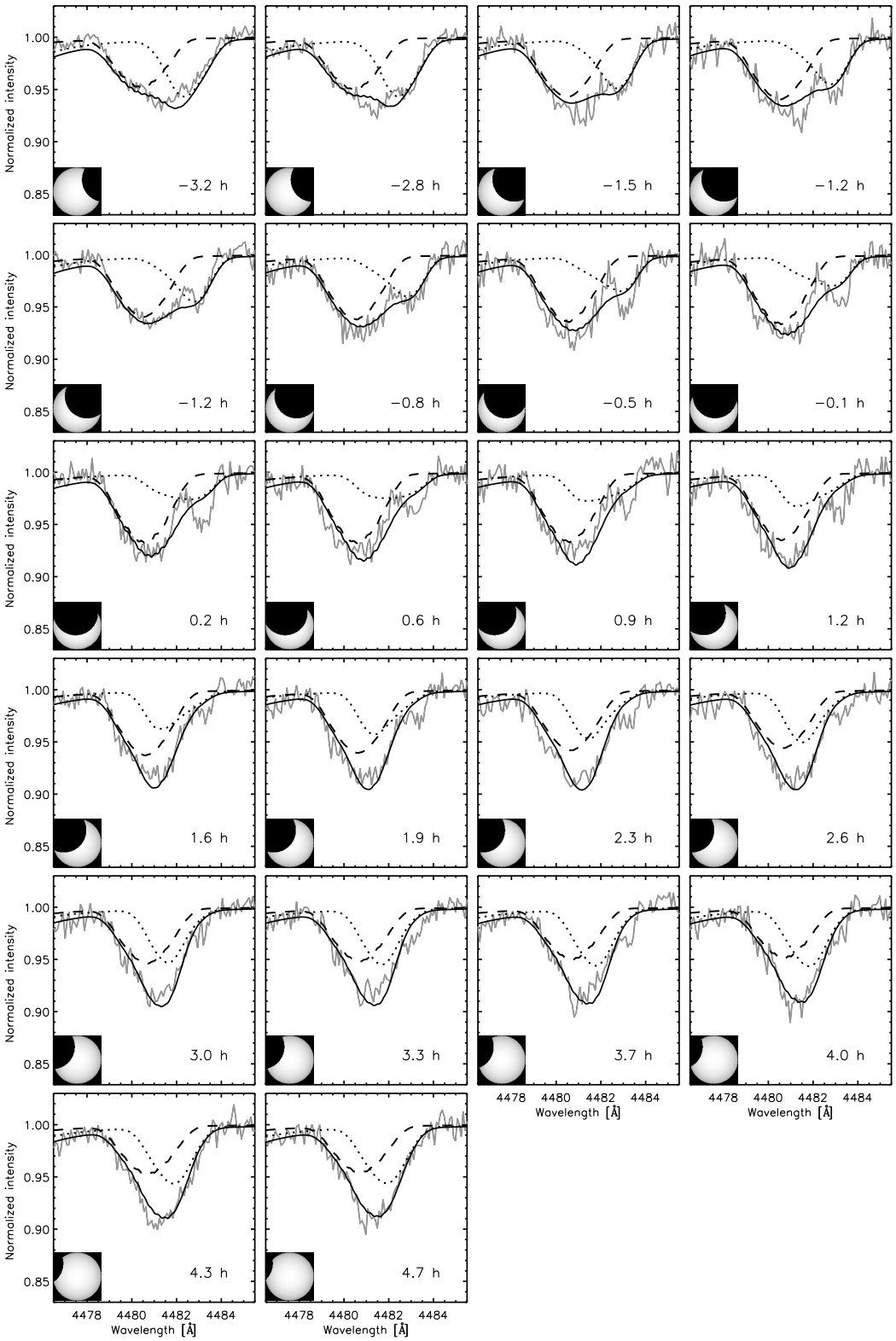

Figure 5.4 — The same as for Figure 5.3, but this time for our best fitting model with parallel spin axes in the DI Herculis system ($\beta \equiv 0°$). Note the disagreement between the model and the measured spectra in the spectral region which is dominated by the primary.

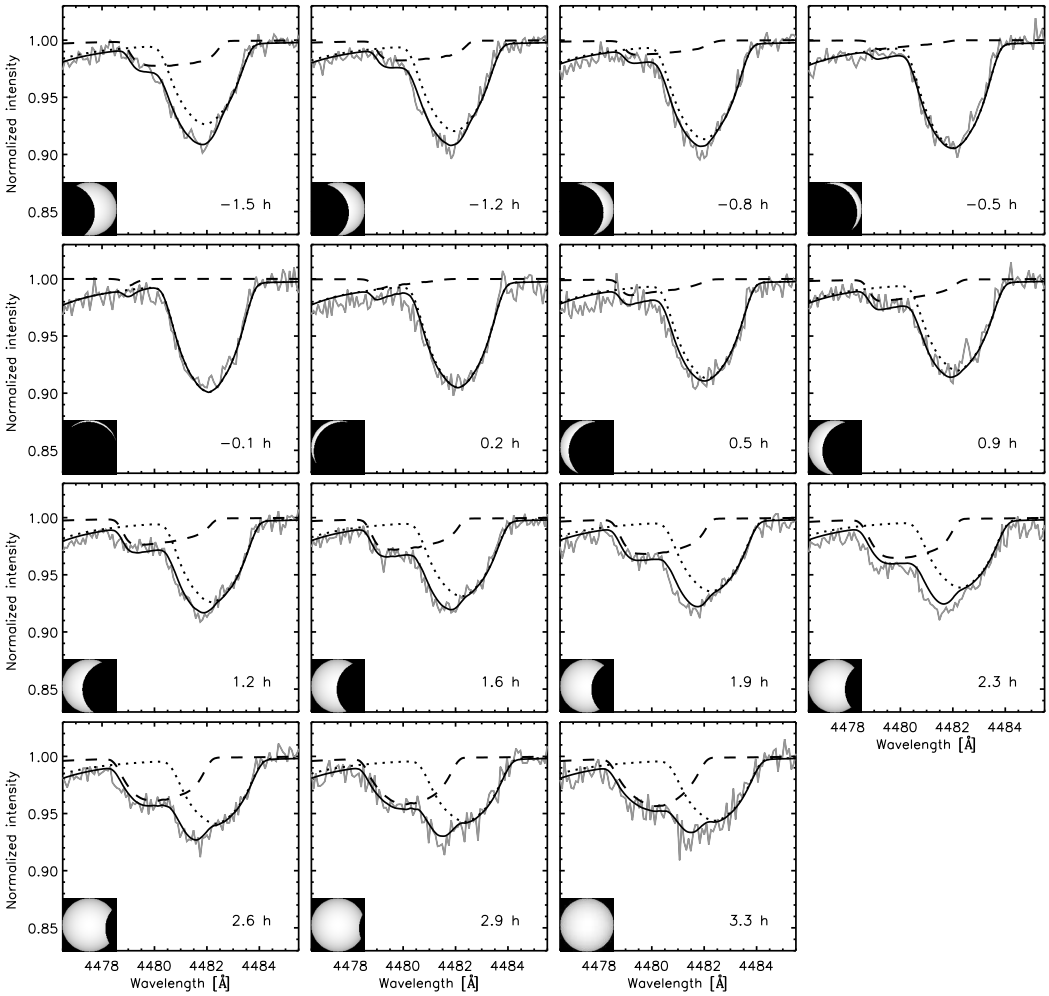

Figure 5.5 — The same as for Figure 5.3, but this time for observations during the secondary eclipse. The projected angle between the spin axis of the secondary and the orbital axis is 93° for the best model while a degeneracy exists with a second minimum at −88° (See Section 5.4.1).

The uncertainty in the wavelength solution of the spectrograph is very low and negligible for our purposes.

For the analysis of the RM-effect we use our approach developed in Chapter 4, which we shortly summarize here. The main difficulty in the interpretation of the RM-effect in double star systems is in the fact, that one does not only receive light from the eclipsed background star, which is the light one is interested in, but also from the eclipsing foreground star. For a double star system consisting of components of the same spectral type that means that one actually receives more light from the foreground star than from the eclipsed background star. In Chapter 4 we developed two methods to analyze the RM-effect despite this difficulty. In our first approach (Section 4.3.1) we extract from each obtained spectrum during its eclipse the contribution of the foreground star. To do this we first disentangle the spectra of the two components by using the tomography algorithm developed by Bagnuolo & Gies (1991), all observations obtained out of eclipse, and an orbital model of the binary system. We then derive

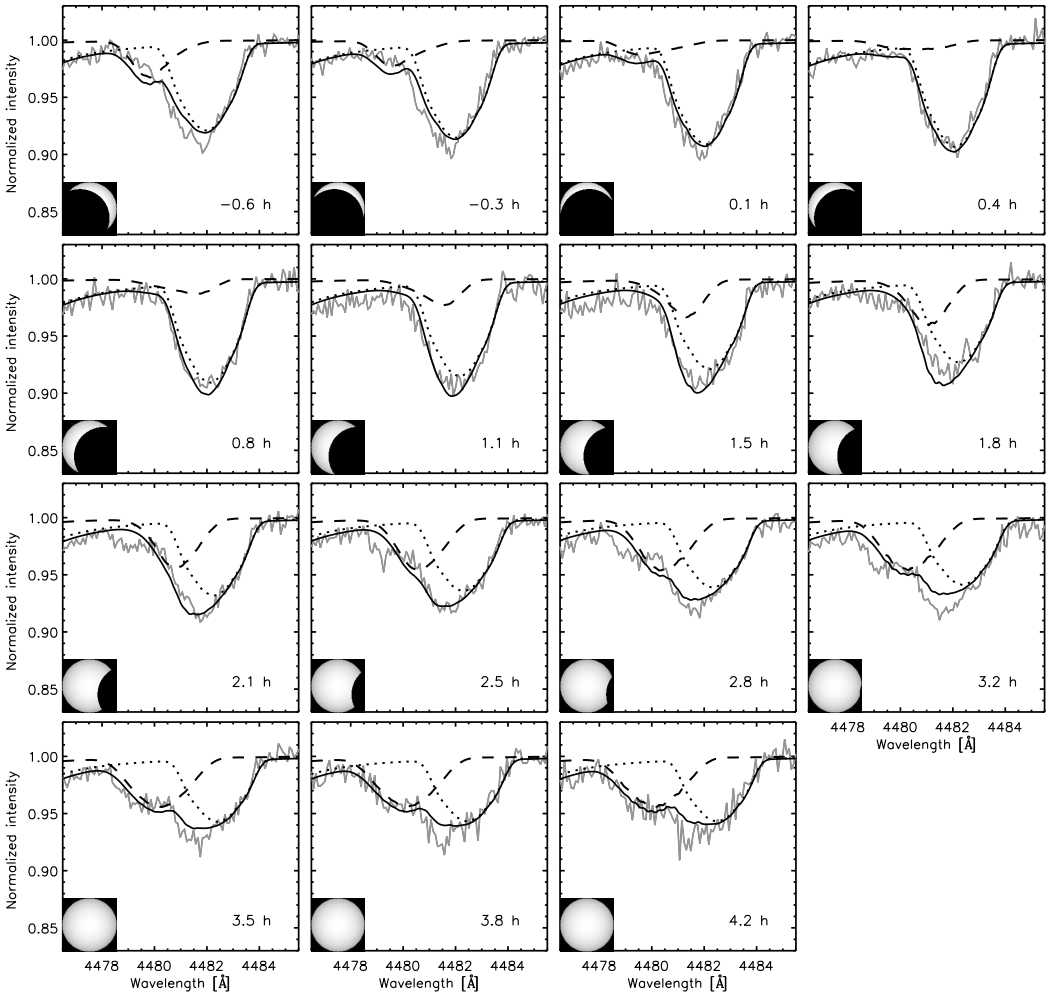

Figure 5.6 — The same as for Figure 5.4. Our best fitting model with parallel spin axes in the DI Herculis system ($\beta \equiv 0°$) is displayed along the observed spectra, but this time for the secondary eclipse.

the parameters which governs the RM-effect by measuring the shift of the center of gravity of the absorption lines of the eclipsed star. In our second approach (section 4.3.2) we simulate the absorption lines of both stars – out of the eclipses and during both eclipses – and derive the best fitting orbital and stellar parameters by comparing our model to the measured spectra. As it turned out, our second method delivers more accurate and precise results (see section 4.4) and since we have only a relative small number of out of eclipse observations of the DI Herculis system, we use only the second method in this chapter.

We fitted the spectra of the two stars in the DI Herculis system during and out of eclipses leaving the following orbital parameters free: the period (P), the time of primary minimum (T_{minI}), the eccentricity (e), the argument of periastron (ω) the orbital inclination (i), and the semi-amplitudes of the two stars (K_i). Furthermore the luminosity ratio at ~ 4500 Å between the two stars enters the fit as a free parameter (L_s/L_p). For each star we have four additional free parameters: The first parameter describes the projected rotational velocity ($v \sin i$). The second parameter, the Gaussian width of the macro-turbulence (ζ_{RT}), describes the the strength

of velocity fields on the stellar surface (Gray 2005). We kept the σ of the Gaussians for the tangential and radial velocity fields and their covered surface fraction equal. Another stellar parameter describes the degree of pressure broadening for the He I lines. The angle between the stellar spin axis and the orbital spin axis, projected onto the plane of the sky, β, is the fourth parameter. A projected rotation axis perpendicular to the orbital plane would mean $\beta = 0°$, whereas $\beta = 90°$ would indicate that the rotation axis lies in the orbital plane. The longitude of the ascending node of the orbit (Ω) is not known, resulting in an ambiguity in the sign of the angle β. In our definition, a positive β indicates that the RM-effect, integrated over the complete eclipse, would give a positive residual in radial-velocity, for an exactly edge-on orbit. The companion passes over a larger stellar surface area which is moving towards the observer than over surface area which is moving away from us. Two additional free parameters are needed, one which weights the relative depth of the simulated He I and Mg II lines, and another which describes the total depth of the stellar lines in the spectrum.

Next to these 18 free parameters we adopted a number of parameters from the literature for our model and kept these fixed: We describe the limb darkening of both stars using a linear limb darkening law and with the limb darkening coefficient $u = 0.4$ at ~ 4500 Å (Gray 2005). We further adapted the radii of the two stars from Guinan & Maloney (1985) displayed in Table 5.1. Finally we did not allow for solar-like differential rotation $\alpha = 0$.

We used the Levenberg-Marquardt least-squares minimization algorithm to derive the best fitting parameters and the bootstrap method (Press et al. 1992) to derive the $1-\sigma$ uncertainties in the parameters. Our best fitting parameters are displayed in the first column of Table 5.2, along with literature values for the orbital and some stellar parameters in the second column. Note that we find that the rotation-axes of both stars are tilted against each other and with respect to the orbital spin (i.e. $\beta_i \neq 0$). Note that the literature value for ω (329.9°) obtained from Popper (1982) is brought forward to the year 2008 including an apsidal motion rate of 1.04°/100 years as determined by Guinan et al. (1994). Figure 5.2 displays the spectra around the Mg II line at 4481 Å for all observations out of eclipse (gray lines). Furthermore we indicate our best fitting model for absorption lines of the primary (dotted lines) and secondary (dashed lines) and their combined contribution (solid lines). Figure 5.3 shows the same for our observations during primary eclipse, and Figure 5.5 displays data obtained during secondary eclipse along with the model. All figures show spectra which for clarity have been spectrally binned by four pixels. The fits, however, have been performed with the original resolution. The radial velocities of our orbital model and the orbital plane of DI Herculis are displayed in Figure 5.8.

We further tried to fit our data using the same model but this time with the β_i for both stars set to 0. This would mean that the projections of all axes in this system are parallel. The results of this fit are displayed in the third column of Table 5.2 and in Figure 5.4 and Figure 5.6.

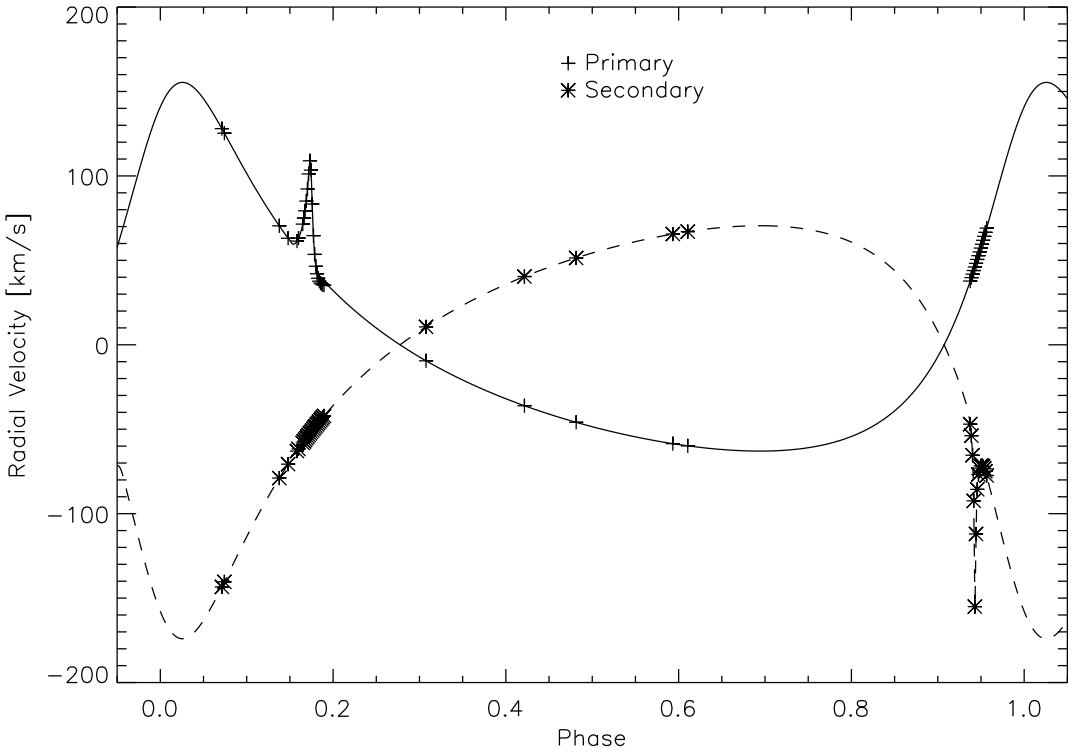

Figure 5.7 — The radial-velocity solution for the primary (solid line) and secondary (dashed line) components of DI Herculis is plotted against orbital phase. The crosses and stars indicate the radial-velocities of the stars at the times of the observations according to our best fitting model (they do not indicate radial-velocity measurements). The midpoint of the primary eclipse occurs at a phase of ~ 0.17, and the midpoint of the secondary eclipse occurs at a phase of ~ 0.94. Note that the systemic velocity is not shown in this graph.

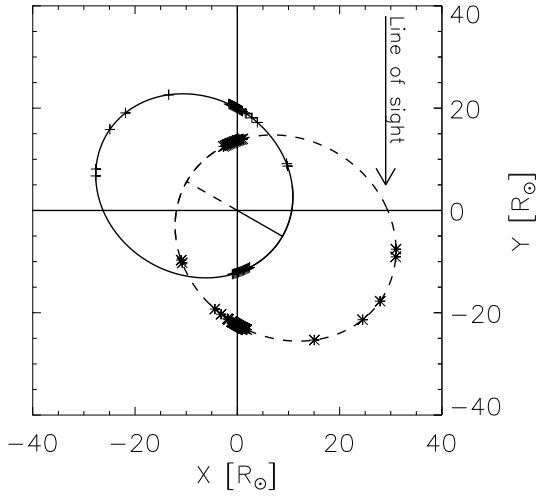

Figure 5.8 — A polar view of the orbit of the binary system DI Herculis. The solid line represents the orbit of the primary component and the dashed line the orbit of the secondary. The lines from the center of gravity towards the orbits indicate the periastron. The crosses and stars indicate the positions of the stars during observations.

Table 5.2 — Derived parameters for the DI Herculis system and its components are shown together with their formal errors derived using the bootstrap method. The second column shows our best fit parameters. For comparison, values given by Popper (1982) and Guinan & Maloney (1985) are shown in the third column, while the fourth column shows the derived parameters with the assumption of aligned spin axes $\beta_i \equiv 0°$. See Section 5.4 for a further discussion about the uncertainties of the best fitting parameters.

Parameter	Best fit	Popper (1982)† Guinan & Maloney (1985)⋆	Parallel axes $\beta_i \equiv 0°$
T_{minI} [JD-2400000]	42233.36±0.05	42233.3481±0.0007⋆	42233.36±0.05
P [days]	10.55017±0.00004	10.550164±0.000001⋆	10.55015±0.00005
e	0.487±0.003	0.489±0.003†	0.487±0.004
ω [°]	330.6±0.6	330.2±0.6†	330.4±0.9
i [°]	89.28±0.05	89.3±0.03⋆	88.16±0.14
$a \sin i$ [$R_\odot$]	42.3±0.6	43.18±0.24†	43.7±1.0
K_p [km/s]	109.6±2.1	110.7±0.5†	114.2±3.4
K_s [km/s]	123.0±2.0	126.6±1.2†	126.9±3.5
γ_1 [km/s]	9.1±2.5	8.5±0.3	9.2±2.3
γ_2 [km/s]	$= \gamma_1$	9.1±0.3	$= \gamma_1$
$v \sin i_p$ [km/s]	105±1		102.7±2.2
$v \sin i_s$ [km/s]	116±2		111.8±2.5
$\zeta_{RT} P$ [km/s]	13±2		12±2
$\zeta_{RT} S$ [km/s]	10±1		23±2
β_p[°]	71±2		0 (fixed)
β_s[°]	93±4		0 (fixed)

5.4 Discussion

5.4.1 Robustness of the results

How robust are the derived parameters for the stars in the DI Herculis system? The biggest uncertainty in our results comes from the imperfection of the normalization of the spectra. This can be seen in the panels displaying the observations obtained during the primary eclipse (Figure 5.3). The two left panels in the two top rows have been obtained during different nights than the rest of the observations during the primary eclipse. One can see that there is an offset between the model and the spectra. It is difficult to quantify the error introduced by this imperfection in the normalization as most observations during primary eclipse, and all observations during the secondary eclipse, have been obtained during one night each. Under this condition it is not possible for the bootstrap method to derive reliable uncertainties. We estimate that the stated uncertainties listed in Table 5.2 underestimate the real uncertainties by a factor ~ 2 for each parameter. There are a few methods with which the normalization of the spectra can be improved. On of these is used, in a different context, in Chapter 6 of this thesis and applying it here will be an immediate improvement to our analysis.

A second challenge lies in our incomplete coverage of the orbit (see Figure 5.8). In particular we miss, due to bad weather, observations at orbital phases where the components have high radial velocities. One can expect that this influences the derived values for the semi-amplitudes of the radial-velocities most. Indeed for our best fit we derive orbital parameters which are, with the exception of the semi-amplitude of the secondary K_s, consistent with values found over 20 years ago by Popper (1982) and Guinan & Maloney (1985). We estimate that our real uncertainties in the semi-amplitudes is $\sim 5\,\mathrm{km\ s^{-1}}$. The other orbital parameters are however not as much affected by this problem of orbital coverage, as their uncertainty is more a function of the coverage of the eclipses which actually have been covered fairly well.

How do the reduced accuracies in the semi-amplitudes of the radial-velocities influence our results for the relative orientations of the stellar spin axes, β_i? The case for the DI Herculis system is in this respect more fortunate than that for the V1143 Cyg system, where the orbital velocity of the components was an order of magnitude greater than the projected rotational velocities, and changed rapidly during eclipses, compared to the $v \sin i$ of the components. Therefore small systematics in the orbital solution would have strongly influenced the derived values for the spin axes in the V1143 Cyg. This is not the case for DI Herculis. The nearly edge-on orientation of the DI Herculis system does however introduce a degeneracy in the derived values for β of the secondary as we find that its axis is nearly in the orbital plane. It is therefore very difficult to decide if the angle of β is $\sim 90^\circ$ or $\sim -90^\circ$. This has no consequences for our conclusion on the apsidal motion (section 5.4.2), but it might suggest a different route to misalignment (section 5.4.2). We find that $\sim 10\%$ of our bootstrap runs find a minimum at $\sim -88^\circ$ and $\sim 90\%$ a minimum at 93°. (Each run starts with parallel axes of both stars.) The latter is therefore our preferred value for β_s.

Furthermore our model does not include the fact that the shape of the stellar line changes

from the center towards the limb of the star. This can in particular introduce systematics in the parameters for $v \sin i$ and ζ_{RT} (See also Chapter 4.4.2 for a discussion on this subject). However in the same chapter we show, using a much higher S/N ratio mean stellar absorption profile (Broadening function), albeit for slower rotating F stars, that this does not have any significant influence on β, the parameter we wish to determine with the work in this chapter. We are therefore confident that this does not constitute a major additional source of systematics for the fitted values of β.

In addition, our program oversimplifies the velocity fields on the stellar surface, as it assumes that the same surface area is covered by material moving tangentially and by material moving radially. This is not true for early type stars like the ones in the DI Herculis system as can be seen in bisector analysis (Gray 2005). However, changing the ratio of the surface areas covered by the different velocity fields does not significantly change the values for the fitted stellar parameters. The stellar rotation is simply the dominant broadening mechanism for these two stars. However, as our understanding of the velocity-fields on stellar surfaces of early type stars is not complete, it would be interesting to observe the RM-effect in a system for which the components have a lower $v \sin i$.

A set of parameters for which disagreement with the literature values exists, and which are important to derive the expected apsidal motion rate, are the projected rotational velocities of the stars. We derive for $v \sin i_p$ and $v \sin i_s$ values of 108 km s^{-1} and 119 km s^{-1} respectively. Guinan & Maloney (1985) estimated the $v \sin i$ for both components to be ~ 45 km s^{-1}. This value is a conservative estimate as a higher $v \sin i$ would have increased the disagreement between expected and measured apsidal motion even more (see Section 5.4.2). We are, given our experience with V1143 Cyg and including the systematics discussed in these paragraphs, confident that the derived parameters have an uncertainty not greater than 10 km s^{-1}.

Note that our results for the stellar parameters, and in particular for β, are reproduced if we use literature values for the orbital parameter of DI Herculis (not shown here). While this is not surprising, as our orbital parameters are similar to the literature values, this gives us extra confidence that our approach is not dominated by systematic errors. Finally, one should note that the fit for which we used parallel rotation axes produces a significantly worse fit to the data during eclipses as can be seen in the Figures 5.4 and 5.6. Furthermore this fit finds an orbital inclination (i) far outside of the 1σ interval given for this value in the literature, as can be seen in Table 5.2. Keeping the orbital inclination fixed to its literature value, other orbital parameters (especially T_0, P, e, and ω) are found to be outside of the error-margins of the literature values (not shown here). We therefore conclude that our conclusion that the rotation axes in the DI Herculis system are misaligned is solid.

We will now focus on the discussion about the consequences of this result for the expected apsidal motion rate in the next section and then shortly mention possible causes of misalignment in Section 5.4.2.

5.4.2 Implications of the misaligned rotation axes

Apsidal motion

How does a misalignment of the stellar rotation axes influence the expected apsidal motion? The effect of a misalignment between the stellar rotation axes and the orbital spin axis on the apsidal motion has been studied by Kopal (1978); Shakura (1985); Company et al. (1988) and Petrova & Orlov (2003). The contribution of the stellar rotation to the advance of the longitude of the periastron is reduced if the stellar rotation axis is tilted with respect to the orbital spin axis until, finally, when the axis of stellar rotation lies in the orbital plane, its contribution is half as large, and with the opposite sign, compared to when the stellar and orbital axes would be parallel. In this situation, it contributes to a retrograde rotation of the periastron. The contribution of the stellar rotation to the apsidal motion depends not only on the orientation of the axis, but also on the square of the angular stellar rotation rate. As one measures only $v \sin i$, a greater inclination towards the observer would mean a higher angular stellar rotation rate, and therefore a greater contribution of the rotation term to the overall apsidal motion. In this study we derive only the angle between the projection of orbital spin axis and the stellar spin axes. We therefore have only limited information on the geometry.

Table 5.3 — Expected apsidal motion of the orbit of the DI Herculis system for a few different orientations of the stellar spin axes, and rotational speeds of the components.

V_p km s^{-1}	V_s km s^{-1}	β_p [°]	β_s [°]	$incl_p$ [°]	$incl_s$ [°]	dω/dt [° /cycle]
45	45	0	0	0	0	0.00127
105	116	0	0	0	0	0.00238
105	116	71	93	0	0	0.00049
120	133	71	93	30	30	0.00031
			measured			0.00029±0.000041

In Table 5.3 we show a few expected apsidal motion rates (dω/dt) for the DI Herculis system for different degrees of misalignment between the axes. The first column is a reproduction of the results obtained by Guinan & Maloney (1985) who estimated a $v \sin i$ of 45 km s^{-1} and assumed aligned axes. The second row shows ω for the observed $v \sin i$ with the rotation axes aligned. For this case the difference between the measured and expected apsidal motion amounts to nearly a factor of 10. The next row shows the expected apsidal motion for the case that the components have no inclination towards us – rotational speed (V) is equal to the projected rotational speed ($v \sin i$). For this case the disagreement is reduced to a factor of 2. The next row shows our calculations for a moderate amount of inclination of 30° for both stellar spin axes. For this case the expected and measured values for (dω/dt) agree with each other. From a statistical point of view it is expected that the stars show a certain degree of inclination, the position of the Earth does not constitute a preferred reference frame for the stars in DI Herculis and it also appears from the measurements of β that the orbital frame of DI Herculis does not constitute such a

system. We therefore conclude that a misalignment of the different spin axes in DI Herculis is responsible for the low observed apsidal motion rate in this system.

Star formation and evolution

An interesting question is how the stars in the DI Herculis system end up having a completely different angular momentum vector than their orbit. Have they formed with their formation axes misaligned, and if so, how was it possible to maintain the misalignment during subsequent phases? There are a number of ways stars can acquire tilted rotation axes in binary systems, see for example Monin et al. (2007) for a discussion on this subject. A interesting mechanism for DI Herculis would be the mechanism suggested by Bonnell et al. (1992). According to these authors a situation like in DI Herculis can arise if the initial cloud, out of which the binary forms, is elongated and its rotation axis is misaligned to the cloud axis. However, if the stars have formed with misaligned axes, it is not clear how they can remain having misaligned axes, as it is thought that during the pre-main-sequence phase, when the stars are more extended, tidal forces are strong and align the axes.

The spin axes of the stars could also get misaligned after their formation. One mechanism would be Kozai migration which might be responsible for the existence of a number of close binaries (e.g. Fabrycky & Tremaine 2007). For $i > 39.2^\circ$ between the orbits, the torque from the outer body causes the inner orbit's orientation to librate, while i and e oscillate. During the phases of high eccentricity, tidal forces dissipate energy and ultimately shrink and circularize the orbit. So far no third body has been found. If a third body exists, the Kozai migration might have helped to shrink the orbit of an originally already misaligned binary system, which would also help to explain the existence of DI Herculis as for a wider system tidal forces during the pre-main-sequence phase might not have aligned the system. As DI Herculis is a very young system it would be interesting to model how long the Kozai migration would have needed to work as this might constrain the parameters of the potential third body. Also other 3-body mechanisms, like a close encounter, might have influenced the relative orientations of the spin axes. Another possible cause for the misalignment could be the ejection of the binary out of a cluster which might have changed the orientation of the orbital and stellar axes.

Here we cannot answer how the axes in the DI Herculis system ended up being misaligned. In the future we will attempt to exclude at least a number of scenarios, of which we did only list a few in the above paragraphs, by carrying out further observations and more detailed modelling.

5.5 Conclusion

We observed the DI Herculis system during and out of its eclipses with the high resolution Echelle spectrograph Sophie at the OHP. We have shown that the stellar rotation axes are neither aligned with each other nor with the orbital angular momentum. The projections between the stellar spin axes and the orbital spin axis span angles of $71 \pm 4^\circ$ and $93 \pm 8^\circ$, respectively. This is the first clear demonstration of such a strong misalignment. It further solves a 20-year-old mystery about this system: the observed orbital precession is too slow to be in agreement with the predictions made by Newtonian mechanics and general relativity. This prediction was based on the premise of co-aligned stars. When this assumption is relaxed, as shown

by our observations, the paradox disappears. The results of these measurements contain new challenges for binary formation and evolution theories.systems like DI Herculis.

Acknowledgments

We would like to thank the team which designed and build the amazing Sophie spectrograph and its software. We are also grateful for the support from the complete team at the OHP observatorie. Also thanks to Yuri Levin for enlightening discussions.

Bibliography

Bagnuolo, Jr., W. G. & Gies, D. R. 1991, ApJ, 376, 266 88
Bonnell, I., Arcoragi, J.-P., Martel, H., & Bastien, P. 1992, ApJ, 400, 579 96
Claret, A. 1998, A&A, 330, 533 82
Claret, A. & Gimenez, A. 1993, A&A, 277, 487 82
Claret, A. & Willems, B. 2002, A&A, 388, 518 82
Company, R., Portilla, M., & Gimenez, A. 1988, ApJ, 335, 962 82, 95
Fabrycky, D. & Tremaine, S. 2007, ApJ, 669, 1298 96
Gray, D. F. 2005, The Observation and Analysis of Stellar Photospheres (The Observation and Analysis of Stellar Photospheres, 3rd Edition, by D.F. Gray. ISBN 0521851866. Cambridge, UK: Cambridge University Press, 2005.) 90, 94
Guinan, E. F. & Maloney, F. P. 1985, AJ, 90, 1519 82, 83, 90, 92, 93, 94, 95
Guinan, E. F., Marshall, J. J., & Maloney, F. P. 1994, Informational Bulletin on Variable Stars, 4101, 1 82, 90
Hipparcos. 1997, ESA SP-1200 83
Kopal, Z., ed. 1978, Astrophysics and Space Science Library, Vol. 68, Dynamics of Close Binary Systems 82, 95
Marshall, J. J., Guinan, E. F., & McCook, G. P. 1995, Informational Bulletin on Variable Stars, 4161, 1 82
McLaughlin, D. B. 1924, ApJ, 60, 22 83
Monin, J.-L., Clarke, C. J., Prato, L., & McCabe, C. 2007, in Protostars and Planets V, ed. B. Reipurth, D. Jewitt, & K. Keil, 395–409 96
Petrova, A. V. & Orlov, V. V. 2003, Astrophysics, 46, 329 82, 95
Popper, D. M. 1982, ApJ, 254, 203 90, 92, 93
Press, W. H., Teukolsky, S. A., Vetterling, W. T., & Flannery, B. P. 1992, Numerical recipes in FORTRAN. The art of scientific computing (Cambridge: University Press, |c1992, 2nd ed.) 90
Rossiter, R. A. 1924, ApJ, 60, 15 83
Shakura, N. I. 1985, Soviet Astronomy Letters, 11, 224 82, 95
Snellen, I. A. G. 2004, MNRAS, 353, L1 83
Winn, J. N., Noyes, R. W., Holman, M. J., et al. 2005, ApJ, 631, 1215 83

Chapter 6

Ground based transmission spectroscopy of the atmosphere of HD 209458b using the VLT

Recently, Snellen et al. (2008) have presented the ground-based detection of sodium in the transmission spectrum of the extrasolar planet HD 209458b. They showed that under good atmospheric circumstances and with the right observing strategy and analysis methods, ground-based transmission spectroscopy of exoplanets can lead to detections. The aim of this chapter is to show that the sodium absorption also appears in another ground-based data set, that transmission spectroscopy can be done routinely from the ground, and to target, besides sodium, also potassium in the atmosphere of HD 209458b. We carried out ground-based transmission spectroscopy of HD 209458b using the UVES spectrograph at Kueyen (Unit Telescope 2) of the Very Large Telescope at the Paranal Observatory. The obtained spectra have been corrected for instrumental effects which influence the transmission spectroscopy, such as a change of the blaze function of the spectrograph, and a non linearity effect in the CCD. Furthermore the influence of telluric sodium absorption, and absorption due to water in earth's atmosphere has been corrected for in the spectra. Although the first part of the transit was missed due to technical problems, and the weather was less stable than during the Snellen et al. (2008) observations, we also detect sodium. Our measurements are fully consistent with earlier results. We further extend these observations by measuring the ratio between the Na D_2 and Na D_1 lines to be ~ 1.8. Around the centre of the transit the planetary sodium absorption seems to be less deep than during the rest of the transit, of which a hint is also seen in the Snellen et al. (2008) data. If real, this could be caused by the change in relative radial velocity of the planet with respect to that of the star, with the planets absorption centered at the heart of the stellar absorption line during mid-transit. For absorption by potassium in the atmosphere of HD 209458b, we find an upper 3-σ limit of 0.042% in a passband of 1.5Å.

S. Albrecht & I.A.G. Snellen
A&A to be submitted

6.1 Introduction

A stellar spectrum observed through the atmosphere of a transiting planet carries the spectral imprint of the atomic and molecular species in that atmosphere, making the depth of the transit wavelength dependent. Comparing in-transit with out-transit spectra of the host star can therefore reveal information about the composition and structure of the planet's atmosphere (e.g. Seager & Sasselov 2000) which would otherwise remain inaccessible. This opens the fascinating possibility to study the physical and chemical characteristics of these alien atmospheres. For hot Jupiters two prominent absorption features are expected caused by resonance lines of alkali metals in the visible wavelength band. Absorption by sodium in the Na D lines at 5889 Å and 5895 Å, and absorption by potassium in the K I lines at 7665 Å and 7699 Å (e.g. Brown 2001). Charbonneau et al. (2002) were the first to detect the sodium feature in the transmission spectrum of an extra solar planet, HD 209458b using the Space Telescope Imaging Spectrograph (STIS) on board of the Hubble Space Telescope (HST). This way, for the first time information is received about the conditions in an atmosphere of an planet orbiting a different sun. This same data set has recently been re-analyzed by Sing et al. (2008a,b), showing the presence of an additional broad absorption component. The only successful ground-based observations of an extra solar planetary atmosphere have been presented by Redfield et al. (2008) and from our group (Snellen et al. 2008). Redfield et al. (2008) detected sodium absorption by the atmosphere of HD 189733b using the Hobby-Eberly Telescope. Snellen et al. (2008) re-analyzed archival HDS/Subaru data of HD 209458 for a range of different passbands. Their findings are fully consistent with the results by Charbonneau et al. (2002) and Sing et al. (2008a).

We here continue these measurements to pursue three aims. The first goal is a further investigation of the sodium absorption by the atmosphere of HD 209458b. Second, to show that these observations can be routinely done also with the Very Large Telescope (VLT). Our final goal is to search for absorption by potassium, which is expected to produce absorption at a similar level as sodium in the atmosphere of HD 209458b. This chapter is structured as follows: In Section 6.2 we describe the observations from ESO's Paranal Observatory. Subsequently, we present our analysis and results for sodium and potassium in the sections 6.3.1 and 6.3.3. The discussion in section 6.4 is followed by our conclusions.

6.2 UVES VLT observations

On the night of August 13, 2006 we obtained 56 high resolution spectra of HD 209458 using the Ultraviolet and Visual Echelle Spectrograph (UVES, Dekker et al. 2000) on Kueyen (UT2) of the VLT. Sixteen observations were taken during, and forty after, the planetary transit. The beginning of the transit was missed partly because of bad weather and technical problems. The sky remained partly cloudy throughout the night. In Figure 6.1 the atmospheric conditions for each observation are shown. The 1D-seeing, indicated by the dashed line, is measured from the 1D stellar profile on the CCD. The strength of telluric water lines, which is arbitrary normalized and indicated by crosses, is measured by a set of strong H_2O lines. The dotted line shows the normalized continuum count level in each observation. Note the particularly low count levels for frames 17 – 20. These frames have been significantly influenced by clouds, while the integration were stopped a few times, because the telescope had lost track of the star.

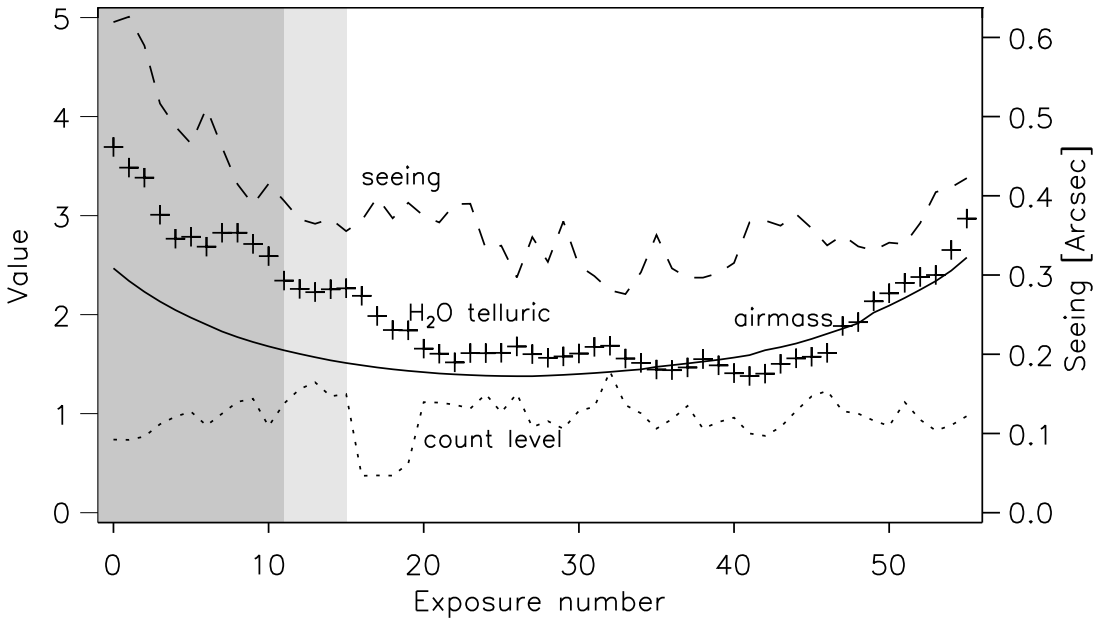

Figure 6.1 — The panel shows the environmental conditions during the observations of HD 209458 at the VLT in the night 13/14 August 2006. The grey areas indicate the timing of the planetary transit and period of egress. The solid line indicates the airmass for which HD 209458b was observed, and the dotted line indicates the normalized flux in the exposures. The dashed line shows the seeing (in σ) as measured from the the one-dimensional profile of the star along the slit. The crosses indicate the strength of telluric water lines.

These frames are shown here but have been excluded from the analysis.

The data were taken using a free template, with dichroic 2, and cross disperser 2 (CD2). Using a slit of 0.5 $''$, which was aligned with the parallactic angle, a resolving power of R $\sim$ 65 000 was obtained and a wavelength range of 3800 Å $< \lambda <$ 9000 Å was covered. Typical exposure times were 400 seconds, but for a few observations the exposure time was altered to account for changes in the flux level, and to achieve an as uniform as possible S/N level for each observation throughout the night. After initial data reduction, using the ESOREX (version 3.6.1) software package [1] , we extracted spectra with a S/N ratio between 200 – 300 in the continuum around the Na D lines and with a similar S/N ratio in the continuum around the K I potassium lines.

6.3 Transmission spectroscopy

The relative strength of the absorption features is determined in each reduced spectrum by integrating the flux in a wavelength band centered around the appropriate wavelength. This flux is divided by the flux in adjacent, equally wide bands on the short and long wavelength side of the central wavelength band. Differences of these ratios between in-transit and out-transit

[1] We used the -reduce.extract.profile='gauss' option for the uves_obs_scired recipe, because the default option 'virtual' to extract the orders resulted in a quasi periodic pattern, even if the resolution is chosen to be 0.1 pixel.

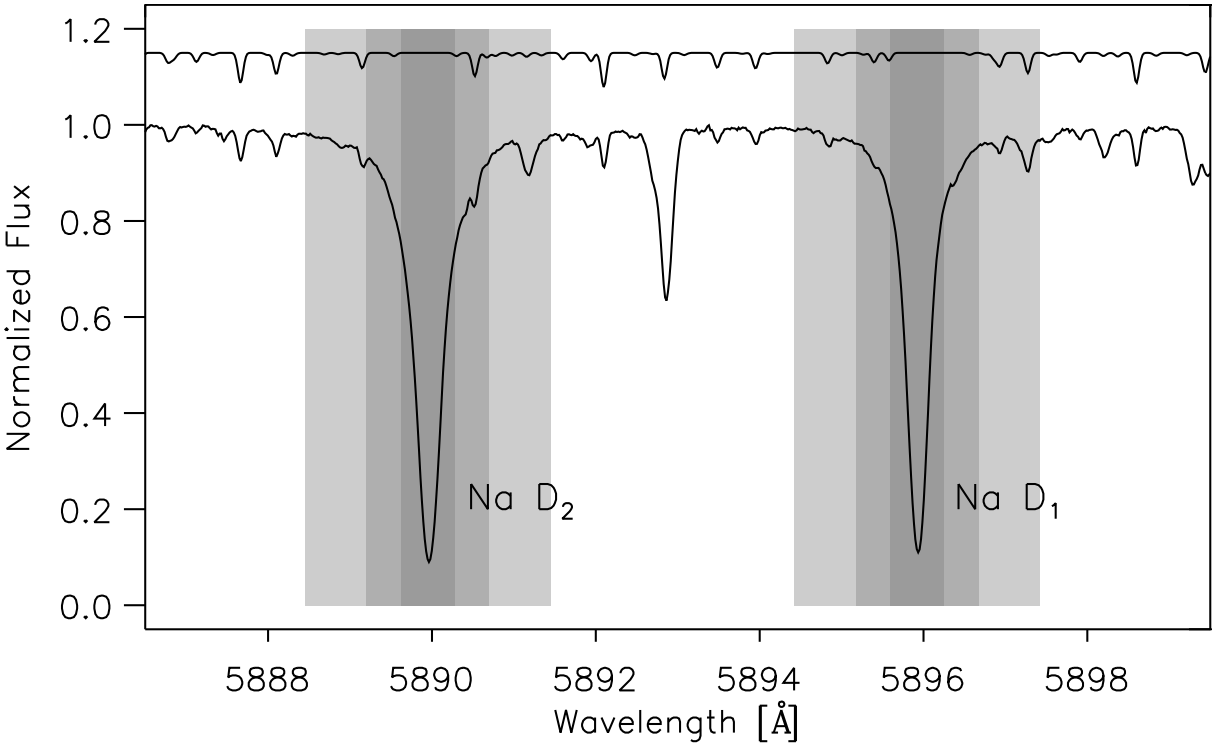

Figure 6.2 — This figure shows a spectrum of HD 209458b obtained with UVES at the UT2. The shaded regions represent three central passbands with a width of 2×0.75 Å, 2×1.50 Å, and 2×3.0 Å. The upper spectrum represents a telluric spectrum, mainly consisting of H_2O lines, created using the line list of Lundstrom et al. (1991).

spectra, are subsequently attributed to absorption:

$$\left.\begin{aligned} F_{\rm left} &= \int_{\lambda_0-\frac{3}{2}\Delta\lambda}^{\lambda_0-\frac{1}{2}\Delta\lambda} F(\lambda)d\lambda \\ F_{\rm cen} &= \int_{\lambda_0-\frac{1}{2}\Delta\lambda}^{\lambda_0+\frac{1}{2}\Delta\lambda} F(\lambda)d\lambda \\ F_{\rm right} &= \int_{\lambda_0+\frac{1}{2}\Delta\lambda}^{\lambda_0+\frac{3}{2}\Delta\lambda} F(\lambda)d\lambda \end{aligned}\right\} \quad F_{\rm line} = \frac{2F_{\rm cen}}{F_{\rm left}+F_{\rm right}} \tag{6.1}$$

where $F_{\rm cen}$, $F_{\rm left}$, and $F_{\rm right}$ are the measured fluxes in the central and two adjacent comparison bands. The center wavelength of the absorption line is indicated by λ_0, and $\Delta\lambda$ stands for the total width of each of the passbands. The flux ratios of the central to adjacent bands is indicated by $F_{\rm line}$, which should be lower during transit if absorption by the planet atmosphere is detected.

6.3.1 Sodium

We searched for absorption by sodium around the Fraunhofer D resonance lines. The exact position of the line center was determined through Lorentzian fitting for the Na D lines, and Gaussian fitting for other comparison lines. For the Na D_2 line the exact position was also determined after the change in strength of a telluric water line, which lies on the wing of the stellar line, was removed. Figure 6.2 shows the spectral region around the Na D doublet, with the three central passbands used in our and in the analysis by Snellen et al. (2008) are indicated by gray shaded areas. The passbands, used for comparison, are always located directly next to these.

Before Equation 6.1 can be used to derive the absorption of the planetary atmosphere, other effects which change with time and which influence the ratio between the central and sidebands, both instrumental and induced by the earth atmosphere, have to be excluded.

Instrumental effects

Two important instrumental effects influence our spectra. The blaze function of the spectrograph slowly changes over night and introduces a change of flux between the different bands over the time scale of a planetary transit. The use of Equation 6.1 only prevents zero or first order effects to influence the transmission spectroscopy. Any higher order effect, e.g. a change in spectral curvature of the blaze function will not be corrected for. A good way to treat the change of the blaze function in transmission spectroscopy is explained in Winn et al. (2004), has been applied by Snellen et al. (2008), and is also followed in this chapter: Fortunately, the blaze functions change only very slowly as a function of the spectral order. Therefore, one can use the change in blaze function between frames in the two adjacent orders to correct for the change in the blaze function in the order of interest, without introducing possible systematic effects due to the planetary absorption.
The second instrumental effect for which we corrected is a non-linearity in the conversion factor of the CCD and its electronics. If the conversion factor decreases slowly towards a high count level, but this is not taken into account by the reduction software, then high count levels are overestimated and low count levels are underestimated. If the count level for each exposure changes, one expects that the depth of an absorption line is underestimated for high count levels and vice versa. This effect has been first identified by Snellen et al. (2008). To quantify this effect we measured the depth of 40 deep absorption lines, for which we do not expected that planetary absorption plays a role, for each exposure in a 0.75 Å passband. Note that all these lines are located on the lower red CCD of UVES. By comparing Figure 6.3 with Snellen et al. (2008) Figure 3. one can see that the effect in our data set is a factor ~ 2 lower than in their data set. We corrected for this effect in the same way as in Snellen et al. (2008). A comparison of the corrected and uncorrected absorption depth for the 40 lines plotted as a function of exposure number can be seen in Figure 6.4.

Earth's atmosphere

For ground-based observations, one also has to correct for telluric effects. In the wavelength regions of the Na D lines, changes in the strength of telluric absorption lines, caused by H_2O and also sodium in the Earth atmosphere, can be problematic. Note that the regions in the

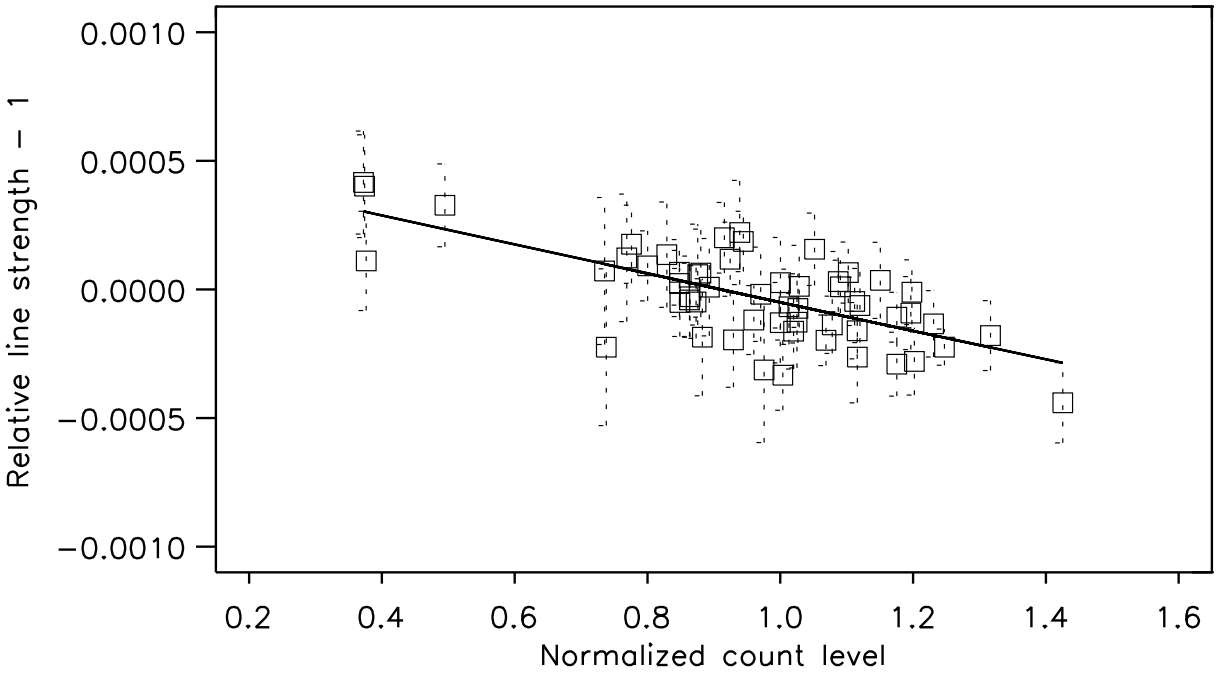

Figure 6.3 — Normalized mean line depth of 40 strong stellar lines plotted as a function of the normalized flux for the 56 exposures. A clear trend is visible, indicating that a non-linearity influences the data.

earth atmosphere where the telluric water lines and the telluric sodium absorption originate are not identical and therefore the change of these telluric features over time can differ. See figure 6.5 for a zoom in the spectral region around the stellar Na D_2 lines, where one can see the development over night of two prominent H_2O absorption lines and the telluric sodium Na D_2 line.

Telluric sodium: An important contribution of the earth's atmosphere to the observed spectra is additional sodium absorption. This absorption is, due to the relative difference in radial velocity between earth's atmosphere and HD 209458 ($\sim$ 23 km sec^{-1}) displaced by $\sim$ 0.45 Å relative to the stellar sodium lines (Figure 6.5). The development of the strength of the telluric Na D lines can therefore be measured and is shown in Figure 6.6. Clearly the change in the Na D_1 line over the night and its absolute strength are lower compared to that of the D_2 line. We corrected for the telluric sodium in the following way. First a reference spectrum was constructed from 5 frames (nr. 24 – 28) taken at low airmass. Each individual frame of the night was subsequently divided by this reference spectrum. In this way the change (not the absolute value) of the telluric sodium absorption becomes visible, which was fitted with a Gaussian fixed in position and width. This Gaussian model to the change in telluric sodium absorption was subsequently removed from the spectra to make its contribution constant with time. Variations in the D_2/D_1 ratio at Paranal are not uncommon, but have only been measured on a longer timescale, with an average line ratio of 1.6 (see Patat 2008). Our correction for the telluric sodium will hide the sodium signal of the atmosphere of HD 209458b over the wavelength range of 0.05 Å. However, as the smallest band-pass employed in this study is 0.75 Å we expect no

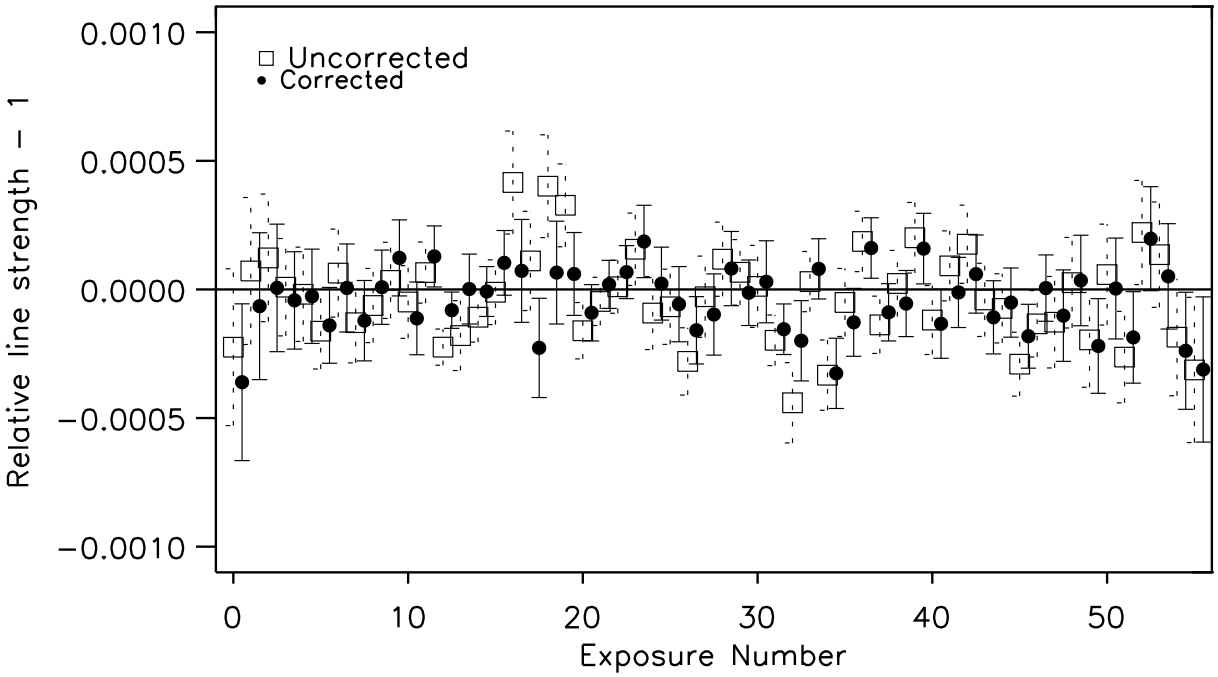

Figure 6.4 — Uncorrected (empty squares) and corrected (filled circles) average normalized mean line depth of 40 strong stellar lines plotted over the exposure number. The corrected values are shifted by 0.5 in exposure number for clarity.

significant additional error, compared to our uncertainties. Moutou et al. (2001) have noticed similar features appearing and disappearing during different exposures at similar wavelengths in their study of HD 209458b's atmosphere (their Figure 4.). Note that around the same time the telluric sodium features start to strengthen in our data set, the moon is rising above the horizon. However we think this effect is unlikely caused by reflected sunlight, since the star with $m_V = 7.65$ is so much brighter compared to the sky background. It is known that the moon has its own sodium atmosphere which extends to several times the radius of the moon and covers several degrees on the sky (see Mendillo 2001). However, HD 209458's angular distance on the sky ($\sim 50\,^\circ$) was too large for our measurements to be influenced by it, and this distance does not change over the course of one night as the sodium feature does. Most likely it is the change in weather pattern in the Earth's upper atmosphere which is responsible for the increase in the line strength of the telluric sodium absorption. For example the cloud coverage varied over night.

Water lines: The main contribution of the telluric spectrum around the Na D doublet consists of water absorption lines (see Figures 6.2 and 6.5). We measured the change in strength of strong water lines in the 7000 Å regime as a tracer for the strength of the telluric water lines around the Na D doublet, since these lines can be measured much more accurately. The crosses in Figure 6.1 show the scaled development of the mean of these absorption lines over time. We confirmed this measurement with measurements of the weaker H_2O lines around the Na D doublet, but at a higher noise level. Due to the change in weather conditions during the night, the strength of the water lines does not follow the airmass: If it had been a perfectly stable

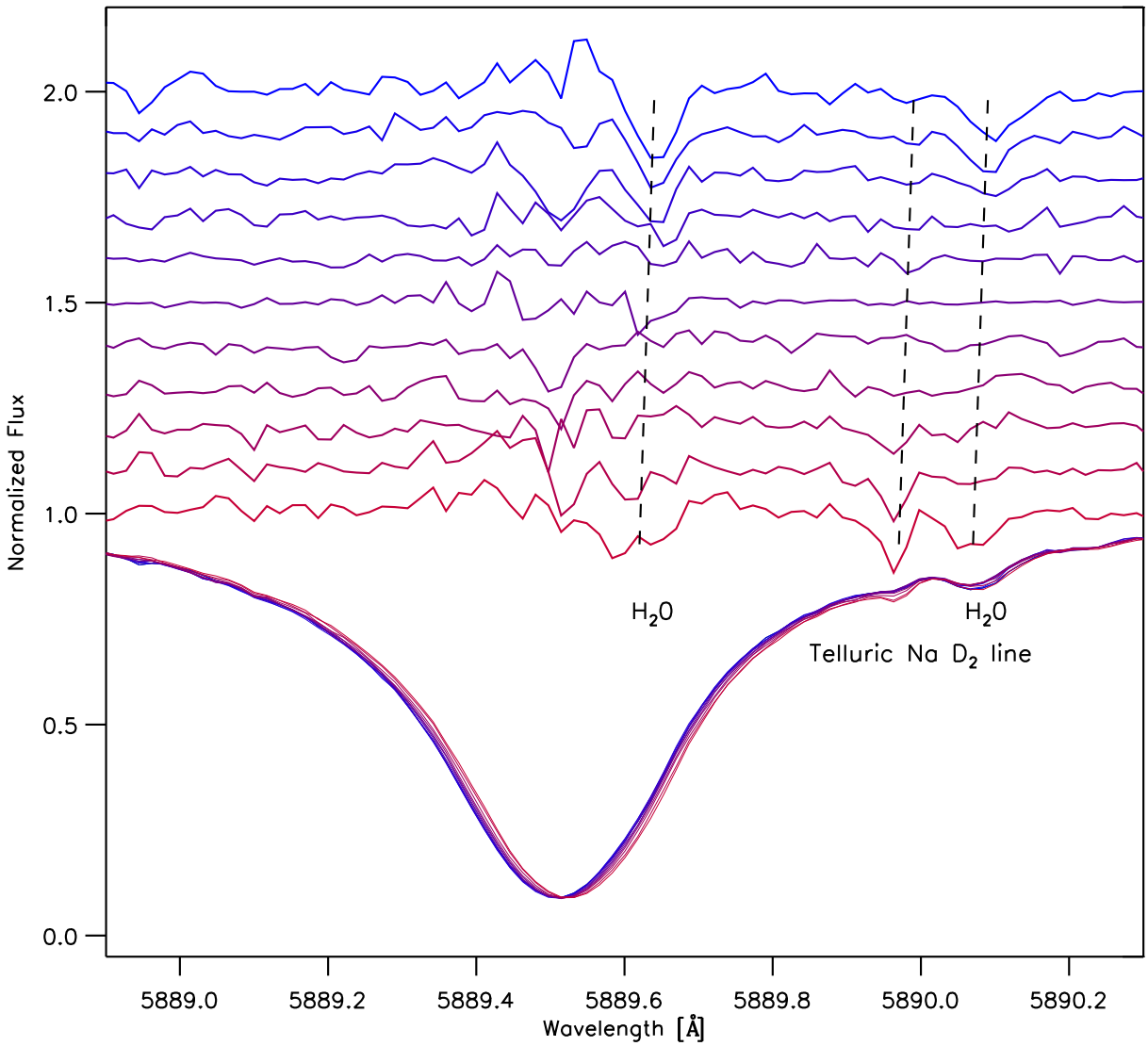

Figure 6.5 — The spectral region around the Na D_2 line. Eleven spectra are plotted as function of wavelength in the rest frame of the observatory. Each spectrum represents the median of 5 consecutive frames. One can see that the stellar absorption line shifts in wavelength space over night by ~ 0.02 Å towards longer wavelengths. The upper lines represent these median spectra divided by the median of 5 spectra obtained at low airmass (see also text) in the *stellar* rest frame. These "relative spectra" have been amplified by $\times 5$ in this plot. The median of the first five spectra obtained during the night is displayed at a flux value of 2 and each following spectrum is shifted by 0.1 units down. The wavelength position of the telluric sodium line and two strong H_2O lines are indicated. Also indicated by the slightly tilted lines is the relative shift of the telluric lines in the stellar rest frame over time due to the change in relative radial-velocity. The water lines are prominent at the begin of the night, decrease during the middle, and increase later again. The telluric sodium line does not change significantly over the first half of the night, and later increases in depth. Note that the S/N in the "relative spectra" is significantly lower in the core of the Na D_2 line as a low flux level is divided by a low flux level.

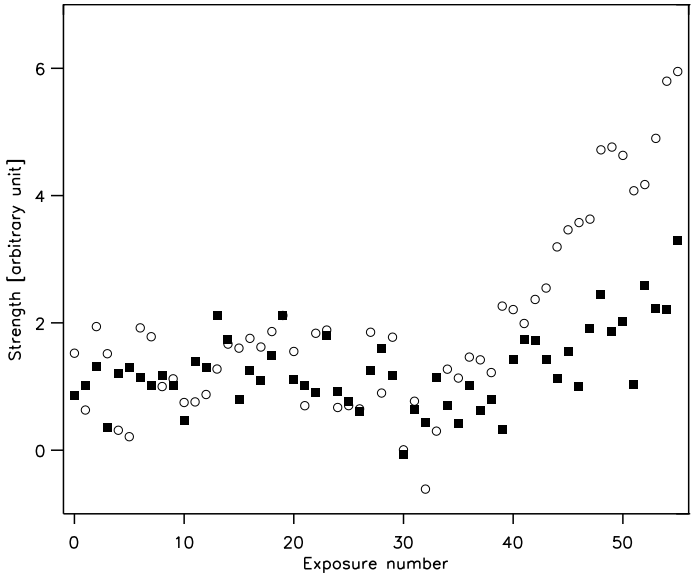

Figure 6.6 — The development of the two telluric sodium lines as a function of the exposure number. The D_1 line is represented by filled squares and the D_2 line by open circles.

night, the water column would have been constant in time, and purely a function of viewing angle, making the strength of the H_2O telluric lines follow airmass (see Snellen et al. 2008).

The change in absorption of stellar light by telluric water in the different spectra effects the data reduction and the transmission spectroscopy in two ways. Firstly, the contribution of telluric H_2O lines in the central passband will make the observed absorption appear deeper, while those lines located in the adjacent bands will make it appear shallower. It therefore depends on the distribution of H_2O lines and the size of the passbands in which way telluric H_2O lines will influence the measurements. Secondly, the telluric lines in the adjacent orders also influence the results in a indirect way, since these orders are used to correct the blaze function of the spectrograph. One can correct for both effects, after conducting the transmission spectroscopy by correlating the strength of the strong telluric water lines around 7000 Å with the measured strength of the Na D absorption outside the transit, and use the inferred coefficient to correct all spectra of the night, and afterwards find the difference in absorption depth during and out of transit. We measured the relative line strength of the sodium absorption in three passbands around the two Na D lines for passbands similar to those used by Snellen et al. (2008) and Sing et al. (2008a). See section 6.3.2 and Figure 6.8 for our results using this method.

Instead of removing the influence of the telluric water lines in the transmission spectroscopy one can also remove the change of the strength of the telluric lines in the spectra itself, before carrying out the transmission spectroscopy. For this we used the information on telluric lines in the wavelength region around the Na D doublet compiled by Lundstrom et al. (1991) to create a model telluric spectrum. Lundstrom et al. (1991) provided the wavelength positions and most importantly the relative depth of the different telluric lines. This approach has two weaknesses. The relative strengths of the different absorption lines have to be known to very high accuracy to remove all changes. Furthermore the effect mentioned above; the influence of the correction of the change of the blaze function of the spectrograph due to the water lines can not be corrected in this way. However, the advantage is that one can take into account the relative movement of the telluric lines with respect to the stellar absorption lines during the night. The radial velocity of the star changed, mainly due to acceleration of the observatory relative to the star, by nearly 1km sec^{-1}, equivalent to a shift of ~ 0.02 Å at 6000 Å (see also Figure 6.5). Therefore keeping

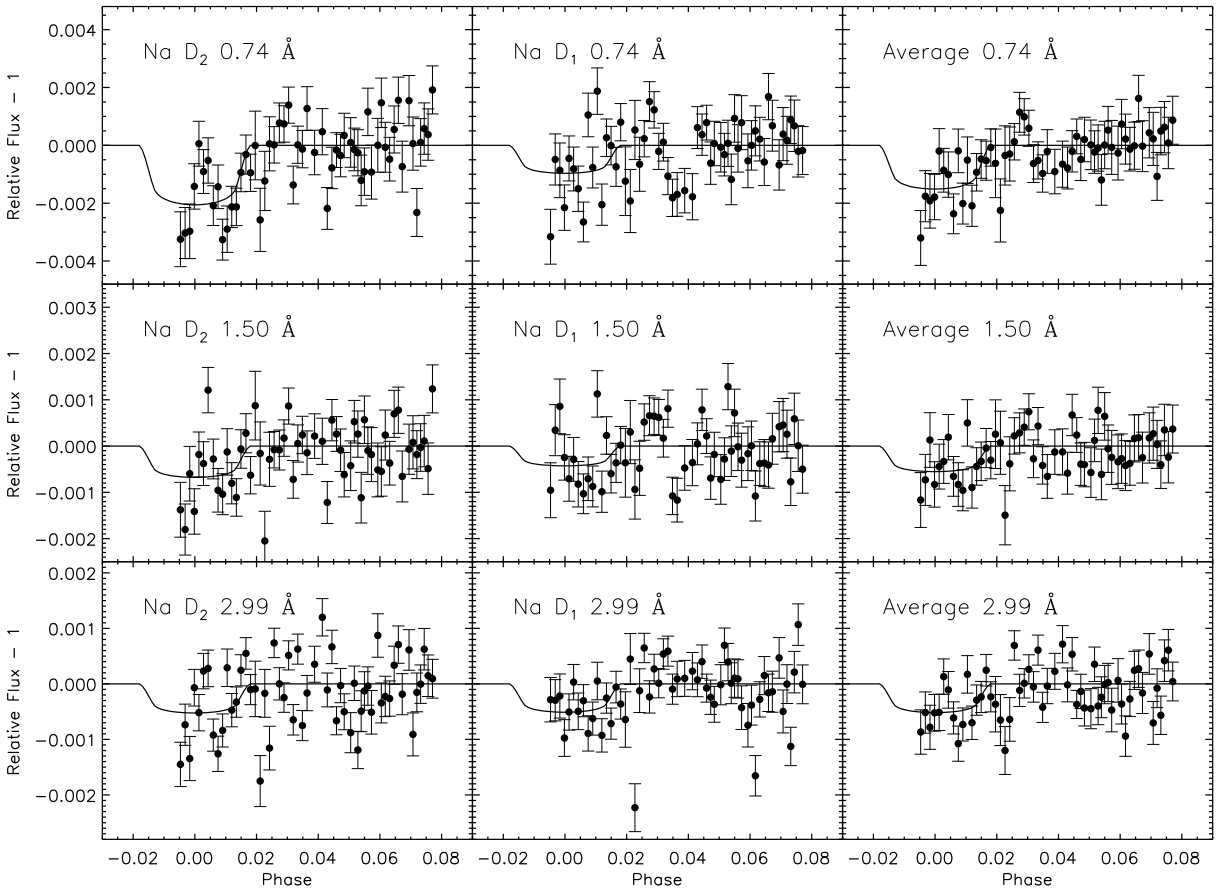

Figure 6.7 — The left panels show the sodium absorption in the Na D_2 line for the three different passbands of 0.75 Å, 1.5 Å, and 3.0 Å, in the top, middle, and bottom panel, respectively. The middle panel show the same for the Na D_1 line and the right panels for the average of the two. The solid line represents our best fit.

the passbands fixed in the rest frame of the star can mean that a telluric line is moving partly from one passband into an adjacent passband over the course of the night (see also section 6.3.3 and the Figures 6.9 and 6.10). This is not taken care of in the first method used in this work. It turns out that for the chosen passbands of 0.75 Å, 1.5 Å, 2.2 Å, and 3 Å around each sodium line no significant telluric line lies at a border of one of the passbands. Hence this effect does not influence the measured absorption due the planetary atmosphere. However, if transmission spectroscopy is conducted at many different passbands this effect is indeed important in our data set and first the synthetic spectra of telluric lines have to be subtracted from each observation, scaling it to the overall depth of the telluric features in that observation. This way the change in the telluric lines over time is removed to a high degree and the absorption due to HD 209458b's atmosphere can be calculated at different passbands. A final correction for the telluric features is still needed in the transmission spectroscopy due to residuals in the removal of the telluric lines and the influence the change of the telluric lines has on the blaze correction. Furthermore, we did not remove the change in the strength of the telluric water line located in the core of the Na D_2 line (only to derive its exact position in wavelength). Due to the low flux and the

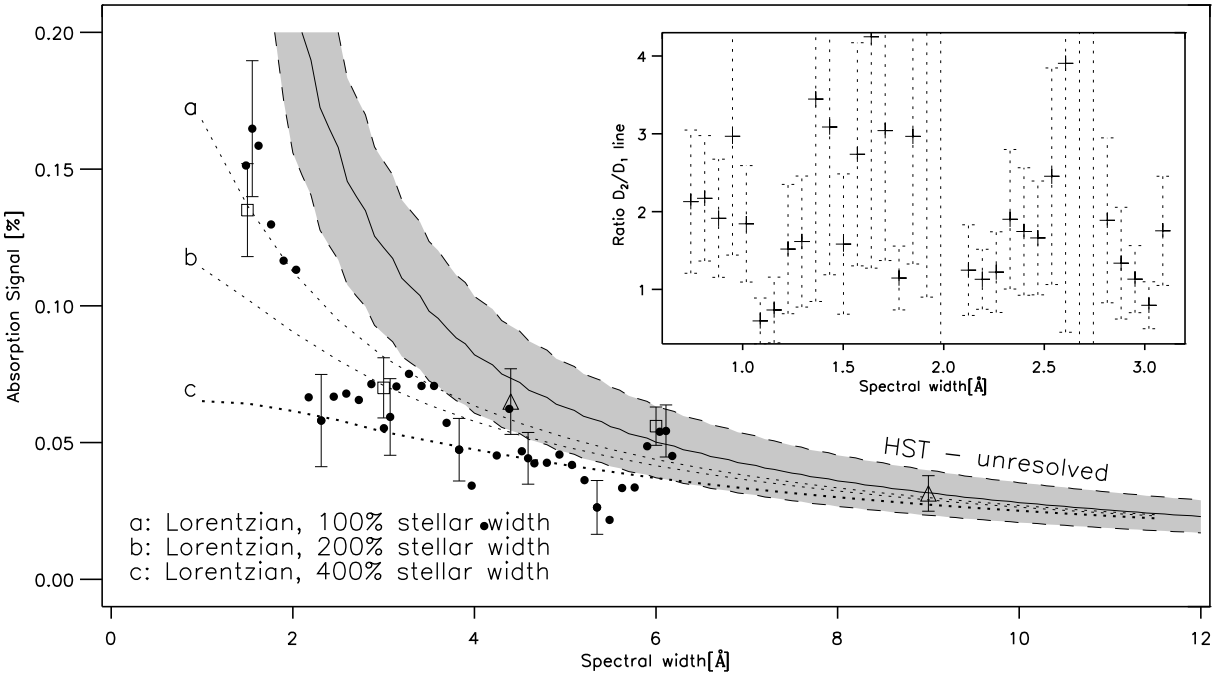

Figure 6.8 — Transmission spectroscopy around the Fraunhofer D line. The absorption signal in the two Na D lines is plotted over the total width of the central passbands. The filled circles indicate the average absorption in the D_1 and D_2 lines. Every tenth data point shows the 1-σ uncertainty. The open squares indicate the absorption signal found by Snellen et al. (2008) and the open triangles the absorption found by Sing et al. (2008a). The line indicates the absorption found by Charbonneau et al. (2002), if the absorption by the planetary line would be completely unresolved. The lines indicated by *a, b, c,* show the Na D absorption levels as a function of passband, expected from the HST measurements, assuming that the atmospheric absorption feature is Lorentzian shaped with a width equal to, 2× and 4× the stellar width of the Na D doublet. The insert shows the ratio of the depth of the absorption found in the D_2 and D_1 lines over the different band passes.

change in the relative radial-velocity a complete removal would be difficult and the fact that this line is always in the central passband means that it cannot introduce a systematic effect. Finally, the seeing changes over night (Figure 6.1), and the Rossiter-McLaughlin effect, which changes the shape of the absorption line during the transit, would further complicate a removal (see also the discussion in Snellen et al. (2008) on this subject and Chapters 4 and 5 for an in depth discussion of the Rossiter-McLaughlin effect).

6.3.2 Sodium results

The results for both methods of removal of the telluric water lines are shown, for the four passbands, in the second and third columns of Table 6.1. Both methods lines turn out to give similar results. The values agree in all four passbands with each other and with the literature values within their 1-σ uncertainties, with the exception of the values derived in the 4.4 Å passband. The latter value derived using the second method lies just outside the uncertainties of the literature value and the value derived using the first method. The correction coefficient

Table 6.1 — Comparison of the measurements of the sodium absorption by HD 209458b's atmosphere for the two different methods of correcting for the telluric water lines. The first column shows the result for which the correction for telluric water lines was carried out in the transmission spectroscopy and the second column shows the results for which the telluric water lines have been removed in the spectra and only a small additional correction was carried out. The values are given together with their 1-σ uncertainties, as derived from the χ^2 fit. The third and fourth columns show the results by Snellen et al. (2008) and Sing et al. (2008a).

Passband [Å]	This work		Snellen et al. (2008)	Sing et al. (2008a)
	Depth [%]			
1.5	0.151±0.025	0.129±0.025	0.135±0.017	
3.0	0.055±0.015	0.053±0.015	0.070±0.011	
4.4	0.062±0.011	0.044±0.011		0.065±0.012
6.0	0.052±0.010	0.042±0.010	0.056±0.007	

used to scale the telluric spectrum and the coefficient used in the former method to remove the influence of telluric lines correlate linearly, which is also expected. Furthermore we measured, using the latter method, the relative line strength of the sodium absorption in two passbands around the two Na D lines varying in width from 0.75 Å, to 3 Å in steps of 0.035 Å. The transit curves are shown in Figure 6.7 for the passbands of 0.75 Å, 1.5 Å, and 3 Å chosen to be similar to those in Snellen et al. (2008). The left panels show the absorption in the D_2 line, the middle panels in the D_1 line, and the right panels show the average of the two. All these measurements are also given in Table 6.1, and compared with the Snellen et al. (2008) and Sing et al. (2008a) results.

Instead of first conducting a fit only to the frames obtained outside of the transit, subsequently measuring and removing the telluric line contribution, and finally measuring the absorption depth, we also used the Levenberg-Marquardt least-squares minimization algorithm to simultaneously fit both the telluric line contributions and the transit depth. Both methods give similar results.

6.3.3 Potassium

Next to absorption by sodium, also absorption by potassium in the 7667 Å resonance doublet line is expected to be a prominent absorption feature in the transmission spectrum of hot giant planets (Seager & Sasselov 2000; Brown 2001). As the UVES observations cover the potassium lines at 7665 Å and 7699 Å, we searched for it in a similar way as for sodium. The potassium lines in our setting are located on the upper red CCD of the UVES spectrograph. Unfortunately, the line at 7665 Å overlaps with very strong telluric O_2 lines and we did not include it in our analysis. The wavelength region around the line at 7699 Å is shown in Figure 6.9.

To correct for the change in the blaze function of the spectrograph we used the same method as used before. As the spectral order immediately 'below' the order of interest is strongly effected by O_2 lines we used one order further away. This introduces a penalty of a slightly worse correction for the change in the blaze function.

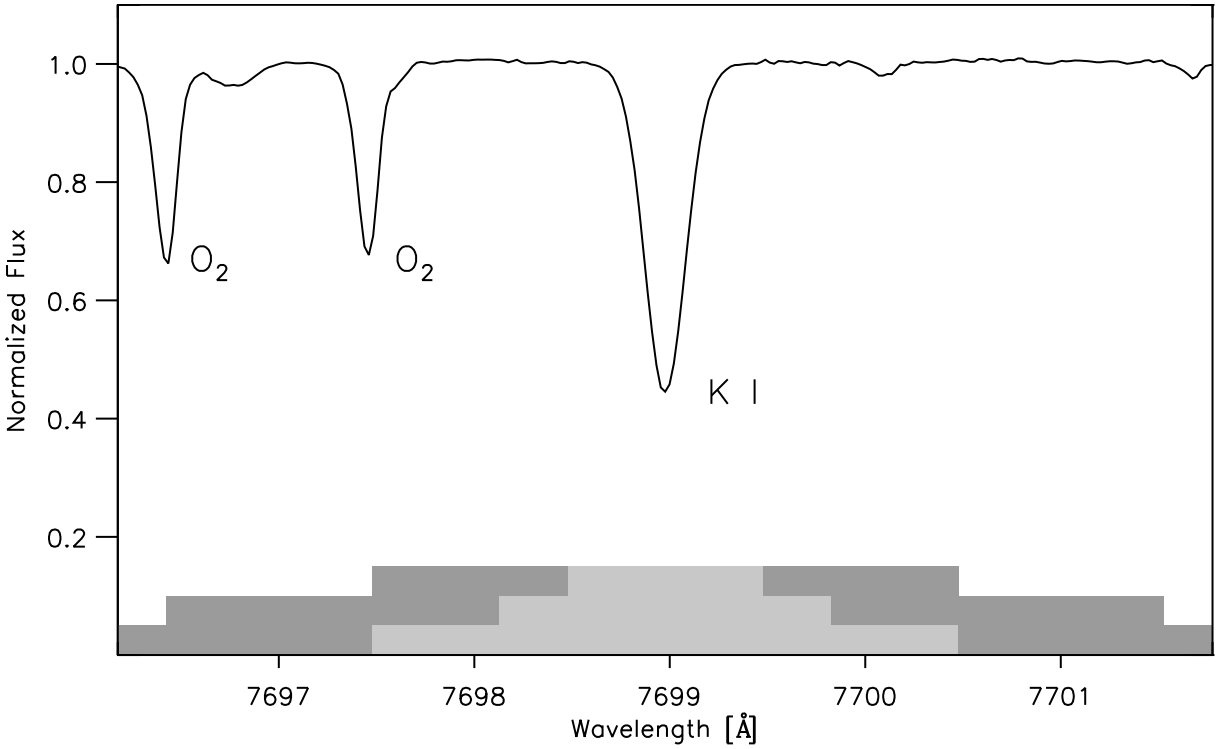

Figure 6.9 — The figure shows the spectral region around the K I line at 7699 Å, obtained with the UVES spectrograph. One can see two strong and a number of weaker telluric O_2 lines. Indicated by light gray areas are three central band-passes of 1 Å, 1.8 Å, and 3 Å, respectively. The dark gray areas indicate the sidebands.

The telluric contamination around the K I line is, besides that only one line can be used, less challenging. As expected, no absorption by telluric potassium is measured and the telluric O_2 lines in the spectral region of the K I line (Figure 6.9) follow the airmass nicely. We correct for the influence of the O_2 lines in the transmission spectroscopy after applying Equation 6.1 with a number of band-passes which have total widths between 0.4 Å and 4 Å. As in the case of the Na D lines we fit simultaneously for absorption during transit and contamination by O_2 lines.

Figure 6.10 shows the results obtained in the different band-passes. We find no significant absorption by the planetary atmosphere in the applied band-passes. In the band-passes with a width of 1.5 Å, and 2.5 Å we find 3-σ limits of 0.042%, and 0.015%, respectively. It is worth pointing out that our measurements only cover a narrow spectral band. If there exists an absorption feature by potassium which is broader than the widest band pass used here, than it would not be detected by our measurements.

Note the features at passbands of widths of $\sim$ 0.6 Å, $\sim$ 1 Å, $\sim$ 1.8 Å, and $\sim$ 3 Å, shown in Figure 6.10. These originate from the change in the wavelength position of the telluric absorption lines relative to the wavelength of the potassium absorption line over night. The sign of the derivations is positive if the telluric line moves out of the central band over the course of the night. The derivation is negative if the telluric line moves out of one of the side passbands. The signature at 3.0 Å for example originates from the movement of the telluric line at $\sim$ 7697.5 Å out of the central band (see Figure 6.9). Over the course of the night, the

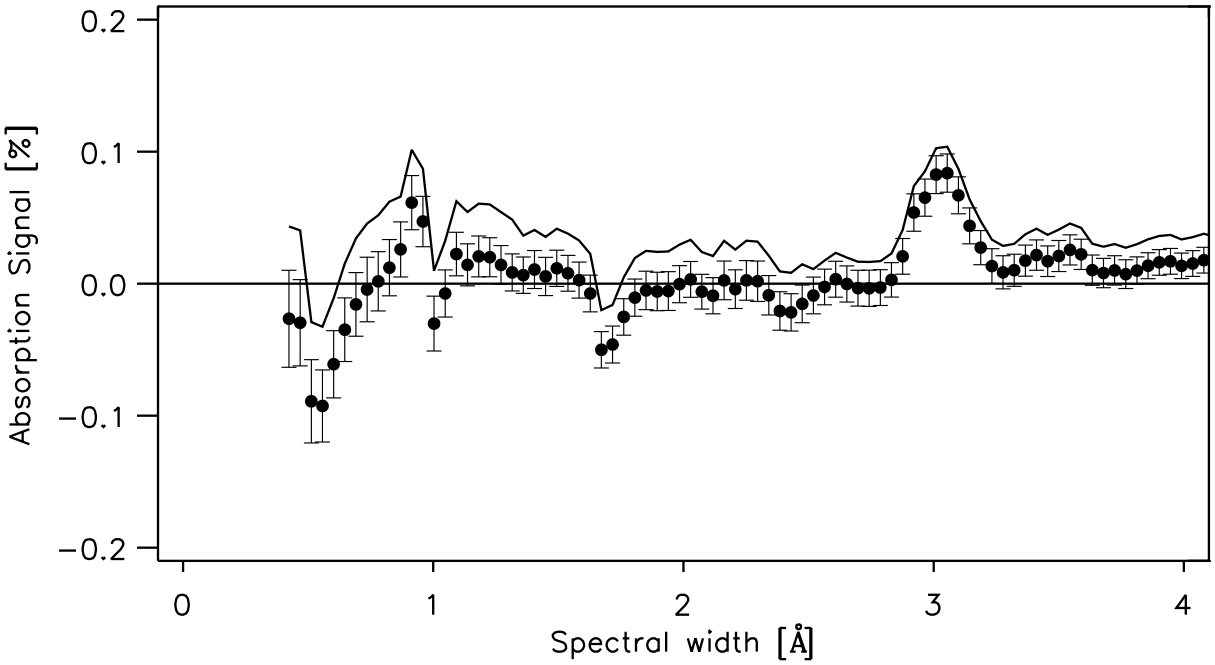

Figure 6.10 — Transmission spectroscopy around the potassium line at 7699 Å. The absorption signal is plotted over width of the central passband. Note that the width indicated here on the x-axis, is the width of one passband and not two as for the two Na D lines. The solid line shows the 3-σ line. See text for an explanation of the features at $\sim$ 0.6 Å, $\sim$ 1 Å, $\sim$ 1.8 Å, and $\sim$ 3 Å.

star gets red-shifted while the telluric line remains at its wavelength. This leads to extra flux in the central band and neither the transmission spectroscopy nor the correction for the O_2 lines applied here do correct for this effect. Normalizing the flux at the end of the night, when the absorption line was less present in the central passband will lead to an "extra absorption" in the central band during transit at the beginning of the night. If the telluric line is moving in a side band, like it is the case if the pass bands have widths of $\approx$ 1 Å and 1.8 Å, the effect is opposite. This is the same effect already described in section 6.3.1 in the context of the telluric lines around the Na D lines. For the feature at $\sim$ 0.6 Å a telluric O_2 line is responsible, which is located on one side of the potassium line and can not be easily seen in Figure 6.9. To minimize this effect and as no other correction need to be applied, we included only the first 35 frames obtained during the night in our analysis.

As indicated before, the upper limits derived in this section for the absorption by potassium in the K I resonance line are made using only one of the two potassium resonance lines. Note that due to spin coupling one would expected deeper absorption (by a factor of 2) in the potassium line not measured, if this ratio is not influenced by the planet's atmospheric environment.

6.4 Discussion

The absorption depths of sodium due to the planetary atmosphere measured in the UVES spectra are, within their uncertainties, consistent with the Subaru values of Snellen et al. (2008), and

the results by Charbonneau et al. (2002), and Sing et al. (2008a) (Table 6.1). Figure 6.8 shows our results (filled circles), the results by Snellen et al. (2008) (open squares), the results by Sing et al. (2008a) (open triangles), and as solid line and grey band, the HST measurement by Charbonneau et al. (2002) assuming it is completely unresolved within our passbands. In agreement with the results by Snellen et al. (2008) we find in this data set that it seems as if the Na D absorption lines in the planetary atmosphere are partly resolved out in the narrowest band passes, since they appear significantly below the expected absorption of the unresolved core. We over-plot the same lines that Snellen et al. (2008) have used in their Figure 5, *a, b, c,* which indicate the Na D absorption levels as a function of passband expected from the HST measurements, assuming that the atmospheric absorption feature is Lorentzian shaped with a width equal to, $2\times$ and $4\times$ the stellar width of the Na D doublet.

The correlated measurements of the sodium absorption for the different passbands show, as expected, no sudden change in absorption depth with the width of the band-pass. Considering the results shown here used passbands which differ only by four pixels, two on each side, so there is still a considerable amount of scatter in the data. The scatter in the absorption signal between adjacent passbands is due to different effects for narrow and wide passbands. For the smaller passbands the photon noise in the different pixels is the dominant source of scatter. For wider passbands the difference between the measured absorption signal is more correlated and might partly be due to residuals of the telluric spectrum or residual effects from the blaze function correction. See Figure 6.10 for comparison and section 6.3 for the explanation of these effects.

The stellar Na D_2 line shows more absorption by a factor of ~ 1.8 than the Na D_1 line. This confirms a trend already seen at lower resolution in the HST/STIS data (Sing et al. 2008b), but now also confirmed at a higher spectral resolution. Note that the ratio of the D_2/D_1 lines decreases for wider pass bands in our data (see insert in Figure 6.8). Further, it seems as if the results obtained by first removing the telluric lines in the spectrum lead to somewhat smaller values for the planetary absorption, as can be also seen in Table 6.1 in particular for wider band passes. This could for example originate from a imperfect match of the relative line strength of the telluric water lines a few ångström away from the Na doublet, to which we fitted the telluric spectra, and the telluric water lines which actually lie in one of the band passes. This might explain the decrease in the line ratio, which is not seen in the more noisy measurements without removal of the telluric contribution (not shown here).

It is interesting to note that for the Na D_2 line at mid transit, phase ~ 0, the absorption of the stellar starlight by the atmospheric sodium in HD 209458b seems to be weaker than before and after mid-transit. This effect can be seen over all passbands used for the D_2 line, but it is, due to the higher S/N in the detection of the sodium absorption, best seen in the narrow passbands. Figure 6.11 displays our results obtained for a passband of 0.75Å and the results by Snellen et al. (2008) using a passband of the same width which seem to display a similar effect. If this decrease in the apparent absorption by atmospheric sodium during mid-transit in the Na D_2 line is real, which certainly needs additional confirmation, one can speculate what can cause a decrease in the absorption by atmospheric sodium during mid-transit. The radial-velocity of the planet changes during the transit by ($\pm \sim 16\mathrm{km\,sec}^{-1}$). This corresponds to a shift in wavelength of $\pm \sim 0.3$ Å. If the cross-section of the sodium in HD 209458b atmosphere has a similar or smaller spectral width than the stellar sodium absorption lines, it will, at the beginning and end of the transit, mainly absorb light from the sides of the stellar absorption line. During mid-

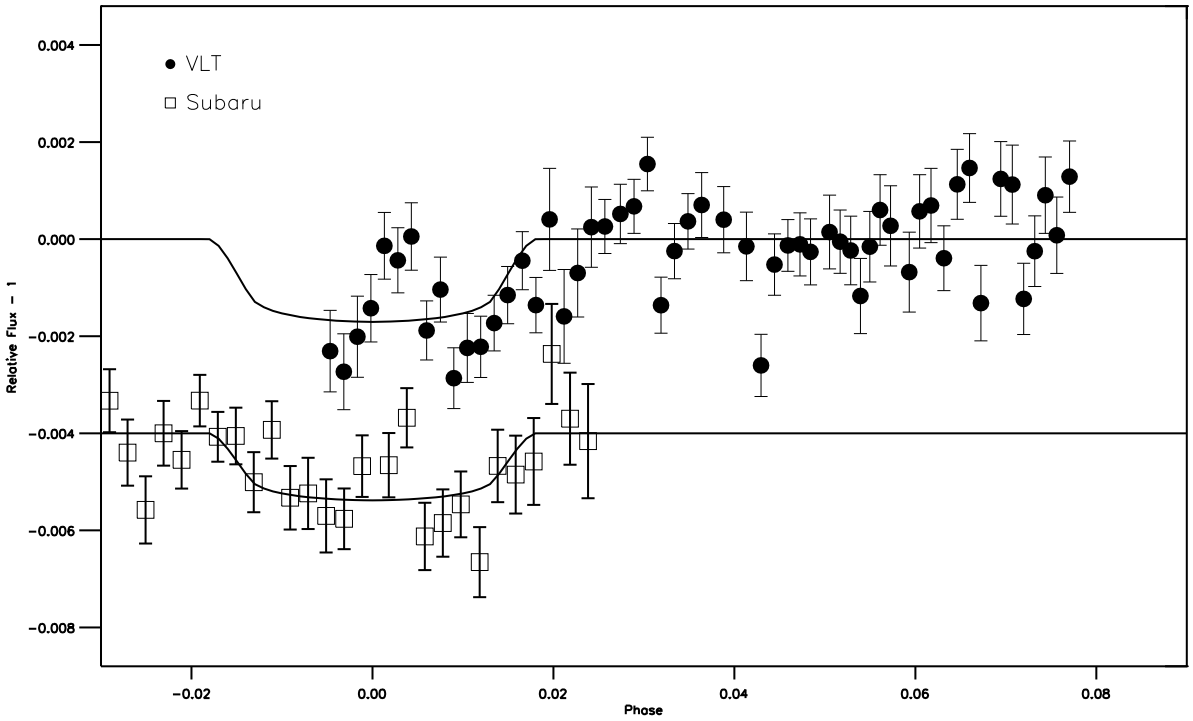

Figure 6.11 — Transmission spectroscopy of the Na D_2 line. The data points indicated by circles are obtained in this work using the UVES at the VLT. The data points indicated by squares are obtained using the HDS at the Subaru telescope. Both data sets show a possible decrease in the absorption around mid-transit, albeit at a low S/N level. The solid lines represent the best fits to the two data sets.

transit there will be only a small radial velocity difference between the star and planet. The two cores of the absorption lines, stellar and planetary, overlap and the planetary atmosphere mainly absorbs light from the core of the stellar absorption line where the intensity is already a factor of a few lower than in the wings and the surrounding continuum. As transmission spectroscopy measures only the change of flux in the total central band this would indeed produce a apparent reduction of absorption during mid-transit. To cause such an effect the planetary absorption line has to be narrow compared to the stellar line as the absorption due to the planetary sodium goes nearly back to zero during mid-transit. As the normalized intensity in the stellar absorption line drops form ~ 0.7 to ~ 0.1 over 0.3 Å it might however be possible that the change in radial-velocity of the planet during the transit indeed accounts for part of this effect. However, a very narrow planetary absorption line would not agree with our findings that the core of the planetary absorption line is partly resolved. In addition for the Na D_1 line a reduction of the absorption during mid-transit is not detected. It might however be missed as the overall level of absorption in this line is lower, and possibly changes in the atmospheric absorption with time are below the S/N ratio available in these measurements. In summary, the effect described here can not firmly be confirmed and characterized with this data set. However, the principle of this effect, changes in the measured absorption during a transit due to changes in radial-velocity of the planet, might open the possibility to further probe the structure of the atmospheric absorption lines. This however requires very high signal to noise observations with an evenly high control of systematic effects. Furthermore a change in the shape of the stellar absorption line

from center to limb might contribute to this effect (e.g. Pierce & Slaughter 1982).

That no potassium absorption by the planetary atmosphere has been measured is to some degree surprising, as models which predict planetary absorption in the line Na D doublet also predict absorption in the K I doublet (e.g. Seager & Sasselov 2000; Brown 2001). It does however fit together with the measurement of a lower than expected absorption of sodium by HST, which is confirmed by Snellen et al. (2008) and this work. Many explanations have been put forward to explain this, for example, by low sodium abundance, atmospheric circulation, high clouds, photo-ionization and others (see Seager 2003). Together with an upper limit for CO absorption by Deming et al. (2005), our upper limit for the K I line supports the idea that high clouds might be responsible for the low depth of the sodium absorption (Seager 2008). This further agrees with the findings of Snellen et al. (2008) and this work that the width of the sodium is comparable to the width of the stellar lines. High clouds would suppress the wings of the planetary absorption lines. Based on spectra from brown dwarfs, with similar T_{eff} as hot Jupiter's, it was thought that the alkali lines are very broad and span several nanometer (Seager & Sasselov 2000).

6.5 Conclusions

In this chapter we presented our results on the measurement of absorption by sodium and potassium in the Na D and K I lines, using the UVES spectrograph at ESO's Paranal observatory during planetary transit. We detect absorption by sodium consistent with earlier space and ground-based measurements. We further extend on these by measuring the ratio of the two Na D independently in a number of narrow wavelength bands. Our data also suggest a decrease of absorption in the D_2 line during mid-transit for which we have a tentatively explanation. With the same observations and same technique we establish an upper limit for absorption by potassium in the K I line, which makes us confident that this upper limit is reliable. These measurements support the idea that HD 209458b has high clouds.

Our results show that it is possible to observe atmospheric features of extra solar planets with earth based observatories, even under non-ideal observing conditions. The results form two data sets taken at different observatories under different weather conditions do not only agree with each other qualitatively, they also agree on a quantitative level. This is encouraging as it not only shows that transmission spectroscopy from the ground is reliable, it also appears as it is now feasible to probe the atmospheres of planets which are around stars one or two magnitudes fainter, or have a smaller relative coverage of the stellar surface or a smaller atmospheric scale height.

Acknowledgments

We would like to thank the support astronomer at ESO's Paranal observatory for his excellent support during the observations.

Bibliography

Brown, T. M. 2001, ApJ, 553, 1006 100, 110, 115
Charbonneau, D., Brown, T. M., Noyes, R. W., & Gilliland, R. L. 2002, ApJ, 568, 377 100, 109, 113
Dekker, H., D'Odorico, S., Kaufer, A., Delabre, B., & Kotzlowski, H. 2000, in Proc. SPIE, ed. M. Iye & A. F. Moorwood, Vol. 4008, 534 100
Deming, D., Brown, T. M., Charbonneau, D., Harrington, J., & Richardson, L. J. 2005, ApJ, 622, 1149 115
Lundstrom, I., Ardeberg, A., Maurice, E., & Lindgren, H. 1991, A&AS, 91, 199 102, 107
Mendillo, M. 2001, Earth Moon and Planets, 85, 271 105
Moutou, C., Coustenis, A., Schneider, J., et al. 2001, A&A, 371, 260 105
Patat, F. 2008, A&A, 481, 575 104
Pierce, A. K. & Slaughter, C. 1982, ApJS, 48, 73 115
Redfield, S., Endl, M., Cochran, W. D., & Koesterke, L. 2008, ApJ, 673, L87 100
Seager, S. 2003, in ASP Conference Series, Vol. 294, Scientific Frontiers in Research on Extrasolar Planets, ed. D. Deming & S. Seager, 457 115
Seager, S. 2008, Space Science Reviews, 135, 345 115
Seager, S. & Sasselov, D. D. 2000, ApJ, 537, 916 100, 110, 115
Sing, D. K., Vidal-Madjar, A., Desert, J. ., Lecavelier des Etangs, A., & Ballester, G. 2008a, ArXiv e-prints, 802 100, 107, 109, 110, 113
Sing, D. K., Vidal-Madjar, A., Lecavelier des Etangs, A., et al. 2008b, ArXiv e-prints, 803 100, 113
Snellen, I. A. G., Albrecht, S., de Mooij, E. J. W., & Le Poole, R. S. 2008, A&A, 487, 357 99, 100, 103, 107, 109, 110, 112, 113, 115
Winn, J. N., Suto, Y., Turner, E. L., et al. 2004, PASJ, 56, 655 103

Nederlandse samenvatting

De titel van dit proefschrift luidt: Stars and planets at high spatial and spectral resolution, oftewel: Sterren en planeten bij hoge ruimtelijke en spectrale resolutie. Ruimtelijke resolutie is hoe precies je kunt bepalen waar een lichtdeeltje vandaan komt. Hoe lager je ruimtelijke resolutie, hoe verder twee objecten van elkaar verwijderd moeten zijn om van elkaar onderscheiden te kunnen worden. Spectrale resolutie is het aantal kleurnuances dat je kunt onderscheiden. We zien licht van verschillende golflengtes als verschillende kleuren. Dus hoe nauwkeuriger je de golflengte kunt meten, hoe hoger je spectrale resolutie.

Sterren zie je, ook door de telescoop, meestal als een punt. Als je een lichtdeeltje opvangt, weet je niet van welk deel van de ster het komt. Je hebt dus eigenlijk maar één pixel. Hoge ruimtelijke resolutie betekent hier dus: meer dan één pixel. Met een hele grote telescoop zou je sterren die niet al te ver weg staan als een schijfje kunnen zien, zoals je ook de planeten in ons zonnestelsel door een telescoop als een schijfje ziet. Maar zulke grote telescopen zijn er voorlopig niet.

Er zijn verschillende manieren om toch ruimtelijke informatie over een ster of sterrestelsel te verkrijgen. Je kunt bijvoorbeeld met twee of meer telescopen op hetzelfde moment naar dezelfde ster kijken. Je kunt soms ook uit andere eigenschappen van het licht dat je opvangt en veranderingen daarin in de tijd ruimtelijke informatie afleiden en een model maken van het object dat je bestudeert. Dat sterrekundigen nog zo veel te weten kunnen komen over die kleine lichtpuntjes in de verte komt doordat in het heelal alles beweegt.

Met spectrale resolutie is het in de sterrekunde beter gesteld. Als je wit licht door een prisma laat vallen worden de verschillende golflengten gescheiden en zie je de kleuren van de regenboog netjes naast elkaar. Veel telescopen hebben een instrument met een prisma. Zo'n instrument heet een spectrograaf. In plaats van zelf door de telescoop te kijken gebruiken sterrekundigen tegenwoordig instrumenten die metingen doen aan het licht dat wordt opgevangen. Als je een spectrograaf gebruikt worden lichtdeeltjes van verschillende golflengtes op verschillende plaatsen opgevangen en geteld. Je weet dan wat de samenstelling van het licht was, welke golflengtes er meer in voorkwamen en welke minder. Mensen kunnen kleuren zien tussen rood (lange golflengte, lage energie) en blauw/violet (korte golflengte, hoge energie). Instrumenten kunnen een groter bereik hebben.

Het tweede hoofdstuk in dit boek beschrijft hoe hoge ruimtelijke en spectrale resolutie gecombineerd kunnen worden in één complex instrument. Hiervoor wordt een bestaande spectrograaf gecombineerd met een bestaande interferometer. Een interferometer is een cluster van twee (of soms meer) telescopen die samen worden gebruikt alsof ze deel uitmaakten van een veel grotere telescoop. Je doet dan net of je een hele grote telescoop hebt die bedekt wordt door een doek met twee gaatjes erin. Die twee gaatjes zijn de twee gezamenlijk opererende telescopen. Het licht dat word opgevangen door de twee telescopen wordt op een handige manier gecombineerd. Daardoor ontstaat een interferentiepatroon. Aan dat patroon kun je bijvoorbeeld zien hoe groot de lichtbron is. De figuren 7.1 en 7.2 illustreren dit. In figuur 7.2 is de lichtbron een punt en in figuur 7.2 is de lichtbron groter. Hoe kleiner het contrast tussen licht en donker is

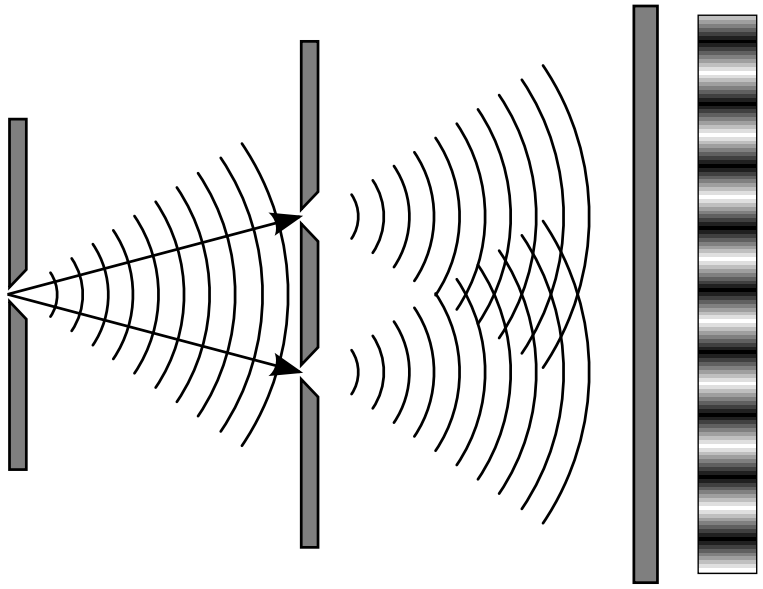

Figuur 7.1 — Schematische voorstelling van een puntvormige lichtbron waargenomen door een interferometer. Er is een scherp contrast tussen licht en donker in the interferentiepatroon dat ontstaat.

in het interferentiepatroon dat ontstaat, hoe groter de lichtbron. Wanneer je zo'n interferometer combineert met een spectrograaf kun je dit voor verschillende golflengtes doen en bijvoorbeeld ontdekken dat een object in de ene golflente groter lijkt dan in de andere. Zo kun je iets te weten komen over de samenstelling van het object. Het voorstel is om de VLT (Very Large Telescope) interferometer te combineren met een zeer goede spectrograaf die zich op hetzelfde terrein bevindt en nu alleen maar met één telescoop tegelijk gebruikt kan worden. Normaalgesproken worden instrumenten die voor de interferometer zijn ontworpen in de interferometer ingebouwd. Dit ontwerp laat zien dat het ook anders kan, waardoor de dure spectrograaf op twee verschillende manieren kan worden ingezet.

Het voorgestelde instrument, UVES-I, is nog niet gebouwd. De overige hoofdstukken in dit proefschrift gaan over zaken die desondanks nu al mogelijk zijn op gebieden waar de inzet van UVES-I in de toekomst een grote bijdrage zal kunnen leveren.

Hoofdstuk 3 gaat over een jong stellair object. Voor zover we weten vormen sterren uit een wolk van gas en stof onder de invloed van zwaartekracht. Dit object is een jonge ster met een schijf eromheen waaruit mogelijk planeten zullen ontstaan. Het object is geobserveerd met een interferometer met een redelijke spectrograaf, in het infra-rood. Door in het infra-rood naar een object te kijken kun je zien hoeveel warmte het uitstraalt. De observaties bevestigen modellen waarin de schijf bestaat uit een warm deel aan de binnenkant en een kouder deel aan de buitenkant.

De hoofdstukken 4 en 5 gaan over twee dubbelstersystemen. Een dubbelstersysteem is een systeem dat bestaat uit twee sterren die ieder in een eigen elliptische baan om elkaar heen draaien (of eigenlijk om het gezamenlijke zwaartepunt). Dubbelstersystemen komen veel voor en kunnen ook planeten hebben. Het is zelfs zo dat de meeste sterren in het heelal deel uitmaken

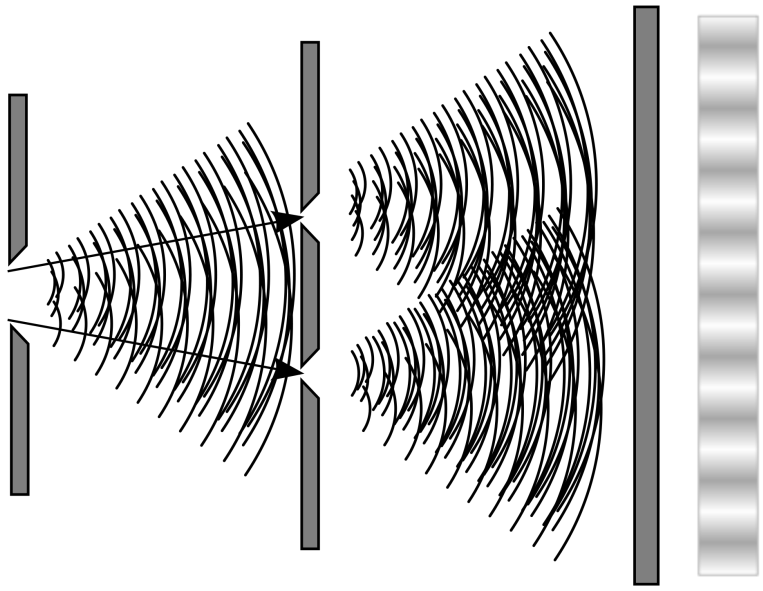

Figuur 7.2 — Schematische voorstelling van een iets grotere lichtbron dan in figuur 7.1, eveneens waargenomen door een interferometer. Het contrast is nu vager.

van een dubbelstersysteem. Sterren draaien ook altijd om hun eigen as (onze zon doet dit bijvoorbeeld met 5 km/s). In dit onderzoek is gekeken wat de hoek is tussen die as en de baan van de ster en of dit voor beide sterren hetzelfde is. Dit is belangrijk om te begrijpen hoe dubbelstersystemen gevormd worden. Voor het systeem in het sterrenbeeld zwaan is gevonden dat beide assen parallel zijn. Voor het systeem in het sterrenbeeld Hercules bleek dit niet het geval.

Dit laatste is een onverwacht resultaat. Er wordt meestal aangenomen dat de assen van een systeem waar de sterren zo dicht bij elkaar staan wel parallel zullen zijn. Het lost echter ook een probleem op waaraan astronomen al 20 jaar werken: een bepaald aspect van de baan van dit systeem, dat apsidal motion genoemd wordt, gedraagt zich niet zo als men berekend had. Een ster in een dubbelstersysteem beweegt in een elliptische baan. Die elliptische baan zelf draait ook nog eens een keer rond. De as voor deze draaiing gaat door het zwaartepunt, oftewel een van de brandpunten van de ellips. Deze beweging heet apsidal motion en wordt veroorzaakt door een verschijnsel dat we kennen als getijdenwerking. Bij DI Herculis bleek de baan langzamer te draaien dan verwacht. Er zijn in de loop der jaren verschillende voorstellen gedaan om dit te verklaren, onder andere een herziening van de relativiteistheorie. Nu we weten dat de rotatie-assen van de sterren, in tegenstelling tot wat werd aangenomen, niet parallel zijn, is het geobserveerde gedrag precies wat we op grond van de bestaande theorie verwachten en is het probleem verdwenen.

Hoe kan men de assen van sterren meten zonder een instrument zoals in hoofdstuk twee besproken is ter beschikking te hebben? De orientatie van de draaiingsas van de twee sterren kon worden bepaald omdat ze elkaar vanaf de aarde gezien regelmatig verduisteren (de ene ster beweegt dan voor de andere langs) en omdat het Doppler effect ook van toepassing is op licht.

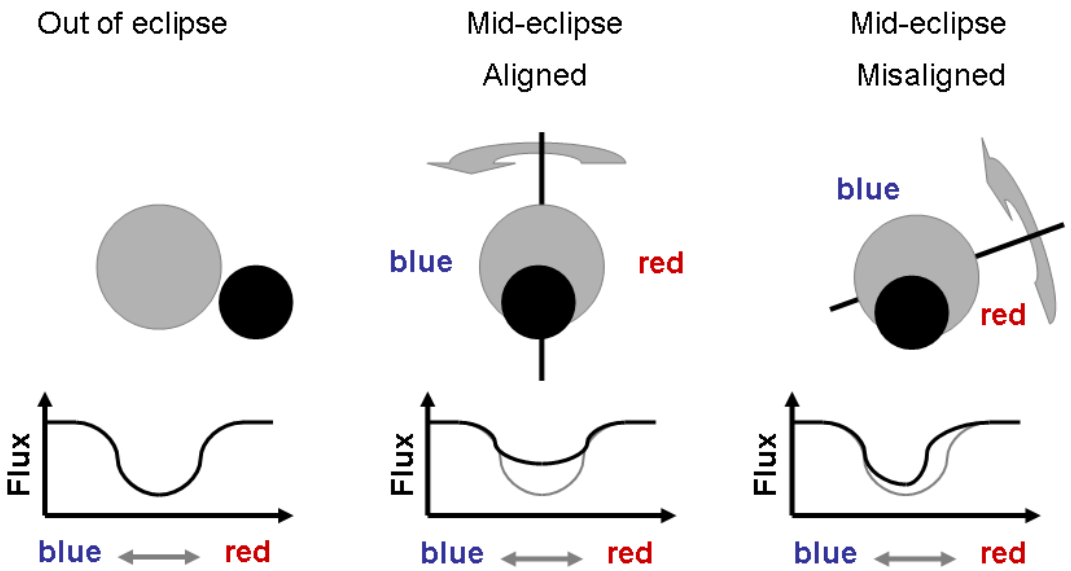

Figuur 7.3 — Schematische voorstelling van het Rossiter-McLaughlin effect. Vanwege het draaien van de ster is een geobserveerde absorptielijn verbreed (links). Een gedeeltelijke verduistering door een object op de voorgrond vervormt de absorptielijn anders als de as een rechte hoek maakt (midden) dan als hij geen rechte hoek maakt (rechts) met het vlak van de baan waarin de sterren zich bewegen.

Een sterverduistering in een verduisterend dubbelstersysteem lijkt op een zonsverduistering bij ons. Maar in plaats van dat de maan tussen ons en onze zon door beweegt, beweegt de ene ster tussen ons en de andere ster door. Het Doppler effect treed op als een bewegende bron golven uitzendt. Die golven kunnen geluidsgolven zijn, zoals bij een ambulance die voorbij rijdt, maar ook lichtgolven, zoals bij een draaiende ster. Omdat een ster om z'n eigen as draait is er altijd een deel van de ster dat naar ons toe beweegt en een deel dat van ons af beweegt. Als een lichtbron naar je toe beweegt worden de lichtgolven een beetje in elkaar gedrukt waardoor alle golflengten iets korter lijken dan ze eigenlijk zijn. Dit noemen we blauw-verschoven. Als een lichtbron van je af beweegt worden alle golflengtes juist een beetje uitgerekt, waardoor ze langer lijken dan ze eigenlijk zijn. Dit noemen we rood-verschoven. Als je de hele ster kunt zien, zie je evenveel rood-verschoven licht als blauw-verschoven licht.

Als nu, bijvoorbeeld, aan het begin van een verduistering het deel van de ster dat naar ons toe beweegt grotendeels door de andere ster van het dubbelstersysteem bedekt wordt, dan ontvangen we vooral rood-verschoven licht (dus van het onbedekte deel). Als dan later het andere deel bedekt wordt, ontvangen we vooral blauw-verschoven licht. Dit is wat we waarnemen als de rotatie-as van de ster een loodrechte hoek maakt met het vlak van de baan van de ster. (Dit komt overeen met het middelste plaatje van figuur 7.3.) Als de as juist in het vlak van de baan ligt, worden de delen die rood-verschoven en blauw-verschoven licht uitzenden steeds in gelijke mate bedekt gedurende de verduistering. De verandering in de verhouding tussen rood- en blauw-verschoven licht in de loop van de verduistering is dus afhankelijk van de stand van de as. Door de verschuivingen te meten, kan men dus berekenen hoe de as van de ster staat ten opzichte van zijn baan. De verschuivingen kunnen gemeten worden doordat het spectrum van licht dat een ster uitzendt herkenbare absorptielijnen bevat. Het effect dat je ziet door deze

verschuivingen heet het Rossiter-McLaughlin effect en wordt geïllustreerd in figuur 7.3.

In hoofdstuk zes wordt een exo-planeet bestudeerd. Dit is een planeet die niet om onze zon draait maar om een andere ster en dus deel uit maakt van een ander sterrestelsel dan het zonnestelsel. Er zijn de laatse paar jaar steeds meer exo-planeten ontdekt, de eerste in 1995. Ook bij het ontdekken en bestuderen van exo-planeten wordt dankbaar gebruik gemaakt van verduisteringen en ook van het Doppler effect.

De planeet die hier bestudeerd is heeft de prachtige naam HD209458b en is een grote gasplaneet, een beetje zoals Jupiter, maar dan veel dichter bij z'n ster, zelfs dichterbij dan Mercurius bij de zon. In dit onderzoek is gekeken naar de 'atmosfeer' van deze planeet. Bij een planeet als deze, die mogelijk geheel uit gas bestaat is het binnenste gedeelte te dicht om licht door te laten. Alleen het buitenste laagje van deze bol gas is doorzichtig, en dit beschouwen we dus als de atmosfeer. Het licht van de ster waar deze planeet omheen draait, net als onze zon, bevat licht van een heleboel verschillende golflengten. Als zulk licht door een gas reist, absorberen de gasdeeltjes heel specifieke golflengten. Elk element van het periodiek systeem heeft, als gas, z'n eigen herkenbare absorbtiepatroon. Als de planeet voor de ster staat, komt een gedeelte van het licht van de ster dus door de atmosfeer van de planeet voordat het onze telescoop bereikt. Als je dan met behulp van een gevoelige spectrograaf kijkt welke golflengten er nu ineens duidelijk minder inzitten dan toen de planeet er niet voor stond kun je erachter komen uit welke gassen de atmosfeer van de planeet bestaat.

In dit onderzoek is gevonden dat de atmosfeer van HD209458b natrium bevat. Naar kalium is ook gezocht, maar dit blijkt er niet te zijn, of in ieder geval niet in voldoende mate om met de huidige middelen te kunnen meten. Het valt namelijk nog niet mee om dit de meten, want het effect is klein en er zijn allerlei andere factoren die het spectrum beinvloeden. De atmosfeer van de aarde, waar het licht natuurlijk ook doorheen moet als de telescoop op aarde staat, absorbeert bijvoorbeeld ook allerlei golflengten.

Er valt dus ook met beperkte ruimtelijke resolutie al heel wat te meten en te ontdekken. Wel zou het UVES-I instrument op al deze gebieden meer mogelijkheden bieden. Bijvoorbeeld zou je daarmee ook de stand van de assen kunnen meten bij dubbelstersystemen die elkaar vanaf de aarde gezien niet verduisteren.

Vervolgonderzoek zal zich vooral concentreren op het meten van draaiingsassen in meer dubbelstersystemen en in ster-planeet systemen en de consequenties van de gevonden resultaten op de theorie over de vorming van sterrestelsels.

Curriculum vitae

The author of this thesis was born in, and raised nearby the city of Osnabrück, in northern Germany. It was an easy choice for me to study physics in Hamburg, a wonderful harbor city, where I was able to do a minor in astronomy for the first two years of my study. After the Vordiplom I enrolled for one year as an Erasmus student at the University of Southampton, England, where I followed lectures on my second passion, Spacecraft Systems Engineering. Back in Hamburg I continued to study physics, with satellite oceanography as a second minor. During my studies I worked for one summer at ESTEC Noordwijk, in a calibration campaign for the HASI instrument on-board the Huygens spacecraft. I finished my studies in physics in summer 2003 with my diploma thesis entitled "Preparation of a superconducting quantum point contact".

During this period I also trained as a research diver at the Universities of Hamburg and Kiel. Subsequently I have participated, either as an assistant researcher or diver, on research expeditions around the Orkneys, and Hebrides and on an expedition from Tromsø to Svalbardor. I also worked for a few months as a diver for the Alfred-Wegener-Institut on Helgoland.

I realized that my main interests were on the intersection between science and the development of instrumentation, in particular in the field of optical/infrared interferometry. I therefore started my PhD on this subject at Leiden University. Unfortunately time scales on which instruments are developed are not a good match for PhD time scales. Therefore, my research focus was slightly deviated towards the science that can be conducted using existing instruments, resulting in this thesis. During my PhD research I participated in summer schools in Alpbach (Austria), Dwingeloo (The Netherlands), Goutelas (France) and Porto (Portugal). I also observed at the Lick Observatory (USA), the VLT at Cerro Paranal (Chile), the Telescopio Nazionale Galileo (Spain), and the Oberservatoire de Haute Provence (France) and I presented the results of my work either orally or via posters at conferences in Glasgow (Scotland), Antalya (Turkey), Orlando (USA), Veldhoven (The Netherlands), and Cambridge (USA).

Nawoord

A PhD thesis is the work of many, and this particular book is no exception. I would like to thank all the people who have made it possible for me to write this thesis and supported me greatly throughout my time in Leiden.

Thank you to everybody at the Sterrewacht. You all made me feel at home right from the beginning and made my stay a very pleasant one. David, Tycho, Erik, and Aart, you are setting standards. Wherever I will go next, in terms of friendly, fast and competent computer support it can only go downhill. Jeanne, Kirsten, Anita, Liesbeth you always have been helpful, right from my first day by helping me finding a place to stay.

Bob, thank you a lot for all your outstanding support throughout my PhD. Working with you is great fun. Without you and the many discussions we had, my work here would have been so much more difficult. Sabine, I very much appreciate that you started the binary project with me, that you introduced me to the world of astronomical spectroscopy, and for your remote support during my first observing runs. Dominic, Sergio, Evelyn, your are the best office mates I can think of. Thank you Dominic for your help whenever I needed it, for your sense of humor and for showing up every morning at 06:00. Demerese, I enjoyed the runs, hanging out with you and the good times at the Sterrewacht. See you at the next summer school. Excellent recipe Ned, it worked, but I nearly burned down the kitchen. Liesbeth you are a brilliant support for every paranymph. I enjoyed all the good times inside and outside the Sterrewacht, in particular with, David, Andreas, Stijn, Remco, Sarah, Rob, Esther, Selina, Michael, Remko, Pascal, Ramon, Ernst, Dave, Cyril, Richard, Nina, Wolfgang, Andreas, Uli, Claudio, Brent, Niruj, Herma, Carolina, Olmo, Isa, Roderik, Anne-Marie. Thanks also to everybody I forgot here and everybody who helped me out with 20cts.

I enjoyed every training and the weekends with the people from the LSD. Hartelijk bedankt voor het luisteren naar mijn 'nederlands' op de borrels. Everybody from the Hong Ying, I always have a great time training with you.

Ellis, you are the first person I met in Leiden. I enjoyed the Tangos we danced. Ik zal aan begrijpen en verstaan werken, beloofd! Kristo I hope you enjoy the north. Christian and Hanna I am looking forward to relaxing at your place. Christian your moving support is excellent. Eva I am glad you came to my party! Graciana all the best in Oxford.

Sebastian, Birte, and Felix, I very much appreciate your friendship and I can always count on your support when I need it!

Hilke thank you for your endless support and passion. Over the last years, you did not deliver one PhD, but two! I enjoyed all the times we have spent together and I am looking forward to all the good times to come, wherever that will be.